The Fusion of Advanced Fuels to Produce Medical Isotopes Using Inertial Electrostatic Confinement

B.B. Cipiti

May 2004

UWFDM-1226

FUSION TECHNOLOGY INSTITUTE

UNIVERSITY OF WISCONSIN

MADISON WISCONSIN

The Fusion of Advanced Fuels to Produce Medical Isotopes Using Inertial Electrostatic Confinement

B.B. Cipiti

Fusion Technology Institute
University of Wisconsin
1500 Engineering Drive
Madison, WI 53706

http://fti.neep.wisc.edu

May 2004

UWFDM-1226

THE FUSION OF ADVANCED FUELS TO PRODUCE MEDICAL ISOTOPES USING INERTIAL ELECTROSTATIC CONFINEMENT

by

Benjamin B. Cipiti

A dissertation submitted in partial fulfillment of

the requirements for the degree of

Doctor of Philosophy

(Nuclear Engineering & Engineering Physics)

at the

UNIVERSITY OF WISCONSIN-MADISON

2004

Abstract

Experiments are described that used an Inertial Electrostatic Confinement (IEC) fusion device to create radioisotopes for medical diagnostics. The IEC concept utilizes spherically concentric electrodes to accelerate fusion ions to high center of mass energies, allowing the use of the D-D and advanced D-^{3}He fusion reactions. The D-^{3}He reaction produces a high-energy 14.7 MeV proton, and this proton is energetic enough to be used to create radioisotopes. The advantage of isotope production using this method is that the IEC device is small and relatively inexpensive, so it may be developed into a semi-portable device.

This dissertation focuses first on where specifically the fusion reactions are occurring, and thus where the source of the reaction products are coming from. These source regime experiments were done with both D-D and D-^{3}He, and three source regimes were identified. The converged core regime is due to reactions occurring in a small core in the center of the cathode. The volume regime represents charge exchange reactions occurring distributed throughout the vacuum chamber. The embedded regime represents beam-target reactions within the grid wires of the cathode.

It was found that at 2 mtorr operating pressures, the D-D reaction is dominated by the volume regime at 70% of the total reaction rate. The converged core accounted for 22% of the total rate, and the other 8% was due to embedded D-D reactions. On the other hand, the D-^{3}He reaction was strongly dominated by embedded reactions occurring within the metal cathode of the device. Roughly 95% of the total D-^{3}He reaction rate was from the embedded regime. The other 5% came from the converged core mode, and the volume regime was negligible.

The beam-target D-^{3}He fusion regime was used to create medical isotopes in two different systems. The designs focused on creating short-lived species capable of use in Positron Emission Tomography. The first isotope created was ^{94m}Tc, a positron emitter with a 52-minute half-life. It was created in a solid molybdenum cathode. Beam-target D-^{3}He reactions occurring in the outer layers of the molybdenum created high-energy protons to activate the surrounding material. Approximately 1.5 nCi of ^{94m}Tc were created using the ^{94}Mo(p,n)^{94m}Tc reaction.

The second isotope created was ^{13}N, a positron emitter with a ten-minute half-life. The cathode was replaced with a thin-walled, stainless steel tube with water re-circulating through it. The ^{13}N was created using the ^{16}O(p,α)^{13}N reaction from the oxygen in the water. Approximately 1.0 nCi of ^{13}N was created using this system.

The final part of the research investigated the effects of deuterium and helium implantation in the various cathodes. The experimental embedded fusion rates were used to determine the fusion ion implantation density. The average deuterium density in the tungsten-rhenium grid wires varied from about 0.008 to 0.024 deuterium to metal atomic ratio at the 100 kV condition. The helium-3 density was around 0.056 helium to metal atomic ratio at the same voltage. The effect of the implantation on the surface morphology was determined using scanning electron microscopy. Deuterium did not appear to affect the surface of tungsten after high temperature (>800 °C) implantation. Helium created a porous surface structure at the same temperatures starting at about $4x10^{16}$ ions/cm^{2}. The pores increased in size and decreased in density with increasing temperature and fluence.

Acknowledgements

First, I would like to express my sincerest thanks to my thesis advisor, Professor Gerald Kulcinski for his incredible support on this project. I have received great advice and ideas over the four years that went well above and beyond what was expected. I would like to thank Dr. John Santarius for the numerous brainstorming office visits, and for his theoretical insight. Bob Ashley has always been someone to depend on when working in the lab or running an experiment. Dr. Harrison Schmitt has been a supportive presence in his visits to our project.

My fellow students have been a great deal of fun to work with. My thanks to Greg Piefer, S. Krupakar Murali, John Weidner, Ross Radel, Alex Wehmeyer, Dave Boris, and Tracy Uchytil for all the help. Whether it was throwing around ideas in the office or helping with a run in the lab, they have always managed to make it enjoyable.

I feel fortunate to be at a great research university like Wisconsin with a huge knowledge base to pull from. Specifically, I would like to thank Professor Jerry Nickles for his advise and help on the isotope production systems. Dennis Bruggink, Sue Ann Hubanks, Linda Kraft, and Joan LePain have been great to work through administrative details with.

I would like to thank Dr. Rick Nebel, who was my mentor at Los Alamos, for his help while I was formulating the research idea. Dr. Steve Zinkle and Dr. Lance Snead at Oak Ridge National Laboratory were helpful in providing the tungsten samples for the implantation experimentation.

This research was performed under appointment to the Fusion Energy Sciences Fellowship Program administered by Oak Ridge Institute for Science and Education

under a contract between the U.S. Department of Energy and Oak Ridge Associated Universities. I have been very appreciative of the financial support afforded by the fellowship. In addition, I would like to thank the Greatbatch Foundation and Grainger Foundation for financial support on the project.

Finally, I would like to thank my family for the support they have given me. My parents have always been there for me, and I would not have gotten to this point without all of their encouragement. I would like to thank my brothers and my sister-in-law for all of the advise about college. My grandparents have taught me about the things that matter the most in life. I feel very fortunate to have the family that I have.

Table of Contents

Table of Figures

Chapter 2

Chapter 3

Chapter 4

Chapter 5

Chapter 6

Chapter 10

Chapter 12

Chapter 13

Chapter 14

Appendix B

Appendix C

Table of Tables

Chapter 7

Chapter 8

Appendix B

Appendix C

Chapter 1 Introduction

Since the 1950's and the beginning of fusion research, virtually all of the work to control fusion has been for the ultimate purpose of producing power. However, the by-products of the various fusion reactions can have other positive uses in the future. Fusion reactions release energy in the form of high-energy charged particles or neutrons, and these products have the potential to do more than produce electricity alone.

High-energy protons can be used for the production of radioisotopes and the destruction of long-lived radioactive wastes [1]. High-energy neutrons can be used for the same purposes as well as for radiotherapy and the alteration of properties of solids. These specific commercial/industrial applications for fusion reactions do not necessarily need a reactor that produces more power than it consumes. The device can be a net energy user, in effect using electrical input to create a value-enhanced product. A compact, inexpensive device for producing high-energy particles would fill many of these needs.

Fusion research has been dominated in the past by study of the deuterium-tritium (D-T) reaction. Less work has focused on advanced fuels such as the deuterium-deuterium (D-D) and deuterium-helium-3 (D-^{3}He) reactions because they require two to three times higher energies to reach suitable reaction rates. However, the advanced reactions are attractive because they release less energy in the form of energetic neutrons.

Inertial Electrostatic Confinement (IEC) offers a unique method for achieving steady-state D-D and D-^{3}He reactions. The IEC concept relies on gridded, spherical electrodes to confine and accelerate fusion ions to considerable energies (40-200 keV) [2]. With the advanced fusion reactions, the IEC concept is able to produce high-energy

protons in addition to high-energy neutrons. Its main advantage is that the concept is relatively simple and inexpensive.

The purpose of this research was to focus on one application of the D-^{3}He reaction, to produce radioisotopes for medical applications. This dissertation is divided into three areas, all related to the isotope production. The first part investigates the fusion reaction source regimes within the IEC device. It is important to know exactly where the fusion reactions are occurring within the device, both for theoretical understanding and for potential use as a proton source. The second part looks at the specific designs for producing medical isotopes. The final part focuses on learning more about ion implantation into the cathode, which is directly tied to the previous two sections.

1.1 Significance of Research

1.1.1 Source Regimes

The investigation of the reaction regimes in the IEC chamber has significant implications on understanding the theory of the device. There are various ways that the fusion reactions can occur depending on the run conditions, and each regime has a specific reaction density distribution in the chamber. Theoretical work up until this point at the University of Wisconsin, and at other sites studying the IEC, has never matched the reaction rates generated in experiments [3,4,5]. The experiments have always performed much better than predicted. One of the apparent reasons for the discrepancy is that the numerical modeling up to this point has not taken all of the reaction regimes into account.

The different source regimes also influence the diagnostics of the device. The D-D and D-^{3}He reaction rates at most experimental facilities (including the UW device) are

determined with a proton detector pointed towards the center of the device. An estimate of the reaction rate is found using a calibration factor calculated from MCNP (Monte Carlo) methods. The calibration factor for the UW device involves assumptions about the source distribution in the device from the work of Thorson [6]. A change in the understanding of the source distribution will drastically change the calibration factor that should be used. This calibration must be known to accurately report reaction rates.

Finally, an understanding of these fusion regimes is important to determine spatially where the D-^{3}He fusion protons are generated for isotope production. The distribution must be known to make maximum use of the proton flux. For example, if many of the protons are created in the center of the device, there will be a larger flux at that location, making it a good place to create medical isotopes. The knowledge of the source regimes will help to design better isotope production systems.

1.1.2 Isotope Production

Currently most commercial or medical isotopes are created in either nuclear reactors using the large neutron flux, or accelerators (linacs or cyclotrons) using 10-20 MeV protons. The D-^{3}He fusion reaction releases a 14.7 MeV proton that may be used to produce isotopes as well. The D-^{3}He proton production rate in an advanced IEC device may be able to reach the fluxes generated in cyclotrons. Typical cyclotron operation generates on the order of 10^{14} p/s [7]. The proton production in the UW IEC device is currently high enough to demonstrate proof of principle radioisotope production.

The advantage of using the IEC concept for isotope production is that it is a simple device that can be built for around $100,000. Cyclotrons and linacs are large and

expensive devices. Cyclotrons currently cost between $1.2-1.7 million [8]. An IEC isotope generator could be inexpensive and placed, for example, on the back of a truck, making it suitable for field operation. With this kind of a setup, isotopes may be made more available for medical imaging procedures in remote locations or small communities.

When using short-lived isotopes for medical imaging, there is a lower limit to the half-life that can be used depending on where the isotope is created. The limit depends on the time necessary to produce, separate, and transport the isotope to the hospital or location of interest. To use a very short-lived species, the isotope must be created either on site or very close to the premises. Often this is not the case with accelerators. In this regard, a portable source of isotopes using IEC could be a valuable instrument.

1.1.3 Ion Implantation

The cathode grid used in normal IEC operation receives a large continuous ion flux. Depending on the run, deuterium or helium fuel may be used. This ion implantation can lead to significant number densities of the gases in the metal wires, and gives rise to a beam-target reaction regime. The beam-target regime will be shown later in this study to be an important part of the total D-^{3}He reaction rate, so an understanding of the implantation is required for isotope production.

In order to predict the contribution of the beam-target regime, the number density as a function of depth must be known. However, this variable is difficult to predict. It is a function of the ion energy, ion type, ion current, and temperature of the sample. All these variables affect how far the ion travels, how it diffuses, the nature of the buildup in the sample, and any effect on the surface structure of the metal.

The effect on surface structure can have implications on the running of the IEC device. Any blister formation or sputtering can effect the electrical operation of the device. The material used for grid wires in the UW experiment is a tungsten-rhenium alloy. Coincidentally, tungsten is a material that is being studied for use as a plasma facing material in both magnetic and inertial confinement work. Therefore, the effects of deuterium and helium implantation on tungsten are an important topic of study in the fusion community. This research concentrates on the effects of deuterium and helium implantation on tungsten at high temperatures (700-1300 °C).

1.2 References

[1] G.L. Kulcinski, "Near Term Commercial Opportunities from Long Range Fusion Research," *Fusion Technology*, **30**, 411 (December, 1996).

[2] R.P. Ashley, G.L. Kulcinski, J.F. Santarius, S.K. Murali, G. Piefer, B.B. Cipiti, R. Radel, J.W. Weidner, "Recent Progress in Steady State Fusion using D-^{3}He," *Fusion Science and Technology*, 44, 564 (September, 2003).

[3] J.F. Santarius, University of Wisconsin-Madison, private communication (2002), see also "Modeling the UW IEC Experiment," presented at the 4th U.S.-Japan Workshop on Inertial Electrostatic Confinement, March 25-26, 2002, Kyoto, Japan.

[4] K. Tomiyasu, "Pulsed Operation of an Inertial Electrostatic Confinement Fusion Device and its Applications," Master's Thesis, Tokyo Institute of Technology, Tokyo, Japan (February 13, 2004).

[5] M. Ohnishi, Y. Yamamoto, M. Hasegawa, K. Yoshikawa & G.H. Miley, "Study on Inertial Electrostatic Confinement Fusion as a Portable Neutron Source," *Fusion Engineering and Design*, **42**, 207 (September, 1998).

[6] T.A. Thorson et al., "Fusion Reactivity Characterization of a Spherically Convergent Ion Focus," *Nuclear Fusion*, **38**, 495 (1998).

[7] J.A. Sorenson & M.E. Phelps (1987). *Physics in Nuclear Medicine, Second Edition* New York: W.B. Saunders Company.

[8] E. Adams & K. Flynn, "A Systematic Review Update of FDG-PET as a Diagnostic Test in Cancer and Alzheimer's Disease," Health Services Research and Development Services Technology Assessment Report, MTA 98-032 (September, 1998), see also www1.va.gov/resdev/prt/petreport.htm.

Chapter 2 Inertial Electrostatic Confinement

The IEC concept relies on spherical electrodes made of wires to confine and accelerate fusion ions. Figure 2-1 shows the general setup. A large negative voltage is applied to the inner cathode, while the outer anode is held at ground potential. An ion source is located outside of the anode. Ions are accelerated into the center of the device where they may fuse with one another. The transparency of the two electrodes allows for the ions to make multiple passes to increase their chance for fusion. In an ideal system, the ions would re-circulate long enough for breakeven to occur. This confinement approach does not form a Maxwellian plasma in which much of the input energy goes towards useless low energy ions and electrons.

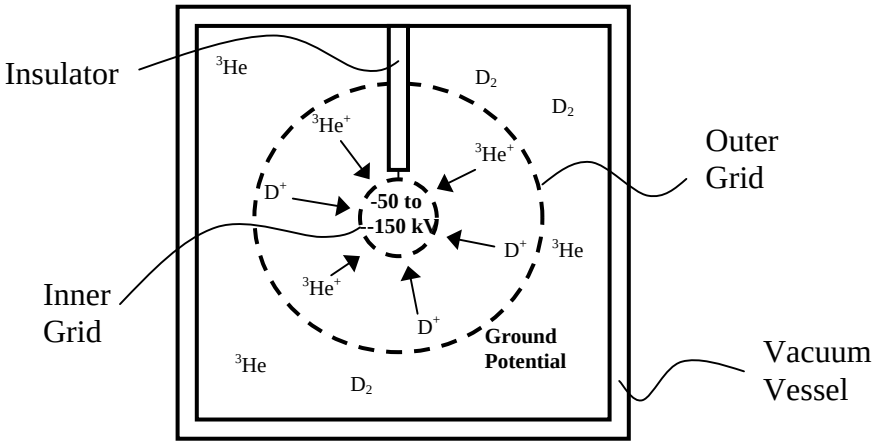

Figure 2-1: Schematic of the Inertial Electrostatic Confinement Approach

The D-T, D-D, and D-^{3}He fusion reactions have been studied using Inertial Electrostatic Confinement. These reactions are shown in Figure 2-2. The D-D reaction has two, equally probable reaction paths to release either high-energy neutrons or protons. Both this reaction and D-T can be used as a source of neutrons. The proton generated from D-D does not have high enough energy for use in producing isotopes.

Most cross-sections for (p,x) reactions require proton energies around 10-20 MeV [1] to overcome the coulomb repulsion of the nucleus. On the other hand, the 14.7 MeV proton generated from D-^{3}He has plenty of energy for isotope reactions.

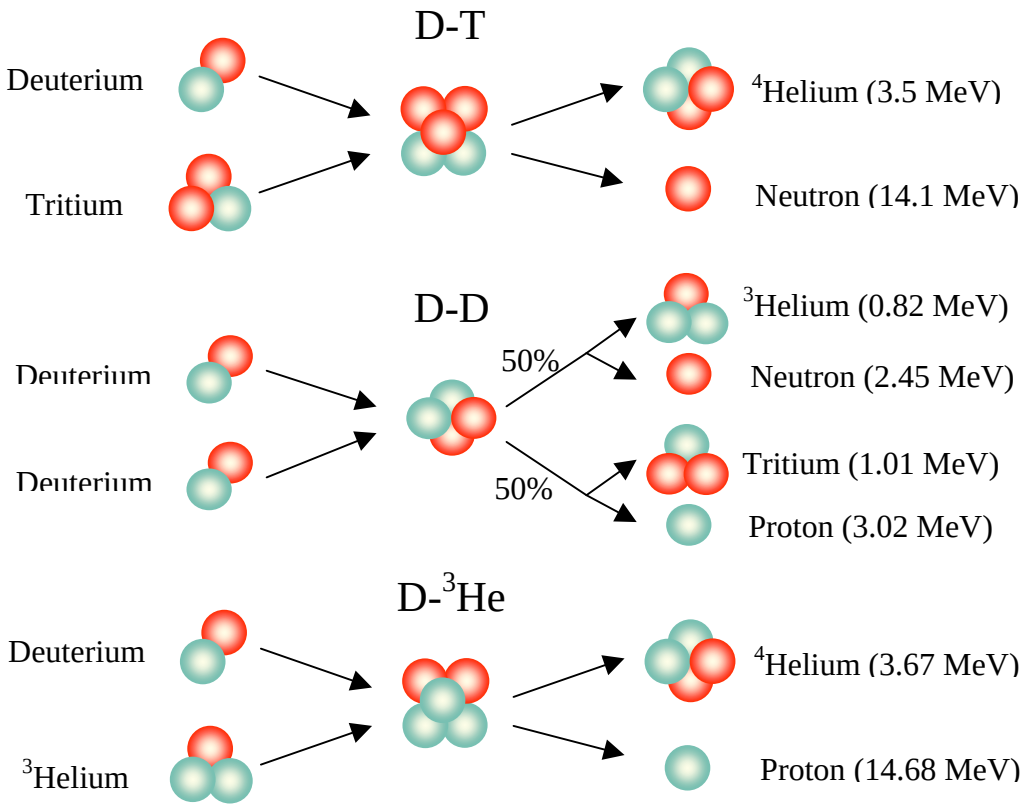

Figure 2-2: IEC Fusion Reactions and Product Energies

The shape of the cross-section plots for these three reactions vary quite a bit over the energies of interest in the IEC project. Figure 2-3 shows a plot of the fusion reactivity (in m^3/s) for the reactions assuming a spherical velocity distribution in the IEC case. The reactivity is plotted as function of IEC well depth in keV. The D-T reaction has the highest reactivity over this energy range. The reactivity of D-D dominates D-^{3}He below about 30 kV, but then D-^{3}He takes over.

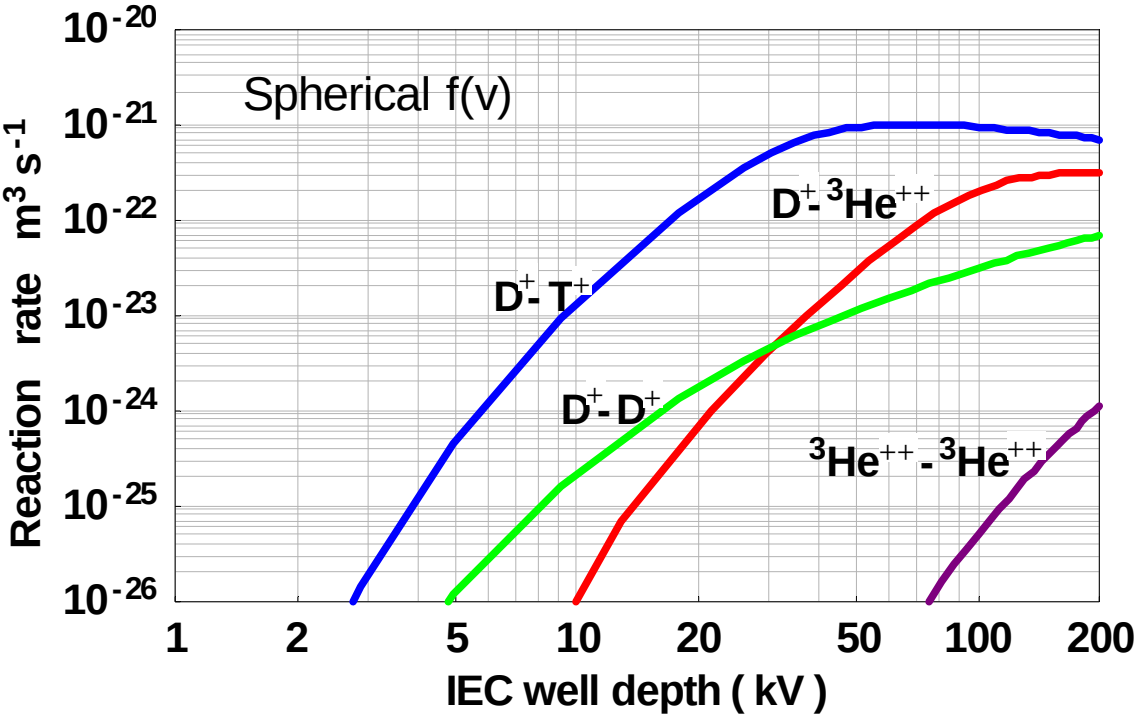

Figure 2-3: Fusion Reactivities as a Function of Energy in a Spherical IEC Device [2]

2.1 History of IEC Research

The IEC concept dates back to the late 60's with the work of Farnsworth and Hirsch [3]. Farnsworth first patented the idea behind IEC [4], and Hirsch built on the work using a strong, negative, electrostatic potential well to promote fusion reactions. The large, negative potential drop was found to allow for the acceleration of ions to energies where the fusion cross-sections are considerable. With six ion guns, Hirsch was able to produce $3x10^9$ n/s using the D-T reaction at a cathode voltage of 150 kV [3].

In recent years, there have been a limited number of IEC projects around the world. In the U.S., the University of Illinois [5,6] along with Daimler-Benz [7] first used IEC for a low power commercial neutron generator. Marshall Space Flight Center has

investigated using the IEC concept for space propulsion [8]. Los Alamos National Lab is doing work on a unique approach to the IEC concept called the Periodically Oscillating Plasma Sphere (POPS) [9]. The University of Wisconsin group has been running D-D since 1991 and is unique in that it also focuses on the D-^{3}He reaction [10].

There are currently five IEC projects in Japan and one in South Korea. Tokyo Institute of Technology, Kyoto University, Kansai University, Kyushu University, and Hitachi Ltd. are all focusing on D-D [11,12,13,14,15]. Seoul National University and Hanyang University have started work on an IEC project in South Korea [16].

Alternatives to the gridded IEC system are the Penning Trap [17] and Polywell™ [18,19] concepts. The Penning Trap uses a combination of magnetic and electric fields to confine electrons in a dense, spherical region. The Polywell™ uses cusp magnetic fields in a semi-spherical geometry to confine electrons. The dense electron cloud then is able to accelerate and confine ions in a similar manner as how a grid operates. These types of setups will probably be desired if IEC moves towards a reactor scenario because they eliminate the loss of ion energy into a metal cathode.

Many of the groups in the past few years have focused on the neutron generation side of the research. The goals include using the IEC device for land-mine detection, industrial quality control, detection of explosives, and detection of radiological substances. Recently the work has shifted towards reaching a lower pressure converged-core operating regime. The purpose of reaching converged core is to increase the reactions rates. This regime will be discussed in later sections.

2.2 University of Wisconsin IEC Research

The University of Wisconsin (UW) IEC fusion experiment has made considerable progress in the past few years in the burning of the D-D and D-^{3}He fusion fuels. The project has achieved a record steady state production of 1.8×10^8 n/s from the D-D reaction [20], and a comparable proton production rate from the D-^{3}He reaction. Research at Wisconsin has focused predominantly on increasing the voltage capabilities and reaction rates up until recently, but the rates have been high enough in the last two years to begin work on alternative uses of the device as a source of neutrons or protons.

Currently, there are many projects in progress at Wisconsin. On the theoretical side, numerical codes have been developed to model the reaction rates [21]. The current status is that the predicted rates are still off from experimental results, but there are more processes that need to be included in the models. Two different concepts for medical isotope production have been established [22,23]. Some studies have focused on understanding the ion dynamics and what species of fuel atoms are present. Finally, a helicon ion source is being developed for low-pressure operation [24].

In addition to the work of this dissertation, an alternative method for producing medical isotopes in the Wisconsin IEC device was designed by John Weidner [25]. The design involved producing a positron emitter by flowing water into the IEC device. The water filled a radiator with a large surface area in thin-walled tubes. The radiator was placed outside of the outer grid, and the tubes allowed the D-^{3}He protons to pass through to the water. Some of the ideas from that work were carried over into this project. Weidner's apparatus was able to produce 0.20 nCi of ^{13}N.

2.3 References

[1] J.A. Sorenson & M.E. Phelps (1987). *Physics in Nuclear Medicine: Second Edition*. New York: W.B. Saunders Company.

[2] J.F. Santarius, University of Wisconsin-Madison, private communication (2004).

[3] R.L. Hirsch, "Inertial-Electrostatic Confinement of Ionized Fusion Gases," *Journal of Applied Physics*, **38**, 4522 (1967).

[4] P.T. Farnsworth, "Electric Discharge Device for Producing Interaction Between Nuclei," U.S. Patent #3,258,402, patented June 28, 1966.

[5] G.H. Miley, "A Portable Neutron/Tunable X-Ray Source Based on Inertial Electrostatic Confinement," *Nuclear Instruments and Methods in Physics Research A*, **422**, 16 (1999).

[6] G.H. Miley et al., "Inertial Electrostatic Confinement: An Approach to Burning Advanced Fuels," *Fusion Technology*, **19**, 840 (May, 1991).

[7] G.H. Miley & J. Sved, "The IEC Star-Mode Fusion Neutron Source for NAA: Status and Next-Step Designs," *Applied Radiation and Isotopes*, **53**(4-5), 779 (November, 2000).

[8] I. Hrbud, Purdue University, private communication (2001), see also "IEC Research Status at MSFS," presented at The 3rd U.S.-Japan Exchange on Inertial Electrostatic Confinement, March 22-23, 2001, Huntsville, Alabama.

[9] R.A. Nebel & D.C. Barnes, "The Periodically Oscillating Plasma Sphere," *Fusion Technology*, **34**, 28-45 (1998).

[10] R.P. Ashley et al., "D-^{3}He Fusion in an Inertial Electrostatic Confinement Device," 18th IEEE/NPSS Symposium on Fusion Engineering, IEEE #99CH37050, p. 35 (October 25-29, 1999).

[11] H. Matsuura et al., "Ion Distribution Function an Radial Profile of Neutron Production Rate in Spherical Inertial Electrostatic Confinement Plasmas," *Nuclear Fusion*, **40**(12), 1951 (December, 2000).

[12] M. Ohnishi et al., "Correlation Between Potential Well Structure and Neutron Production in Inertial Electrostatic Confinement Fusion," Institute of Advanced Energy Research Report, Kyoto University, ISSN 1342-3185 (October 21, 1996).

[13] M. Ohnishi et al., "Beam Optics in Inertial Electrostatic Confinement Fusion," *Review of Scientific Instruments*, **71**(2), 1210 (February, 2000).

[14] K. Yamauchi et al., "Neutron Production Characteristics and Emission Properties of Spherically Convergent Beam Fusion," *Fusion Technology*, **39**(3), 1182 (May, 2001).

[15] M. Ohnishi, Kyoto University, Japan, private communication (2002), see also "Overview of Japanese IEC Research Program," presented at the 4th U.S.-Japan Workshop on Inertial Electrostatic Confinement, October 9-10, 2002, Madison, Wisconsin.

[16] M.J. Park, Seoul National University, South Korea, private communication (2004), see also "RF Plasma Ions Sources of Compact Neutron Generators," presented at the 6th U.S.-Japan Workshop on Inertial Electrostatic Confinement, October 20-21, 2003, Tokyo, Japan.

[17] D.C. Barnes, R.A. Nebel, & L. Turner, "Production and Application of Dense Penning Trap Plasmas," *Physics of Fluids B*, **5**(10), 3651 (October, 1993).

[18] R.W. Bussard, "Some Physics Considerations of Magnetic Inertial Electrostatic Confinement: A New Concept for Spherical Converging-Flow Fusion," *Fusion Technology*, **19**, 273 (March, 1991).

[19] N.A. Krall, "The Polywell™: A Spherically Convergent Ion Focus Concept," *Fusion Technology*, **22**, 42 (August, 1992).

[20] G.L. Kulcinski et al., "Alternate Applications of Fusion-Production of Radioisotopes," *Fusion Science and Technology*, **44**, 559 (September, 2003).

[21] J.F. Santarius, University of Wisconsin-Madison, private communication (2002), see also "Modeling D-D Operation in the UW IEC Experiment," presented at the 4th U.S.-Japan Workshop on Inertial Electrostatic Confinement, October 9-10, 2002, Madison, Wisconsin.

[22] J.W. Weidner et al., "Production of ^{13}N via Inertial Electrostatic Confinement Fusion," *Fusion Science and Technology*, **44**, 539 (September, 2003).

[23] B.B. Cipiti & G.L. Kulcinski, "Embedded D-^{3}He Fusion Reactions and Medical Isotope Production in an Inertial Electrostatic Confinement Device," *Fusion Science and Technology*, **44**, 534 (September, 2003).

[24] G. Piefer, University of Wisconsin-Madison, private communication (2003), see also "Helium Ions Source of D-^{3}He Converged Core Operation," presented at the 6th U.S.-Japan Workshop on Inertial Electrostatic Confinement, October 20-21, 2003, Tokyo, Japan.

[25] J.W. Weidner, “The Production of ^{13}N from Inertial Electrostatic Confinement Fusion,” Master’s Thesis, University of Wisconsin-Madison (2003).

Chapter 3 University of Wisconsin IEC Experiment

3.1 Experimental Facility

A schematic of the UW IEC chamber is shown in Figure 3-1 [1,2]. A cylindrical aluminum vacuum vessel measuring 75 cm high and 100 cm in diameter houses the system. The pumping system consists of a Leybold Trivac® rotary vane roughing pump and Dyna-Tech® turbo pump (1000 L/s) to allow base pressures in the low to mid 10^{-7} torr range. The base pressure is measured using an MKS® ion guage.

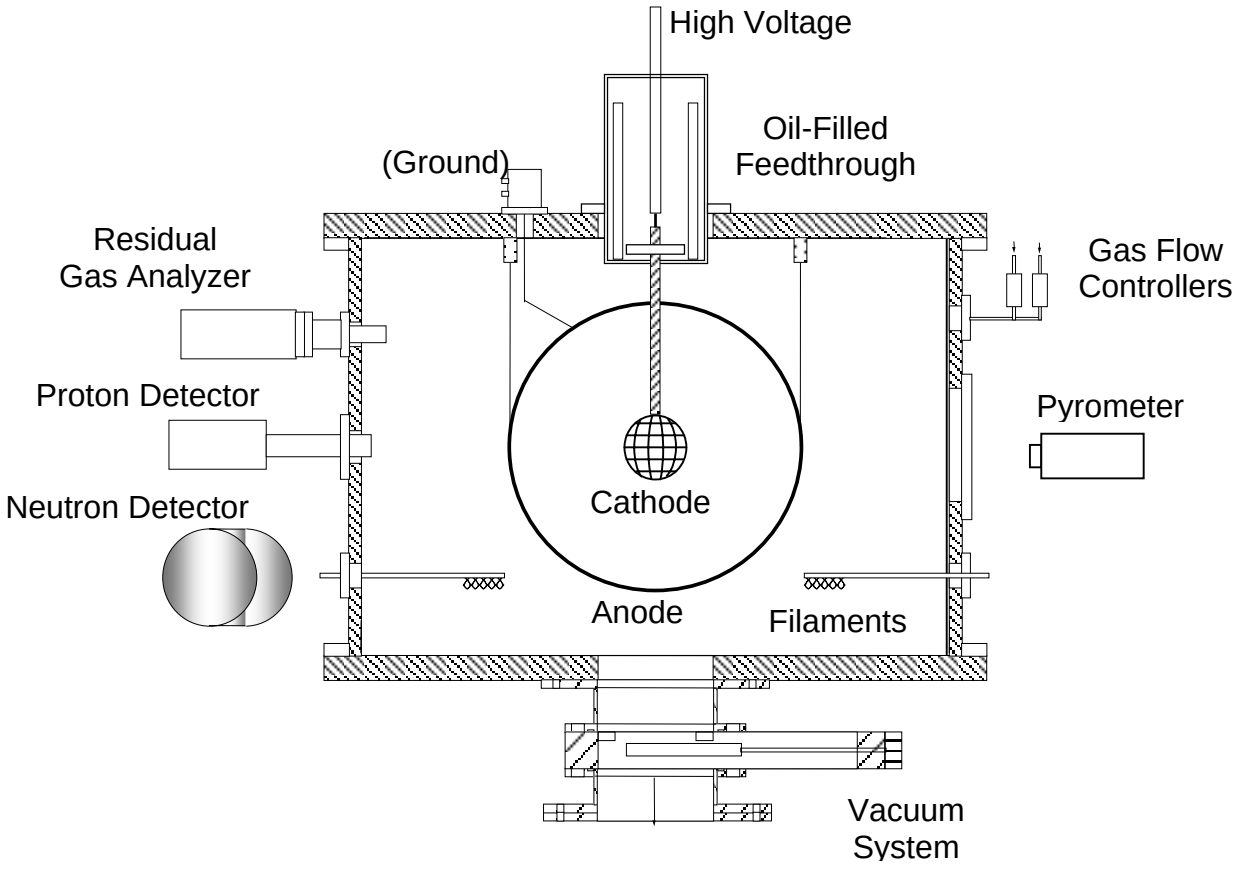

Figure 3-1: UW IEC Experimental Setup

The gas line system contains two MKS Mass-Flo® controllers for both deuterium gas and helium-3 gas. The controllers allow for fine adjustment of the gas up to 50 sccm

(standard cubic cm per minute) into the chamber. During runs, an MKS Baratron® pressure transducer measures the neutral gas pressure in the chamber. Typical run conditions for this project use a 2 mtorr background pressure. A Stanford Research Systems CIS 200® residual gas analyzer determines which gases are present in the chamber. It helps to determine ratios when running two gases and helps to determine if there are leaks in the system.

The 10 cm diameter inner cathode is fabricated from a tungsten-rhenium wire that allows for high temperature operation. A typical grid is shown in Figure 3-2. The outer grid is fabricated from stainless steel wire and remains grounded. A high voltage insulator carries the large negative potential to the inner grid. The present design uses a 3 mm molybdenum or tungsten rod inside a 2 cm cylinder of boron nitride. The Boron nitride is used for its large voltage standoff capability. The high voltage power supply is a Hipotronics® supply with maximum capability of 200 kV and 75 mA. The voltage supply runs through a set of resistors, a total of 200 kΩ, in an oil bath, to stabilize the system during voltage surges and spikes.

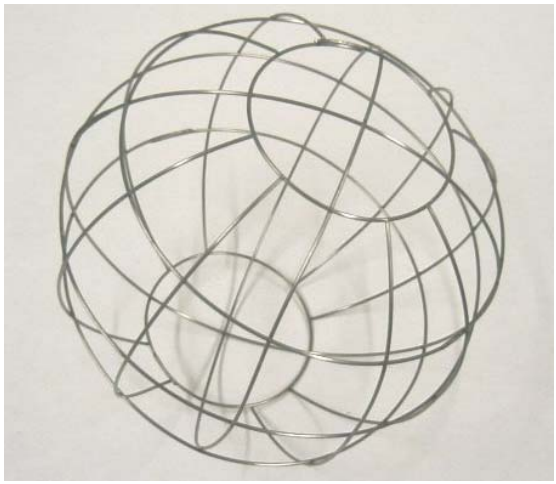

Figure 3-2: 10 cm Tungsten-Rhenium Inner Grid

Three standard 200 W light bulb filaments are used outside of the outer grid to produce electrons that ionize the fusion gases. A variac controls the intensity of the filaments (0-120 V) to vary the current during experiments. The filaments are rectified during runs, and at higher voltages, a positive bias is added to the filaments to drive the electrons away and enable better ionization. This also allows for more control of the current.

A helium-3 filled neutron detector in a paraffin shield counts neutrons generated in the chamber. The detector is calibrated using a Pu-Be known neutron source. The source is placed in the center of the chamber, and the distance of the detector from the chamber (~ 2 m) justifies using a point source for calibration.

The protons are detected with a Canberra® 1200 mm^2 silicon detector on a port facing the center of the chamber, and accompanying multi-channel analyzer (MCA) software. The MCA allows for the detection of the D-D and D-^{3}He protons based on the amount of energy the protons are able to deposit in the thickness of the detector. A thin lead foil protects the detector from some x-ray noise. Figure 3-3 is a schematic of the energy loss through the foil and detector. About 1.9 MeV is deposited in the silicon from the D-D protons, and about 5 MeV is deposited from the D-^{3}He protons.

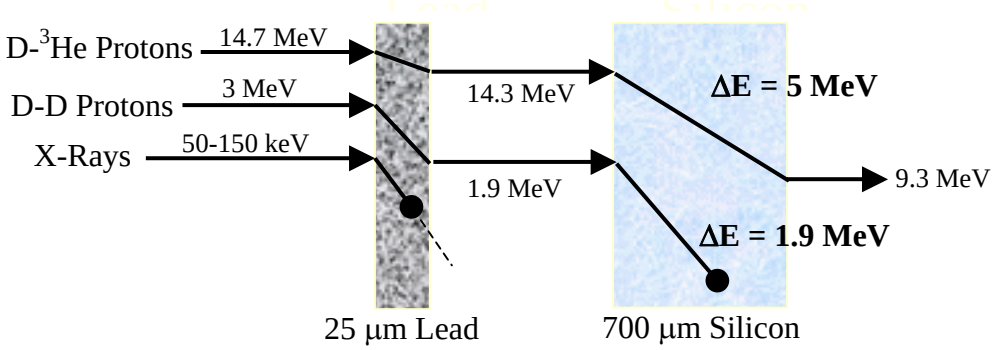

Figure 3-3: Proton Energy Loss through Lead Foil and Detector

The proton detector was calibrated originally using MCNP (Monte Carlo) methodology for a volume source of protons. A rough calculation is shown in Appendix A. Since part of the purpose of this research was to determine a new calibration factor, this calibration is only used as a reference.

Additional view ports are added to the chamber as well. A digital video camera, connected to a computer in the control room, allows for visual monitoring of the operation. A Raytek® Marathon MR pyrometer can be pointed to different areas on the cathode to determine temperatures from 700°C to 1800°C.

The chamber, diagnostics, and high voltage power supply are all located in a radiation-shielded room. Reinforced concrete walls, 1 meter thick, and a lead door separate the control room from the device. Radiation meters monitor the radiation in the chamber room and control room. An interlock system prevents the high voltage from running when the shielded door is open.

3.2 References

[1] R.P. Ashley et al., "Steady State D-^{3}He Proton Production in an IEC Fusion Device," *Fusion Technology,* **30**(2), 546 (March, 2001).

[2] R.P. Ashley et al., "Recent Progress in Steady State Fusion using D-^{3}He," *Fusion Technology,* **44**(2), 564 (September, 2003).

Part I: Source Regimes

Chapter 4 Source Regime Theory

Fusion reactions within an IEC device can occur in many different modes: beam-beam, beam-background, beam-target, and fast neutral-background. These four modes were first outlined with respect to the UW IEC by the work of Thorson [1]. Beam-beam reactions are due to two accelerated ions fusing with one another. Beam-background reactions are due to an accelerated ion fusing with a background gas molecule. Beam-target reactions occur when ions implant into a solid component such as the cathode; further bombardment by ions can result in fusion reactions within the cathode material. Finally, fast neutral-background reactions occur when an ion charge-exchanges with a background gas atom—the resulting fast neutral can then fuse with the background gas. It is important to understand how all of these modes influence the reaction rates both for a better understanding of the physics involved, and for any potential use of the fusion products.

These four modes have been condensed into three source regimes (see Figure 4-1) to be evaluated with experimental data. The converged core regime involves reactions that occur in the center of the device or very near the inner grid. It includes both beam-beam and beam-background reactions. The volume source regime involves fast neutral-

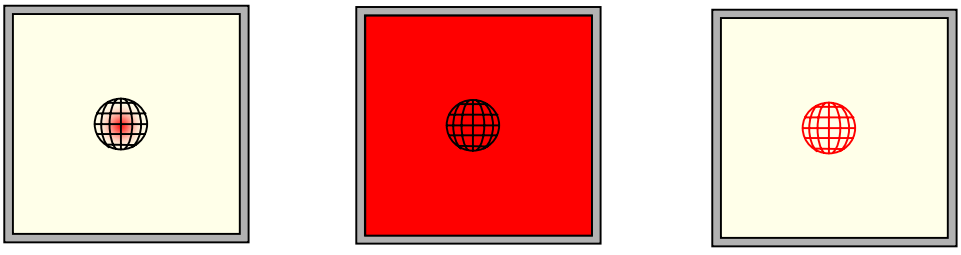

Figure 4-1: Source Regimes (Red Areas Indicate Where Fusion Reactions Occur)

background reactions that can occur distributed throughout the entire vacuum chamber. Lastly, the embedded regime involves beam-target reactions occurring when ions fuse with implanted ions in the cathode grid.

Thorson gave the total system fusion reaction rate (R_{fus}) as [1]:

$$R_{fus} = 4\pi \int_0^{\rho} r^2 dr n_f(r,v) \left(n_o \overline{\sigma_f v(r)_o} + \frac{n_f(r,v)}{4} \overline{\sigma_f v(r)_f} \right) + R_{fus,cat} \qquad \text{(Eq. 4-1)}$$

In this equation, ρ is the radius of the reaction volume, n_f is the sum of the fast ion and fast neutral density, n_o is the background gas density, $\sigma_f v(r)$ is the averaged fusion reactivity, and $R_{fus,cat}$ is the reaction rate from beam-target reactions in the cathode. The first term in the integrand represents beam-background and fast neutral-background reactions. The second term represents beam-beam reactions, and the third term represents embedded reactions.

4.1 Converged Core Regime

In the converged core regime, fusion takes place due to the accelerated ions colliding with other ions or background gas molecules only in the center of the device. This regime is the more intuitive of the various modes of operation. In the long term, this regime is also the most desirable for device performance. Building up a high density in the center of the device, and thus increasing the converged core mode, is probably the only way that IEC may be developed into a fusion power source. The accelerated ions have the most energy close to or within the cathode grid, so the volumetric reaction rate is much stronger near the center of the device.

The radial electrostatic potential profile is believed to be nearly Child-Langmuir [2]. The ion current follows the Child-Langmuir law for space-charge limited current in spherical geometry:

$$I_{CL} = \left(\frac{16\pi\varepsilon_o}{9}\right)\left(\frac{2ze}{m}\right)^{1/2}\left(\frac{V_o^{3/2}}{\alpha^2}\right) \qquad \text{(Eq. 4-2)}$$

The voltage between the grids is V_o, z is for the ion of interest, and α has a complex dependence on the ratios of the radii of the grids. The mass of the ion is included as m, the electron charge is e, and the permittivity constant is ε_o. Equation 4-2 can be used to determine the potential profile using numerical methods. Figure 4-2 shows the calculated potential profile as a function of radius for a 100 kV inner grid potential using the UW IEC grid parameters. The ions gain most of their final energy in the last few centimeters before reaching the inner grid radius. Therefore, the cross-section for fusion is much stronger towards the center of the device. In addition, the ions are converging with radius as $1/r^2$, so the density in the center is much higher. Both of these effects result in a small core in which most of the reactions occur.

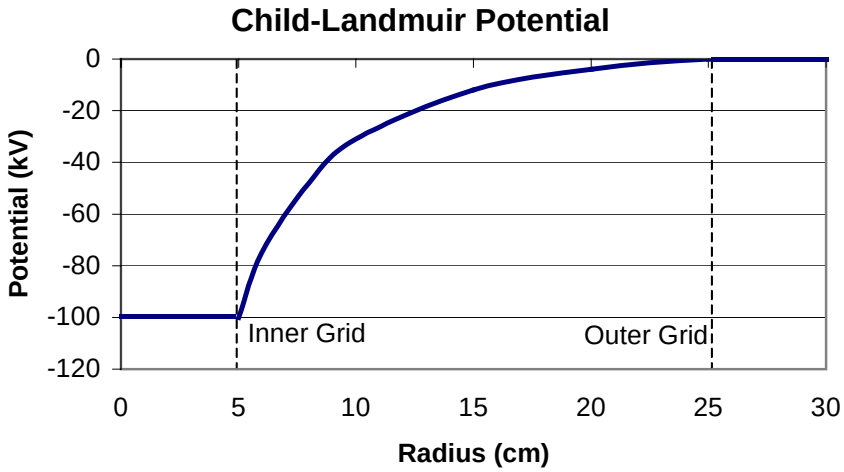

Figure 4-2: Child-Langmuir Potential for 100 keV IEC Cathode [3]

The converged core regime is strongly pressure dependent. Pressure affects the chance for collision of the ions with a background gas molecule on the trip into the center of the device. More collisions will cause charge exchange reactions creating a fast neutral and slow ion. The slow ion will continue to get accelerated towards the center but with a much lower final energy. Higher pressures will, in effect, decrease the converged core regime. At the typical run conditions of 1-10 mtorr in the UW IEC, Thorson showed that the neutral gas density ($\sim 10^{20}$ m^{-3}) is much higher than the fast ion density in the core ($\sim 10^{15}$ m^{-3}) running D-D [1]. Therefore, the beam-background interactions are much more dominant than the beam-beam interactions in those operating conditions.

4.2 Volume Source Regime

The volume source regime is mainly governed by charge exchange reactions. If an ion collides with a background gas molecule and charge exchanges, it creates a fast neutral moving with high energy. Charge exchange reactions do not modify the original path of the ion, so the fast neutral travels in the same direction [4]. This fast neutral is unaffected by the electrostatic potential within the IEC so has equal probability for fusion at any point along its path until it hits the chamber wall.

The cross-section for fusion is independent of radius for the fast neutrals, but the current density is not. Since the fast neutrals are all traveling either through the center and out of the core or just directly out of the core, the current density of the neutrals is dependent on radius. Therefore, the volume regime should have a $1/r^2$ dependence.

Figure 4-3 shows the reaction rate as a function of energy for the D-D and D-^{3}He reactions. The plots show the variation of the reaction rate cross-section with voltage.

The two lower curves are for fast neutral fusion reactions and they illustrate that an order of magnitude or more in the reaction rate can be lost when operating in this mode. This puts the volume source reactions at a disadvantage from the converged core reactions. However at the background pressures around 1-10 mtorr, it is more likely that an accelerated ion will have a charge-exchange reaction with the background neutral gas than fuse with another energetic ion. At these pressures, the mean free path for charge exchange reactions is on the order of or somewhat larger than the device dimensions [5]. The ions only make a few radial passes before charge exchanging or hitting the inner grid. These factors limit the converged core reaction rate but add to the volume regime.

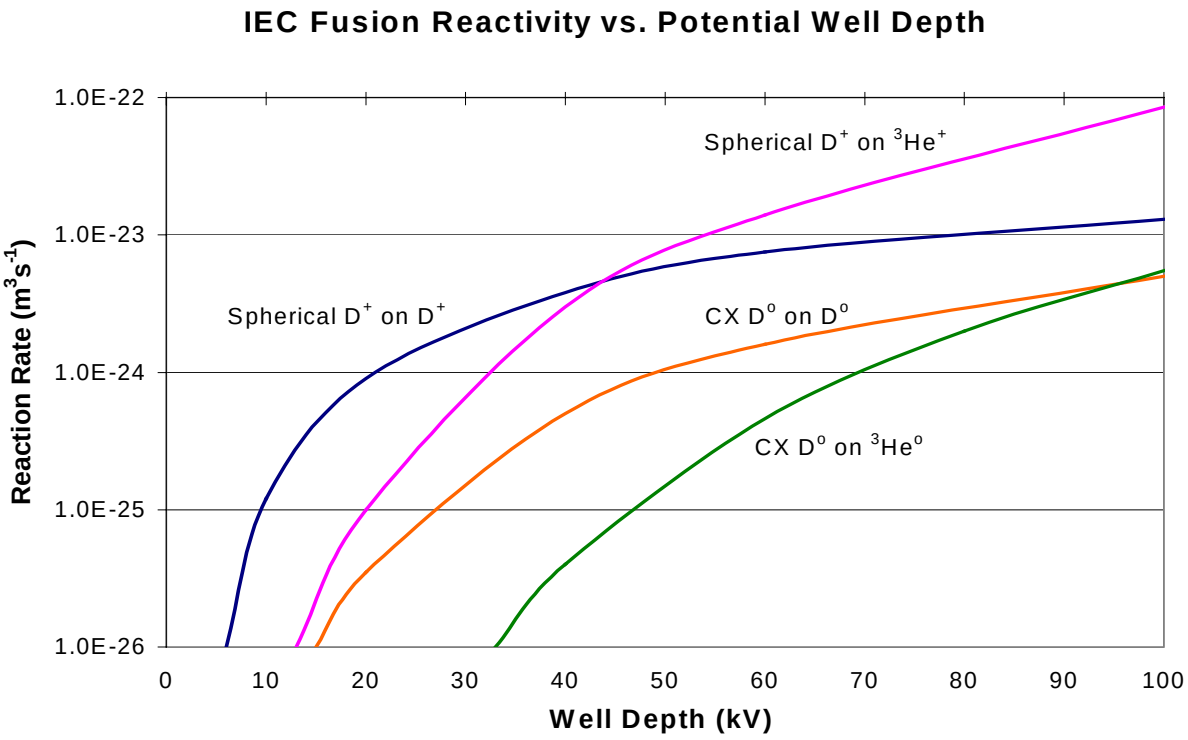

Figure 4-3: Reactivity Difference Between Ion-Ion and Neutral-Neutral Reactions [5,6]

4.3 Embedded Regime

The embedded reaction regime is so named because of the ions that get implanted into the cathode. There is a fairly significant ion current (~2 mA) streaming into the cathode grid wires during normal IEC operation. These ions can build up the atomic density in the cathode to significant amounts. Continued bombardment by fusion ions can then result in beam-target reactions within the grid wires.

4.3.1 Previous Work

Thorson first set up experiments on the Wisconsin IEC device to determine the beam-target contribution for a D-D plasma [1]. The result was that ≤ 10% of the total reaction rate appeared to be from the embedded regime at the optimal operating pressures. Because of the small fraction of the embedded regime contribution, this topic was not pursued at the time. It should be noted the voltage range (<50 kV) was much lower than the ones currently reached by the UW IEC (up to 180 kV). Also, because the work only used the D-D reaction, the contribution of the D-^{3}He reaction was not known.

Fusion reactions occurring within a metal is not a new or unique area. The Rotating Target Neutron Source (RTNS) at the University of California, Berkeley uses beam-target D-T reactions to produce up to $6x10^{12}$ n/s using a 400 kV deuteron beam [7]. The D-^{3}He reaction is also used in Nuclear Reaction Analysis to determine amounts of deuterium in materials. A helium-3 beam directed at a surface with deuterium embedded in it will generate fusion reactions that can be measured.

Very recently, the IEC project at Kyoto University altered the traditional gridded setup to create a beam-target neutron source [8]. A water-cooled titanium target was

placed in the vacuum vessel with a negative bias on it. A multi-cusp ion source generated deuterium ions to implant in the target. At 58 kV, with 12 mA deuterium ion current, the group produced 5.2×10^7 n/s. Their goal is to use this as a small, compact neutron generator.

4.3.2 Theoretical Modeling

It is straight-forward to determine the reaction rate expected in a beam-target experiment. The reaction rate is a function of the beam current impinging the target, ion implantation density within the target, beam energy, material stopping power, and finally the fusion cross-section. The stopping powers and fusion cross-sections are well known from empirical data. The beam current can be measured, but secondary electron emission can play a role in masking the true ion current. The fact that the beam energy is not mono-energetic also complicates matters. The ion implantation density may be the most difficult aspect to estimate accurately unless some other method is used for measurement of the spatial distribution of implanted atoms.

The reaction rate can be determined from integrating the following differential equation [9]:

$$\frac{dN(x)}{dt} = I \cdot n_{fi}(x) \cdot \sigma_{fus}[E(x)]dx \qquad \text{(Eq. 4-3)}$$

$\frac{dN(x)}{dt}$ is the fusion reaction rate in s^{-1}, I is the beam current in ions/s, and n(x) is the embedded ion density as a function of depth (x). The cross-section (σ) is a function of energy (E) of the bombarding ion, which in turn is a function of depth and initial beam energy. The energy at depth x, E(x), is found using the initial beam energy and stopping

power functions for the target material of interest. This equation can be integrated to solve for the total reaction rate if a closed form can be found. Otherwise, it is simple and fairly accurate to use a numerical method to solve the integration. Part III will discuss how Equation 4-3 was used in a computer program to model the embedded reaction rate.

4.4 References

[1] T.A. Thorson et al., "Fusion Reactivity Characterization of a Spherically Convergent Ion Focus," *Nuclear Fusion,* **38**, 495 (1998).

[2] I. Langmuir & K.B. Blodgett, "Currents Limited by Space Charge Between Concentric Spheres," *Physics Review*, **24**, 49 (1924).

[3] J.F. Santarius, University of Wisconsin-Madison, private communication (2002), see also "Modeling D-D Operation of the UW IEC Experiment," presented at the 5th U.S.-Japan Workshop on Inertial Electrostatic Confinement, October 9-10, 2002, Madison, Wisconsin.

[4] K. Miyamoto (1997). *Fundamentals of Plasma Physics and Controlled Fusion,* Tokyo, Japan: Iwanami Book Service Center.

[5] R.P. Ashley et al., "D-^{3}He Fusion in an Inertial Electrostatic Confinement Device," 18th IEEE/NPSS Symposium on Fusion Engineering, IEEE #99CH37050, October 25-29, 1999, p. 35.

[6] H.S. Bosch & G.M. Hale, "Improved Formulas for Fusion Cross-Sections and Thermal Reactivities," *Fusion Technology,* **32**, 611 (1992).

[7] D.W. Heikkinen & C.M. Logan, "Recent Progress at RTNS-II," *Nuclear Instruments and Methods in Physics Research*, **B10/11**, 835 (1985).

[8] T. Tadokoro, Hitachi Ltd., private communication (2002), see also "Development of Compact Neutron Generators by using Ion Sources," presented at the 4th U.S.-Japan Workshop on Inertial Electrostatic Confinement, March 25-26, 2002, Kyoto, Japan.

[9] J.A. Sorenson & M.E. Phelps (1987). *Physics in Nuclear Medicine: Second Edition*. New York: W.B. Saunders Company.

Chapter 5 Source Regime Experimentation

Three different types of experiments were used to determine the source regimes in the IEC device:

1. Embedding experiments quantified the beam-target reaction regime, reactions occurring within the cathode.
2. Eclipse experiments were designed to determine the source location of the protons that were detected in the proton detector. Three different discs were rotated in front of the proton detector to block out different areas.
3. Off-axis experiments used an additional proton detector that looked away from the center of the chamber to compare to the on-axis detector.

None of the individual experiments were able to answer all the questions; rather, it took all three to unfold the different regimes.

5.1 Embedding Experimentation

5.1.1 Grid Experimentation

Embedded fusion reactions are dependent on the number density of the implanted ions within the cathode material. Therefore it takes a certain amount of time for the cathode to get saturated from the ion flux. The embedding experiments used this fact to determine the contribution of embedded reactions to the total reaction rate.

Experiments were run using a new, virgin grid. This insured that the grid wires started off with no deuterium or helium-3 ions present. To determine the effect of deuterium embedding, the new grid was used for back-to-back voltage scans using only

deuterium in the chamber. The experiment looked for an increase in D-D rates over time with implantation density increase. During a typical run, the ion density increases to some maximum saturated point. An embedded regime is indicated by an increase in the rates with run time.

Similar experiments were run with D-^{3}He to look for an increase in rates with experiment time. The results were correlated to total fluence hitting the grid. In addition to the multiple voltage scans, an experiment was setup to run D-^{3}He at a constant condition. After a new grid was conditioned with only deuterium, ^{3}He was introduced into the chamber and the voltage was increased to a high level. That level was maintained, and counts were taken over time to measure the rate increase.

5.1.2 Solid Cathode Experimentation

As a follow up study to the embedding experiments, the cathode grid was replaced with solid, non-transparent metal cathodes. The solid cathodes attract all of the ions into the surface, and no re-circulation occurs. In this manner, fusion reactions should only take place due to the embedded regime. These experiments were set up both to understand the implantation of the fusion gases better and to determine the effects of different materials.

Three metal cathodes were used: tungsten, titanium, and molybdenum. The cathodes are shown in Figure 5-1. The figure also shows how the targets were mounted in the IEC chamber. All three targets were designed with a protrusion and hole at the top for mounting on the bottom of the stalk. The tungsten target was not fabricated in the

same shape as the others due to the machining difficulties of pure tungsten. The titanium and molybdenum were fabricated as spheres.

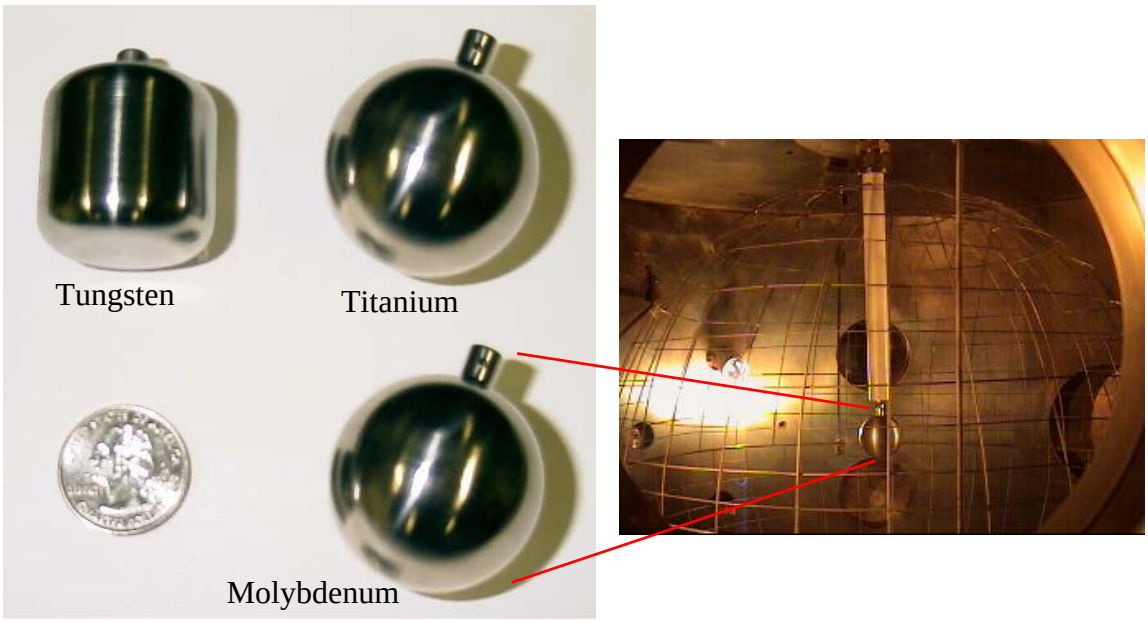

Figure 5-1: Solid Tungsten, Titanium, and Molybdenum Cathodes

A number of various experiments were run with these targets installed. The order of the experiments was important, so it was repeated for all three targets. It usually took a few deuterium runs to get the target conditioned, and some changes were made in the mounting of the targets. The first run in each series was a voltage scan to study only the D-D reaction rate. The next run was with only helium-3 flowing into the chamber. The purpose of the run was to measure the D-^{3}He rates as they only could have been due to ^{3}He on embedded D reactions, thus giving an indication of the amount of deuterium in the target. The third run was with only deuterium again. The D-^{3}He rate could only have been due to D on ^{3}He reactions, thus giving an indication of the amount of helium-3 in the cathode. Finally deuterium and helium-3 were run together.

5.2 Eclipse Experiments

The on-axis proton detector is mounted on a side port of the IEC chamber looking directly into the center of the device where the cathode is located. The purpose of the eclipse experiments was to block out portions of the solid angle view of the detector to determine the impact on the proton rates. Most of the work on designing the eclipse experiments was done by S. Krupakar Murali of Wisconsin.

Three eclipses were made, all circular in shape, from 0.13 cm thick aluminum sheet. Their sizes were 8.0 cm, 4.8 cm, and 2.2 cm in diameter. The thickness of the aluminum is enough to completely stop the 3.0 MeV D-D protons, but only slow down the 14.7 MeV D-^{3}He protons by 6.7 MeV. The eclipsed D-^{3}He protons, although at a lower energy, are able to deposit more energy in the proton detector, so they show up as a higher energy peak. A comparison of the counting rates to non-eclipsed runs (and thus a comparison of the peak heights) at the same conditions determined the effect of the eclipses.

Figure 5-2 shows the positioning of the eclipses in the chamber. The top figure shows the large eclipse in place and how it blocks the solid angle of the proton detector. The large eclipse is designed to block the entire cathode. The medium eclipse blocks most of the center of the cathode, but still leaves many of the grid wires exposed around the sides. The small eclipse only blocks the small core of the cathode. In this manner, the eclipse experiments were used to block out various regimes. The large eclipse blocked out both the converged core and embedded regimes. The medium and small eclipse blocked out portions of the core regime, but did not block much of the embedded

regime since most of the grid wires could still be seen. Comparing the results with the eclipses in place to results without the eclipses gave an indication of the source regimes.

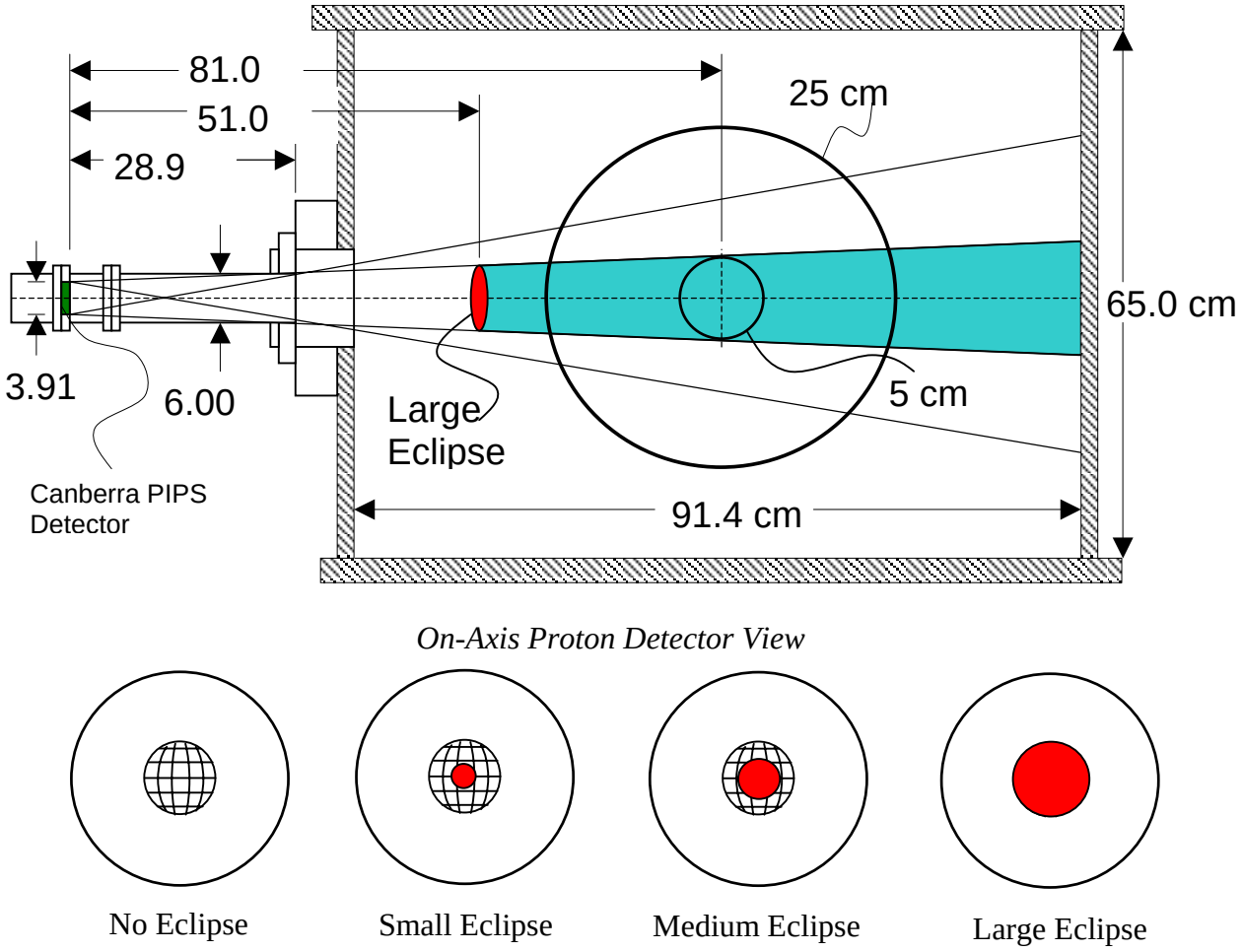

Figure 5-2: Portions of the Proton Detector View Blocked with Eclipses

One of the drawbacks of this experimental method is that it used a 2-D eclipse to block out a 3-D system. The large eclipse for example will block out the grid and core, but it also blocks out the volume in front of and behind the grid. This drawback is part of the reason why this experiment alone could not completely unfold the source regimes.

5.3 Off-Axis Experiments

The off-axis proton detector is similar to the on-axis except for a 450 mm^2 surface area. It is oriented as shown in Figure 5-3. Because this detector does not see the inner grid or core of the device, it can only see volume source reactions. A calibration factor was calculated for this detector. The solid angle the off-axis detector sees was modeled in the Solid Works™ modeling program. The program was used to help split the solid angle into sections for a piece-wise calibration factor. The calibration factor was found to be 200,000. Appendix A shows the detailed calculation of this calibration. This number converts raw counting rate (in p/s from the proton detector) into the total volume source reaction rate in the chamber. In other words, for every proton detected there are 200,000 reactions occurring in the volume regime.

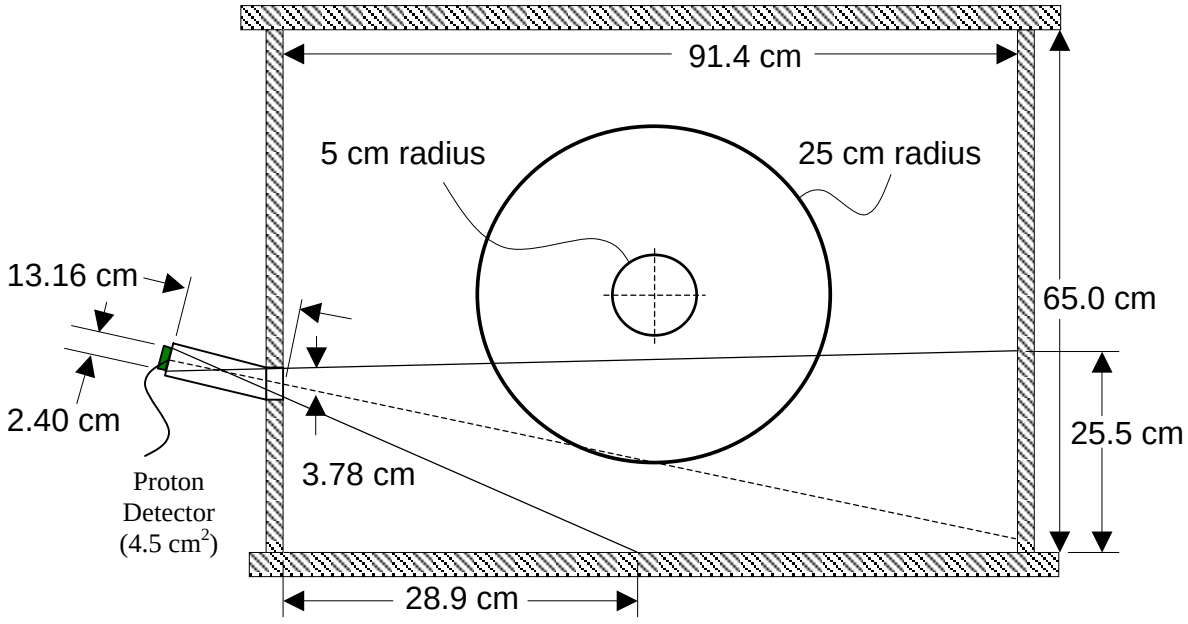

Figure 5-3: Off-Axis Proton Detector Orientation

Using the off-axis counts along with the calibration factor gave a total reaction rate for the entire chamber from the volume source. This volumetric reaction rate was then used to determine the portion of the on-axis detector counts due to the volume source. The rest were due either to the core or embedded regimes. In this manner, the off-axis experiments were used to break down the volume source regime.

Chapter 6 Source Regime Results

6.1 Embedding Experimental Results

The first evidence for embedded reactions was seen with D-D runs following D-^{3}He runs. Even though no helium was flowing into the chamber, a D-^{3}He peak was still seen. This result suggested that helium was implanted in the cathode of the device, and deuterium bombardment caused the reactions to occur. Likewise, a small D-^{3}He peak was also seen in helium only runs after previous run time with deuterium. Figure 6-1 shows the evidence clearly.

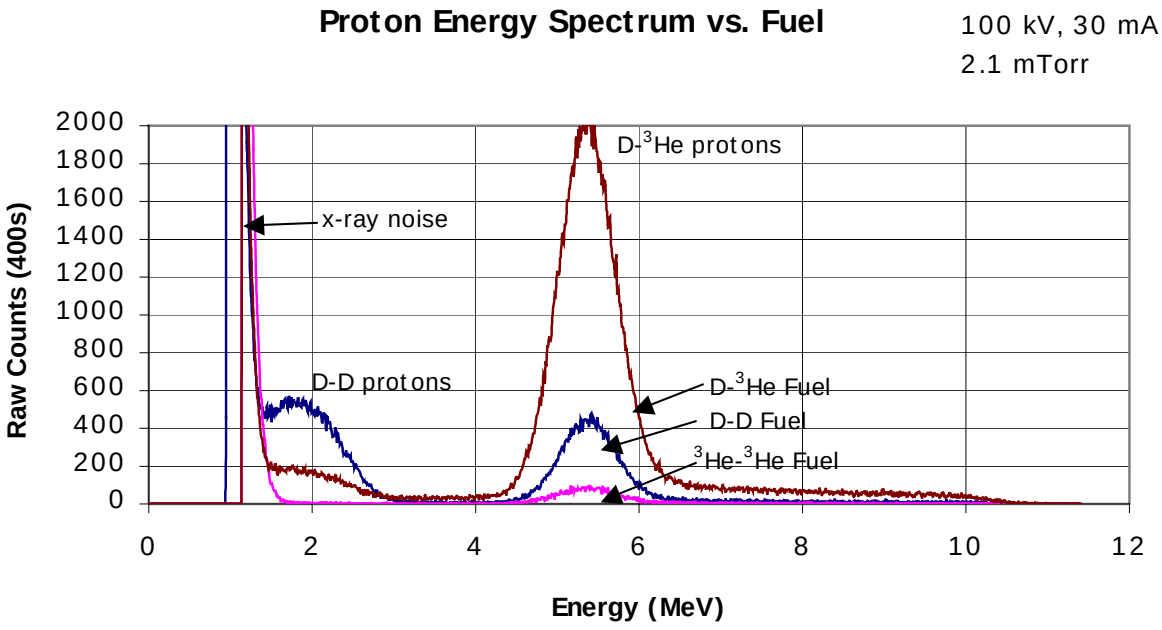

Figure 6-1: Evidence for Embedded Fusion Reactions; D-^{3}He Protons are Measured While Running Only Deuterium or Only Helium-3 in the Chamber

This figure shows the proton energy spectrum from the proton detector for three different fuel mixtures at the same voltage and current (100 kV, 30 mA). The peaks just above 5 MeV are where the D-^{3}He protons show up. The largest peak is from a typical

D-^{3}He run with equal amounts of both gases. The next peak is from a D-D run with only deuterium gas present, and the small peak is from a ^{3}He-^{3}He run with only helium-3 gas present. This figure suggests that both helium and deuterium are implanted into the cathode.

6.1.1 Grid Results

To determine embedded reactions in the cathode for the D-D reaction, a new tungsten-rhenium grid was installed in the chamber, and consecutive voltage scans were performed. Five scans were completed at a constant 30 mA and 2 mtorr background pressure. Figure 6-2 shows a plot of the neutron rates as a function of run time for each voltage. Since the meter current was kept constant, the x-axis can be thought of as being proportional to the total deuterium fluence into the grid. Figure 6-3 shows the plot of D-D proton counts as a function of run time for the same set of experiments.

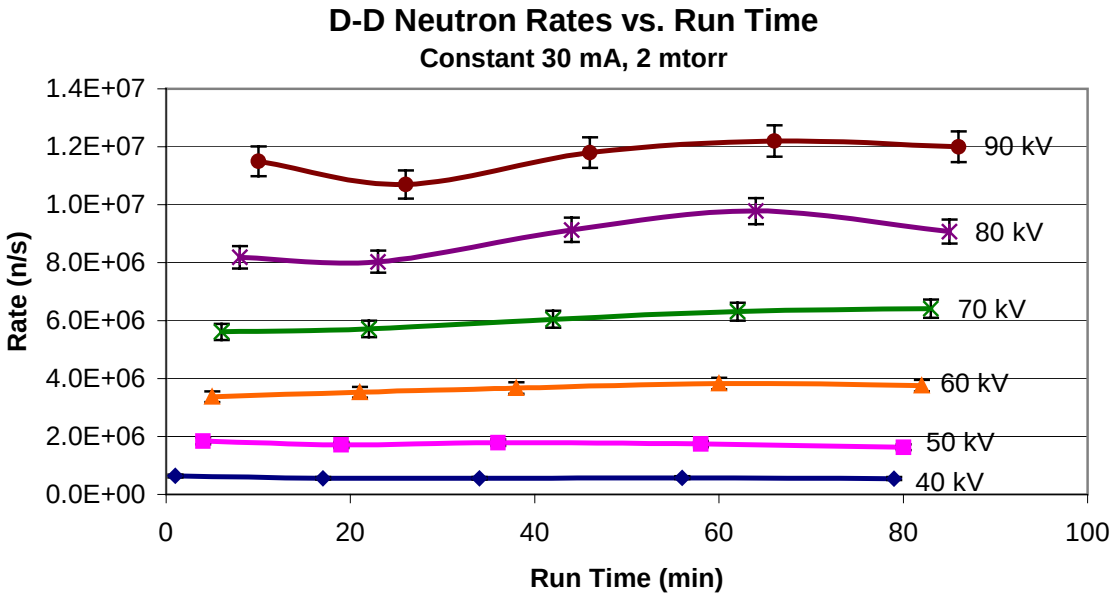

Figure 6-2: Effect of Run Time on D-D Neutron Rates Using a New Grid

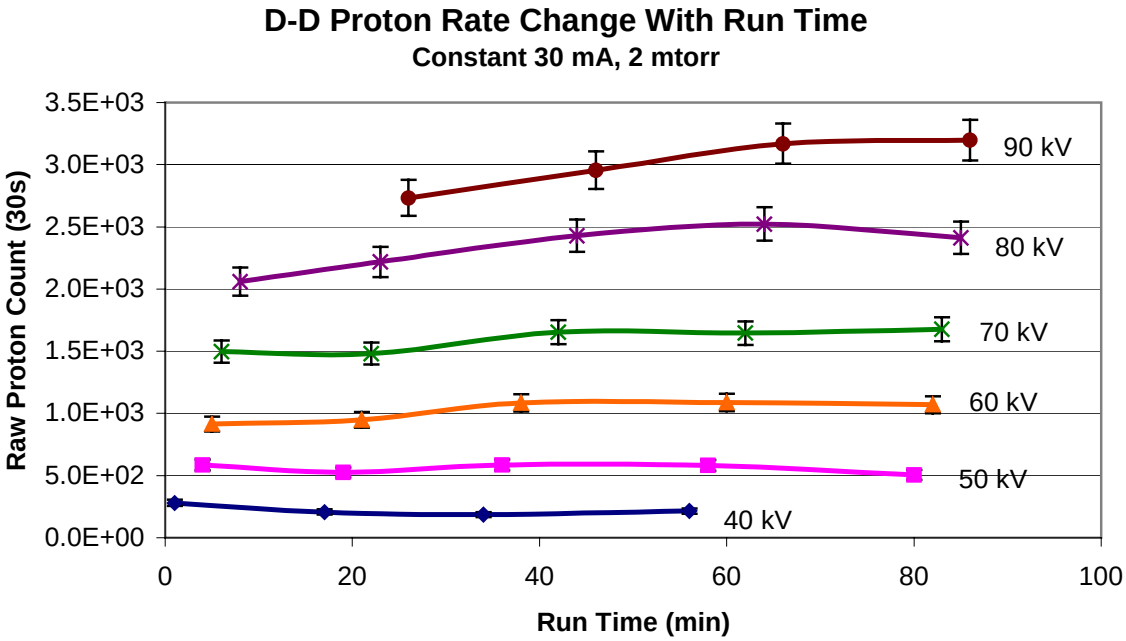

Figure 6-3: Effect of Run Time on D-D Proton Rates Using a New Grid

Both graphs show a slight increase in rates at the higher voltages and little or no increase at the lower voltages. The uncertainty in the data is due to counting uncertainties and ± 1 mA fluctuations in the current during runs. The slight increase in both graphs is beyond the error bars. Over the time range of the data points, the neutron rates increased on average about 10% in the 60-90 kV range. The proton rates increased on average 16% over that same range. It does make sense that the proton rate should increase more than the neutron rate from an increase in the embedded regime. The proton detector "sees" the entire grid and only part of the volume regime, so an increase in the embedded rate will lead to higher numbers. The neutron detector "sees" the entire chamber.

The D-^{3}He reaction behaved differently with the voltage scans. The first embedded experiment was carried out with a grid that had never been run with helium-3

before. Five consecutive voltage scans from 40 to 80 kV were run and the D-^{3}He rate was recorded at each point. Figure 6-4 shows the results of the experiment. A significant increase in the rates is observed over time.

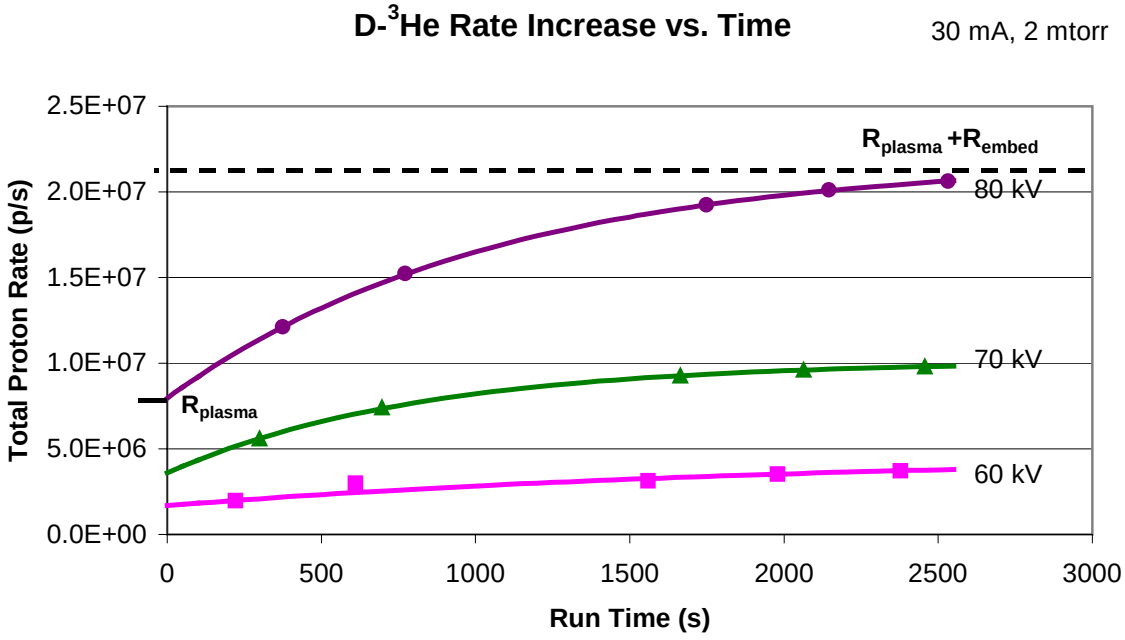

Figure 6-4: Effect of Run Time on D-^{3}He Proton Rates Using a New Grid

The rates appear to follow a saturation trend in that they level off with time. Exponential saturation equations were fit to the data following the form:

$$R_{total} = R_{plasma} + R_{embed}(1 - e^{-\lambda t}) \qquad \text{Eq. 6-1}$$

This form assumes two things. First, there is a starting reaction rate (R_{plasma}) that is due to the D-^{3}He reactions occurring within the plasma. Second, the rate increase is due to reactions occurring within the grid due to implanted ^{3}He ions that get bombarded by D ions. In this equation, R_{total} is the total reaction rate at time t. R_{embed} is the maximum portion of the rate due to embedded reactions. The saturation constant is λ.

Using these best-fit lines for each voltage, the maximum embedded portion of the rates was determined. For all three voltages, 64% of the maximum reaction rate was due to embedded reactions. This means that approximately 2/3 of the maximum reaction rate was due to the embedded reaction regime. There are a couple of errors in this experiment that are important to point out. First, because the voltage scan started with 40 and worked up to 80 kV, some run time passed before the first higher voltage points were taken. This might have had an influence on the extrapolated starting rate. Second, during the experiment, the ^{3}He ions implanted at different depths with different voltages. The deuterium ions have the highest energy at the shallower depths. Therefore a smaller number density at the shallower depths will decrease the rates.

Another experiment was used to compare to the previous one. With a new grid installed in the chamber and conditioned with only deuterium, a time scan was performed with D-^{3}He. In this case, though, the voltage was immediately set to 100 kV for the first D-^{3}He run and held there over time (at 30 mA). The rates as a function of time are shown in Figure 6-5.

The rates seemed to level off around 31,000 counts per 60 s. The rates started around 3,000 counts, which indicates a factor of ten increase. This result suggests that 90% of the maximum D-^{3}He counting rate comes from embedded reactions. It is worth noting that this data was taken over two experiments as indicated by the dashed line. Since the graph stayed continuous, it was an indication that the helium did not diffuse out of the grid wires after shutting down for a few hours. Although the results from Figure 6-5 did not agree with the results shown in Figure 6-4, Figure 6-5 is probably more reliable since the voltage did not change.

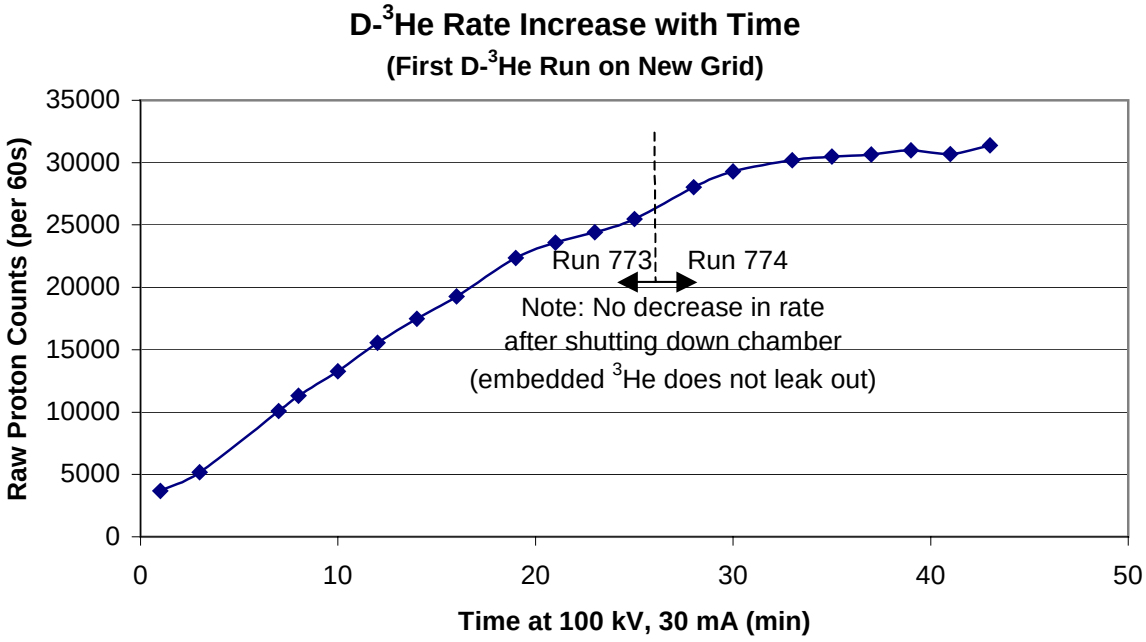

Figure 6-5: D-^{3}He Increase with Run Time on a New Grid Conditioned with Deuterium

The results of the grid experiments show that deuterium does not seem to build up to as high of densities in the W-Re grid wires as does the helium. This conclusion explains why the D-D rates do not increase much with time with a new grid, whereas the D-^{3}He rates increase substantially over the period of the run. The difference between implanted deuterium and helium is explored more in Part III.

One additional fact to explore is the possibility that the rate increase is not only due to implanted ions in the cathode. It had been suggested that some ions could implant in the chamber walls or outer grid to allow fusion reactions upon further bombardment. However, even after running many D-^{3}He experiments in the device and then replacing the cathode with a new W-Re grid, a D-D run will produce zero D-^{3}He protons. Either helium does not implant into the walls (or outer grid), or the amount is too small to allow for significant reactions.

6.1.2 Target Results

The solid cathode experiments were used both to compare to the grid reaction rates and to determine the effect of cathode material on ion retention. The assumptions of the experiment were that ions were implanted into the outer surface of the cathode. Further bombardment caused the reactions to occur at the surface. The neutrons generated by the D-D reaction were representative of a point source since the neutron detector was far away. The protons also acted like a point source, except protons born on the far side of the target (from the proton detector) did not reach the detector. Therefore, the proton detector used a shadowed point source calibration factor. These factors were used to calculate the total fusion rates shown in the following results.

Because the targets were subjected to a large ion flux, they heated up substantially. Figure 6-6 shows the molybdenum target during a run. The color in the figure is slightly distorted, but the target does glow at a bright orange color during high power conditions. A pyrometer external to the chamber measured the target temperature.

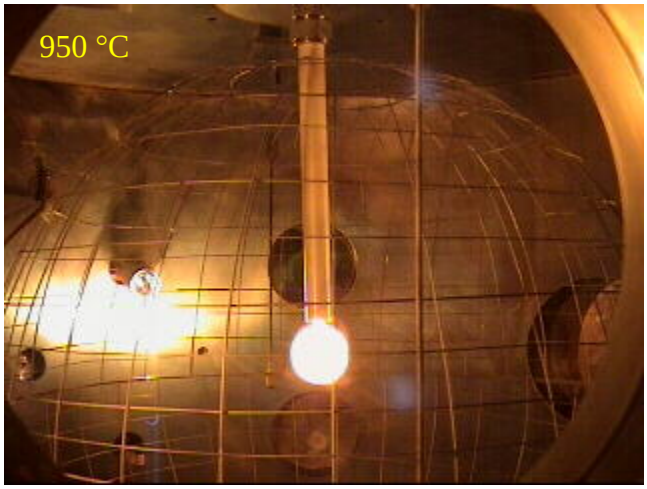

Figure 6-6: Solid Molybdenum Cathode at 70 kV, 30 mA

For all three solid targets used (tungsten, titanium, and molybdenum), two conditioning runs with only deuterium were conducted to start. These runs were used both to check out the diagnostics and to drive out impurities in the system. A D-D voltage scan was then performed for each target, and both neutron and proton data were taken. Figure 6-7 shows the D-D neutron production rate for the three targets.

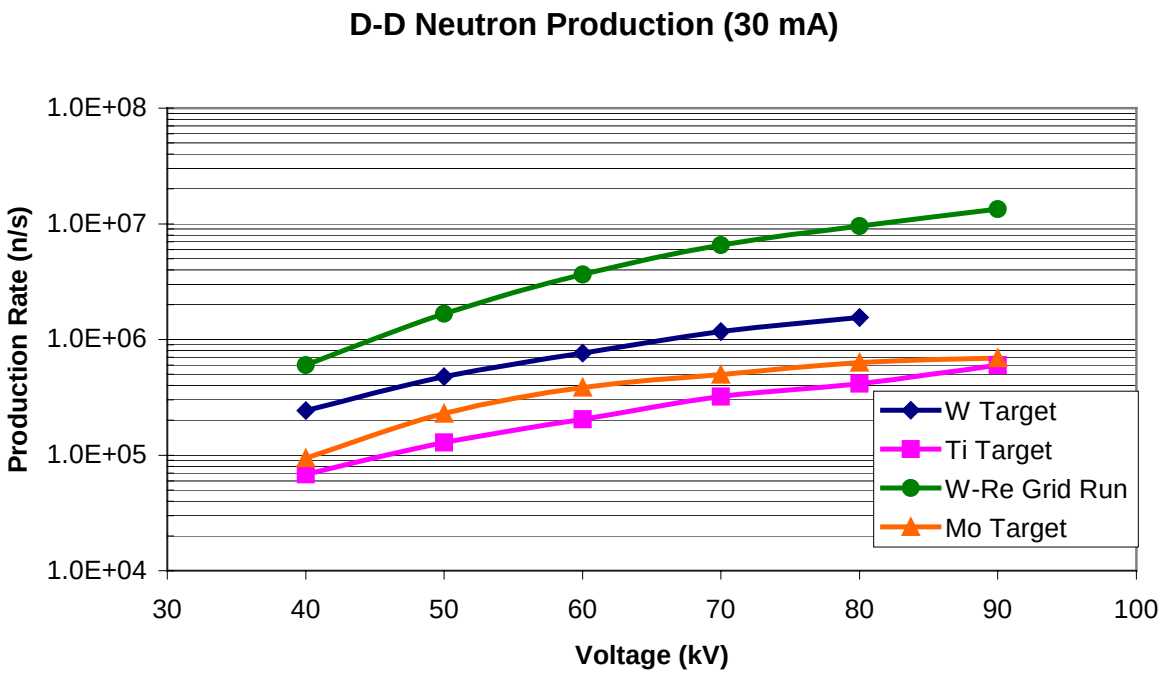

Figure 6-7: Solid Cathode Embedded Reaction Rates

The rates did not change with time, so the result is an indication of the fully-embedded condition. The tungsten target showed the highest D-D reaction rates, followed by the molybdenum cathode. The titanium target produced the lowest number of neutrons. This figure includes data from normal operation with a W-Re grid operated at the same conditions. It is interesting that the W-Re grid only out-performed the tungsten target by a factor of 3 at 40 kV and by a factor of 10 at 80 kV.

The difference between the different targets is probably explained by the difference in diffusivities of deuterium in different metals (see Part III, Chapter 12). Tungsten has a very low diffusivity of hydrogen isotopes, the lowest of any metal. Titanium has a much higher diffusivity, especially at high temperatures. Molybdenum is somewhere in between. At the high temperatures at which the targets operate, the deuterium probably implants and diffuses out much more quickly in the titanium, so it does not have a chance to build up to a high density. The deuterium moves slower in the molybdenum and especially the tungsten, so the number density can build up more. The buildup difference may also be due to differences in solubility and trapping locations in the different metals.

One discrepancy that has not yet been solved with these experiments is that the D-D neutron and proton production rates were not the same in the solid targets. (This has also been a problem with normal grid runs). Figure 6-8 shows the discrepancy between the rates.

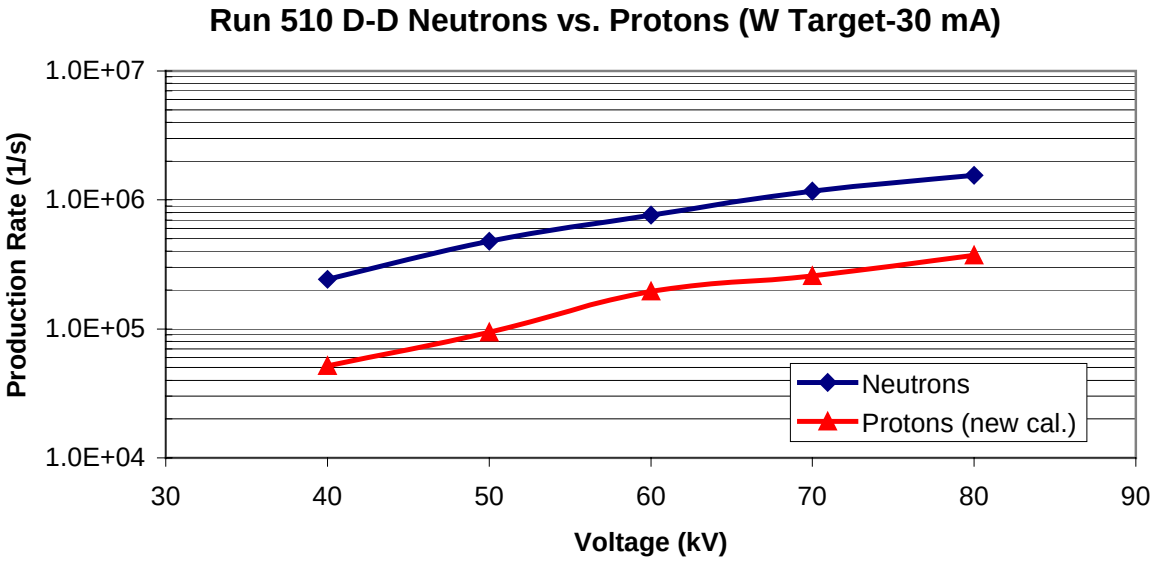

Figure 6-8: Neutron-Proton Discrepancy with the Solid Tungsten Cathode

Clearly, there is some problem with the calibration factors to make the neutron rate consistently a factor of 4 higher than the proton rate. One possibility is that some of the ions fuse as they accelerate towards the target, resulting in some reactions taking place in the volume source. Some of these reactions would remain outside of the field of view of the proton detector but would still be registered by the neutron detector. Another possibility is that the neutron calibration is wrong. A Pu-Be source is used for the neutron calibration, but this source has a distribution of energies up to 10 MeV. The D-D neutrons all come out with 2.5 MeV. Even though the neutrons are thermalized before counting, the energy difference may affect the counting efficiency.

The D-^{3}He experiments with the solid targets were of more interest. To reiterate, the experiments were designed to determine the differences between D on ^{3}He and ^{3}He on D reaction rates. Figure 6-9 shows the results from the tungsten target. The bottom curve shows the D-^{3}He rates with helium only in the chamber after previous deuterium implantation, so the protons only come from ^{3}He on embedded D reactions. The square data points show the rates with D on embedded ^{3}He. The circle data points show the results of running both gases at the same time. Finally, the triangle data points show an example of the rates from a record W-Re grid run at similar conditions.

The proton production from D on ^{3}He is about an order or magnitude higher than from the ^{3}He on D. This corresponds to previous results that suggested the deuterium density in the grid does not build up as high as the helium density. Running both gases at the same time produced the best result with a solid target. It is also striking that the target D-^{3}He rate was very close to the record W-Re grid rate, which again shows how much the embedded regime dominates the reaction rate.

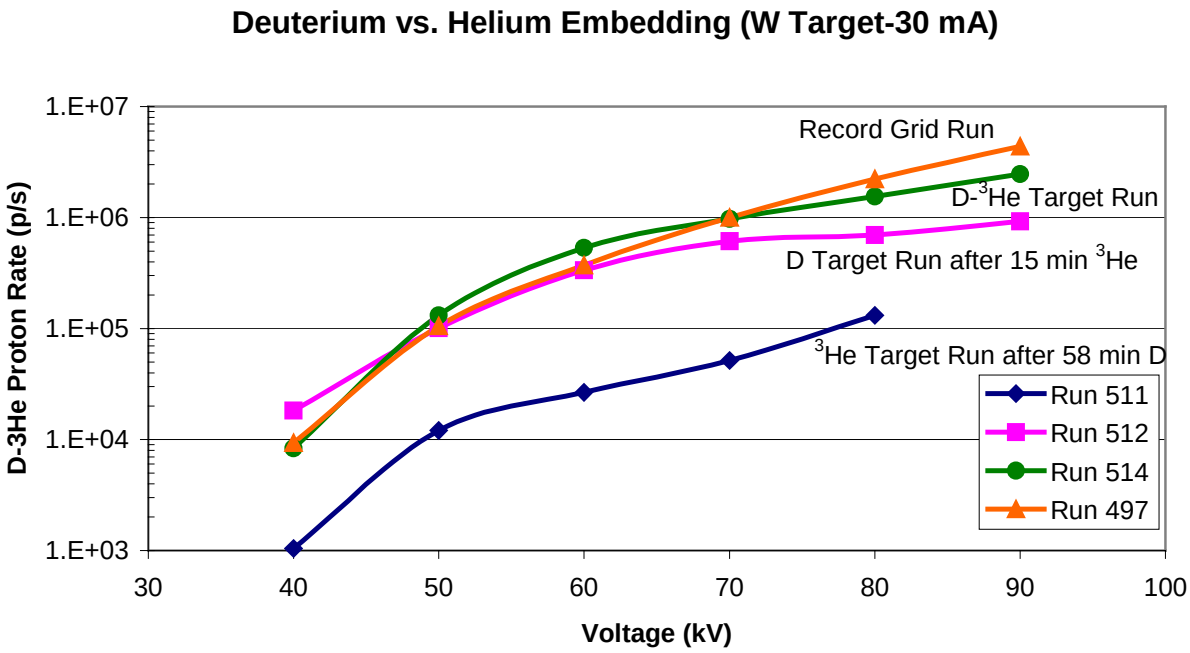

Figure 6-9: D-^{3}He Rates on the Solid Tungsten Cathode

The other targets performed similarly to the tungsten. The molybdenum target, run with the same sequence of experiments, showed the same progression in rates confirming the results from the tungsten. The total D-^{3}He rates were slightly lower for molybdenum, though. The titanium also showed similar results, except the D-^{3}He rates were much lower in comparison. There was more variation in the rates because of poor counting statistics for the low count rates. Figure 6-10 shows a comparison of the D-^{3}He rate for all three targets. All experiments were carried out with the same deuterium to helium ratio of 1 using the residual gas analyzer.

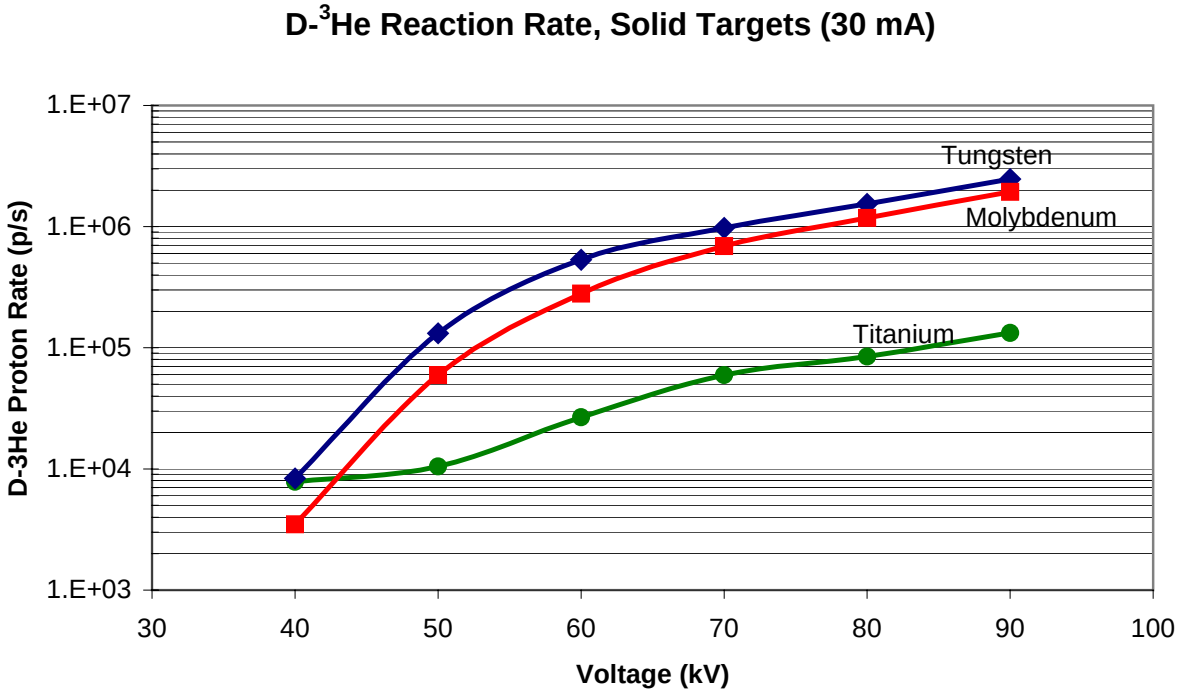

Figure 6-10: D-^{3}He Rates in Different Solid Cathodes

The rates are highest in the tungsten, but molybdenum is not too far behind. The titanium target's D-^{3}He reaction rates were over an order of magnitude lower. The bend in the graph of the titanium rates on the left is due to poor counting statistics. It is interesting that the D-^{3}He rates in Figure 6-10 follow the same trend in the different materials as the D-D rates in Figure 6-7. The result suggests that there is some relationship between deuterium diffusion and helium diffusion within the metals.

6.2 Eclipse Experimental Results

The eclipse experiments at first gave results with a large amount of variation between repeated experiments. It was eventually found that the eclipses needed to be lined up more carefully. The large eclipse was designed to completely block out the

inner grid, but in some of the initial runs portions of the grid were visible to portions of the proton detector surface. Once these problems were ironed out, the eclipse experiments gave repeatable results. All experiments were run at a constant 30 mA grid current and around 1.8 mtorr background gas pressure.

For D-D reactions, the large eclipse blocked 90-95% of the D-D protons over the 40-100 kV range. The small eclipse blocked from 60-69% of the D-D protons, and the medium eclipse blocked 72-90% of the D-D protons. The ranges in the results were due to differences in alignment of the eclipses. The medium eclipse gave the most varying results over different experiments. It is worth pointing out that these percentages did not change with voltage over the 40-100 kV range.

The D-^{3}He results were much different. The small eclipse blocked 4-10% of the D-^{3}He protons, and the medium eclipse blocked 41-47% of the D-^{3}He protons. With the large eclipse in place, no D-^{3}He proton peak was visible above the noise in the spectrum. In other words the large eclipse blocked very close to 100% of the protons. Figure 6-11 summarizes the results of the eclipse experiments.

The small eclipse blocked out a large fraction of the D-D protons, but not many of the D-^{3}He protons. This result suggests a large core regime for D-D at these conditions, but a smaller core contribution for D-^{3}He. Likewise, the medium eclipse blocked more of the D-D protons as compared to the blockage of D-^{3}He protons. The large eclipse blocked out both the core and embedded regimes, so the eclipse experiments show that the D-^{3}He reaction has very few reactions outside of these regions. (This is consistent with the embedded experiments that show a dominant embedded source). On the other hand, there are still some D-D protons coming from the volume source.

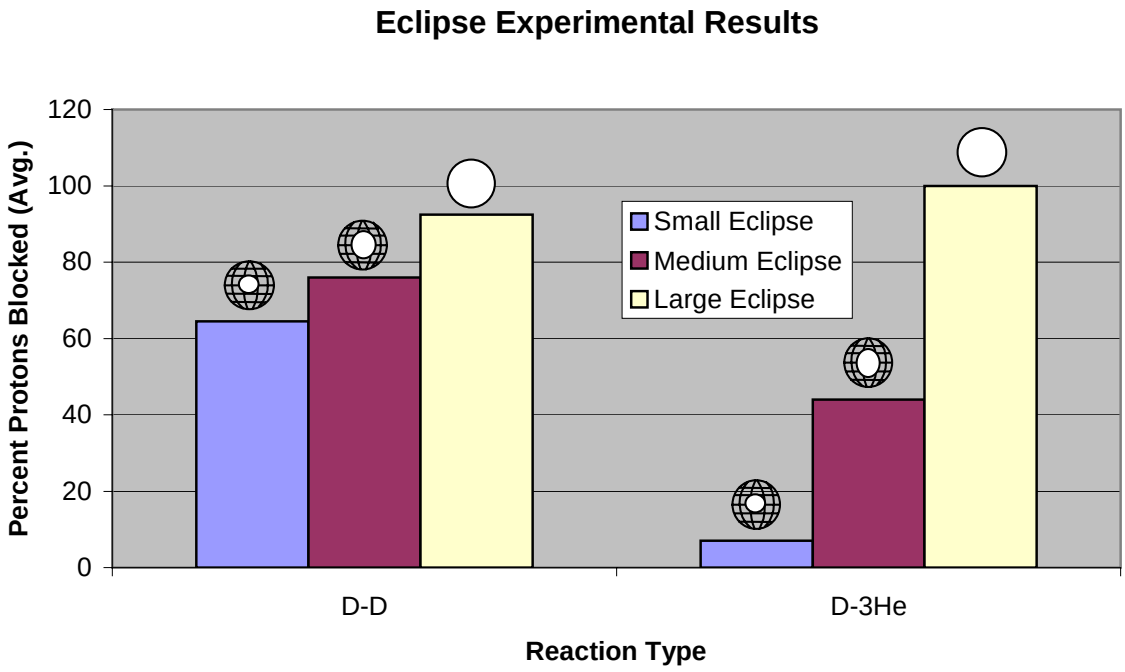

Figure 6-11: D-D and D-^{3}He Protons Blocked by the Eclipse Experiments

6.3 Off-Axis Experimental Results

For the off-axis experiments, both the off-axis and on-axis protons detectors were run at the same time. This setup eliminated some uncertainties from experiment to experiment. The current was kept constant at 30 mA with a pressure around 1.8 mtorr. The ratio of the raw counting rates from the two detectors stayed about constant over the voltage scans.

Using the volumetric calibration factor for the off-axis detector, an estimate for the volumetric reaction rate was determined. The result is shown plotted in Figure 6-12. The top most line shows the reaction rate using the on-axis detector with the original volume source calibration factor. The bottom line shows the volume source rate using

the off-axis numbers with the volume source calibration. The bottom numbers are actually an average over all of the off-axis experiments. The almost order of magnitude

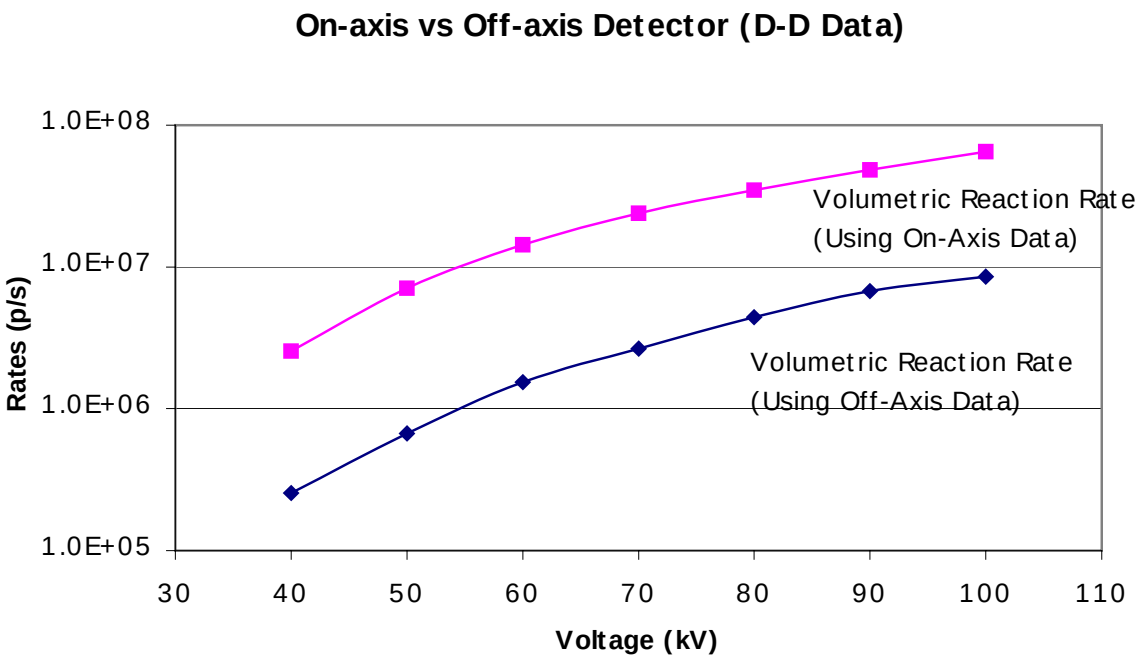

Figure 6-12: D-D Off-Axis Detector Evidence of Volume Source Discrepancy

difference suggests that there is a problem with using the volume source assumption for the on-axis calibration factor. On average, the volume source rate from the off-axis detector is about 12% of the on-axis rate using the old calibration factor. This means that about 12% of the on-axis raw counts come from the volume regime.

The off-axis data for D-^{3}He protons was much different. Very few counts for the D-^{3}He proton peak showed up in the off-axis detector. The counting rates were so small compared to the on-axis detector that the volume source regime was found to be negligible (<1% of the total rate) for D-^{3}He. In other words almost all of the counts seen on the on-axis proton detector originate from the center of the device. Figure 6-13 shows that the D-^{3}He volume source rate from the off-axis detector is about three orders of

magnitude lower than the volume source assumption using the on-axis numbers. The variation in the lower voltages was due to low counting rates in the off-axis numbers.

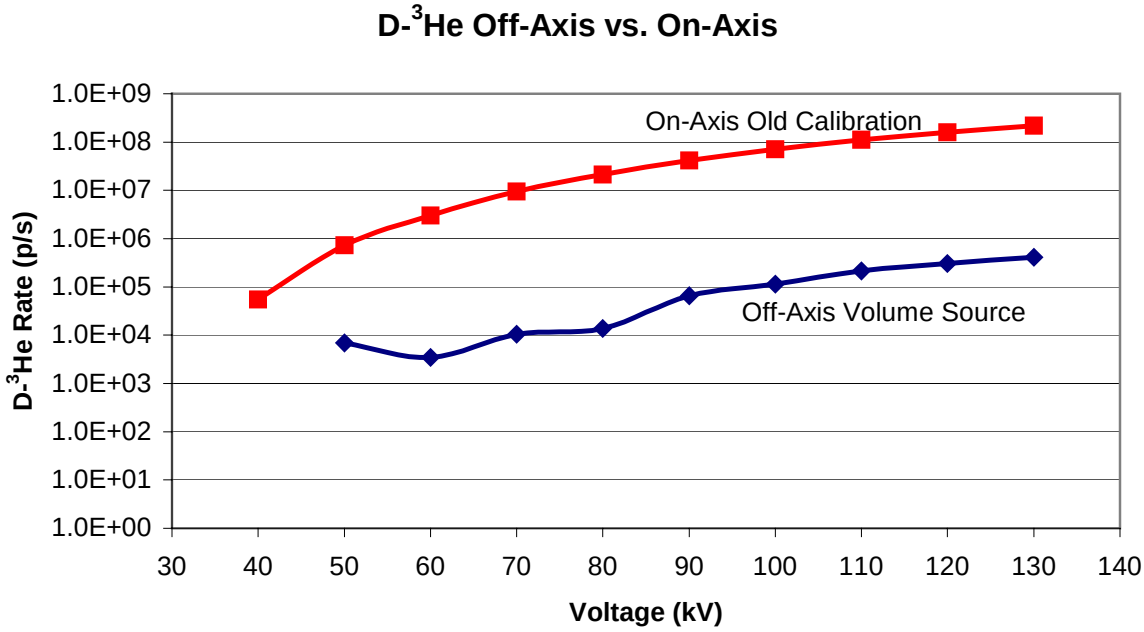

Figure 6-13: D-^{3}He Off-Axis Detector Evidence of Volume Source Discrepancy

The averaged data from these experiments was used to determine the break-down between the source regimes. Assuming the volumetric reaction rate from the off-axis detector is correct, this rate was used to determine what fraction of the on-axis counts was due to volume reactions, and the rest were due to core or embedded reactions. Approximately 10% of the on-axis raw D-D proton counts are due to volume source reactions. However, because the calibration between a point source and volume source are so different, the volume source can still lead to a large percentage of the total reaction rate. Likewise, a negligible portion of the on-axis D-^{3}He protons are due to the volume source.

Chapter 7 Source Regime Discussion

7.1 Source Regime Breakdown

For the D-D reaction, the embedding experiments showed that about 14% of the protons detected on-axis came from the embedded regime. The off-axis experiments found that 12% of the on-axis counts came from the volume regime, so this leaves 74% of the raw counts originating in the core. In the eclipse experiment, the small disc blocked 60-69% while the medium eclipse blocked 72-90% of the D-D protons. This correlates reasonably well to 74% of the counts coming from the core. The large eclipse blocked 90-95% of the D-D protons. The large eclipse blocks the entire core and embedded regime plus part of the volume regime, so this result was a further verification of the other experiments.

Table 7-1 summarizes the results for D-D fusion runs. The top row shows the average percentage of the raw counts reaching the detector from each regime. Since each regime has its own calibration factor, the bottom row shows the contribution of each regime to the total reaction rate in the chamber. The calibration factor calculations are included in Appendix A. The converged core, embedded, and volume calibration factors are 8260, 15700, and 164850 respectively. These are the total number of protons generated for each proton detected from each regime.

	Converged Core	Embedded	Volume
Raw Counts	74%	14%	12%
Total Rate	22%	8%	70%

Table 7-1: D-D Source Regime Breakdown

The embedding experiments with D-^{3}He showed that about 90% of the counts reaching the proton detector were due to embedded reactions. The off-axis experiments showed a negligible contribution from the volume regime. The other 10% then must be from the converged core regime. The small eclipse blocked from 4-10% of the D-^{3}He protons, which seems to verify the core regime. The medium eclipse blocked 41-47% of the protons, but this eclipse also covered more of the grid wires. The large eclipse blocked all of the D-^{3}He protons, verifying a negligible volume regime. Table 7-2 summarizes the results. All of these percentages in Tables 7-1 and 7-2 apply over the voltage range from about 40-100 kV and pressures around 2 mtorr. The percentages would most likely change with different pressures.

	Converged Core	Embedded	Volume
Raw Counts	10%	90%	Negligible
Total Rate	5%	95%	Negligible

Table 7-2: D-^{3}He Source Regime Breakdown

The D-D results were not much different than expected. The volume source was believed to dominate, and that is still the case. There is a sizeable core regime though. The small embedded regime is probably explained by the increased diffusivity of hydrogen isotopes in metals.

The difference in the volume source reactions between D-D and D-^{3}He fuels is more difficult to explain. It most likely is due to differences in the fusion cross-sections over the 40-100 kV energy range (see Figure 2-3). The D-D cross-section increases gradually from 40-100 kV. The D-^{3}He cross-section increases much more rapidly up to 100 kV. The volume source is mainly due to charge exchange reactions occurring when

the ions travel in or out of the center of the device. The fast neutrals generated then will be at a lower energy than the cathode voltage depending on where in the potential well the exchange takes place. At 100 kV for example, the average fast neutral may have ~50 keV of energy. For the D-D reactions, the cross-section is not much different between 50 and 100 keV, so the volume source can contribute. For D-^{3}He though, the difference between 50 and 100 keV is much more significant, so the number of D-^{3}He reactions at 50 keV will be considerable less. Therefore, the volume source is negligible compared to the core and embedded reactions that occur at or near full cathode voltage.

7.2 Proton Detector Calibration

The varying source regimes result in drastically modified proton detector calibration factors. Also, the factor is different for the D-D and D-^{3}He reactions. At different run conditions (such as lower pressure or higher voltages), the calibration factors will need to be recalculated.

The total calibration factor for D-D fusion in the IEC device is (using the individual calibration factors and Table 7-1):

$$8{,}260(0.74)+15{,}700(0.14)+164{,}850(0.12) = \mathbf{\underline{28{,}090}}$$

It should be noted that the top row percentages from the table were used since this number converts raw counts (in counts/sec) to total proton production rate. The total calibration for D-^{3}He (using Table 7-2) is:

$$8{,}260(0.10)+15{,}700(0.90) = \mathbf{\underline{15{,}000}}$$

7.3 Implications for Isotope Production

The very large fraction of D-^{3}He reactions occurring in the embedded regime was an unexpected result of this research. It means that at the conditions of operation, the IEC device is acting essentially as an accelerator for D-^{3}He reactions. Beam-target reactions dominate the rate. In the future, the IEC project plans to move to a low-pressure regime, which should increase the converged core reactions. Until such a change is made, embedded reactions dominate in the current experimental conditions.

Because of the dominance of embedded reactions, it is logical to use the embedded reactions for isotope production. All of the designs to produce isotopes using D-^{3}He reactions that will be described in the following sections use embedded fusion. The designs consist of replacing the inner grid with a solid, non-transparent cathode (like the target experiments) to force only embedded reactions. These solid cathodes were then designed to house the material for activation, and thus produce isotopes.

Part II: Medical Isotope Production

Chapter 8 Medical Isotope Production Theory

With the D-^{3}He source regime established, it was possible to begin the work on producing isotopes. The first step was to choose which isotopes to try to make. The operational characteristics of the IEC project make it particularly well suited to the production of short-lived species. The isotopes used in Positron Emission Tomography fall into the category of short-lived species, and they formed the focus of where the research began.

8.1 Positron Emission Tomography

Positron Emission Tomography (PET) is a medical imaging procedure started during the second half of the last century [1]. Tomographic images are two-dimensional "slices" of parts of the body. PET is unique from other imaging procedures like MRI (Magnetic Resonance Imaging) and X-ray CT (Computer Tomography) in that it can provide real-time images of a physiologic process. A positron emitter is attached to a biological tracer and injected or ingested into a patient. The tracer then travels to the location of interest. When the isotope decays, the positron almost immediately annihilates with an electron to produce two 511 keV gamma rays traveling in opposite directions. Detectors around the patient then detect the gamma rays, and through coincidence counting and geometry considerations are able to determine where they originated. In this manner, the tracer is followed in real time through uptake and removal from areas of interest.

This information is reconstructed into an image of the desired area. The rate of the absorption or diffusion of the tracer tells whether the tissue is healthy or unhealthy. PET can be used to track blood flow in the heart, track sugar consumption in areas of the brain, or determine the location of cancerous tumors. Modern PET scans have image resolutions of a few mm. The demand for PET isotopes has grown considerably in the past decade due to increasing insurance coverage of the procedures [2].

Table 8-1 lists a few isotopes that can be used in PET. All of these positron emitters can easily be attached to a variety of biological tracers, and they are all created with high-energy protons. The isotope ^{18}F, with its 110-minute half-life, is commonly used today. It can be attached to dopamine to do brain activity scans. It is also often attached to FDG (Flurodeoxyglucose), a sugar compound, to measure sugar uptake in all areas of the body. The imaging of sugar uptake can show the location of cancerous regions which consume sugar at a much higher rate than healthy tissue.

PET Isotope	Production	Half-life (min)
^{18}F	$^{18}O(p,n)^{18}F$	110
^{15}O	$^{15}N(p,n)^{15}O$	2
^{13}N	$^{16}O(p,\alpha)^{13}N$	10
	$^{13}C(p,n)^{13}N$	
^{11}C	$^{14}N(p,\alpha)^{11}C$	20
^{94m}Tc	$^{94}Mo(p,n)^{94m}Tc$	52

Table 8-1: PET Isotopes [3]

Figure 8-1 shows how PET is used to scan for cancerous tumors. The ^{18}F-labeled FDG is injected into a patient. FDG is rapidly absorbed into the brain tissue during

normal activity. The picture on the left shows a normal, healthy brain. The picture on the right shows a patient with a brain tumor. Cancerous cells absorb much more FDG since they are growing at a faster rate. The tumor shows up brighter than other areas since more of the isotope is drawn into those cells.

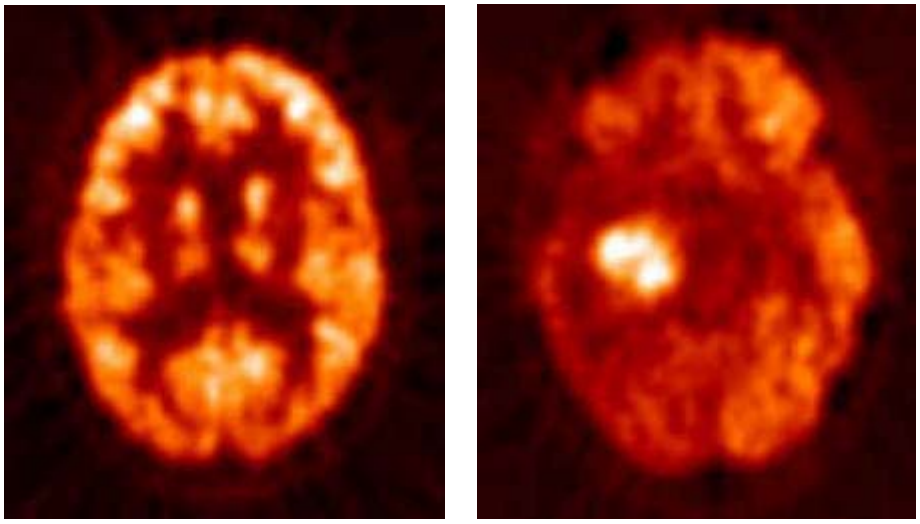

Figure 8-1: PET Brain Scan Showing Cancerous Region Using ^{18}F [4]

The isotopes ^{15}O with its 2-minute half-life, ^{13}N with its 10-minute half-life, and ^{11}C with its 20-minute half-life are desirable for medical imaging because they give the patient a much lower residual radiation dose after the scan is completed. This lower dose would be particularly advantageous for the diagnosis of pregnant women and children [5]. These three isotopes can all be easily incorporated into a variety of biological compounds.

Figure 8-2 shows the physiological function of PET with a ^{13}N-labeled ammonia scan. In this diagnostic, the tracer is injected into the blood and can be used to show blood flow to the myocardium (heart muscle). The picture on the left shows a cross-section of a healthy heart muscle—the ring indicates that all areas were receiving blood

flow. The picture on the right is the same cross-section of a patient who suffered a heart attack. The dark areas on opposite sides show areas that were not receiving blood.

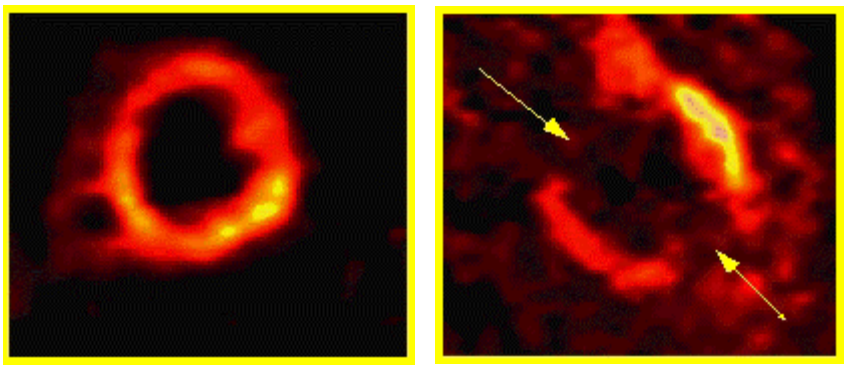

Figure 8-2: PET Myocardium Scan Using ^{13}N [6]

The last isotope listed in Table 8-1 is ^{94m}Tc, a technetium isotope with a 52-minute half-life. This isotope has been used in limited cases [7], and has the advantage of being able to be used with the same chemistry associated with ^{99m}Tc (a well established and highly used gamma emitter in nuclear medicine). Unfortunately ^{94m}Tc gives off a number of high-energy gamma rays and so results in a higher residual radiation dose to the patient than desired.

The isotope ^{94m}Tc was produced in this project as a first step in developing the process. Although it is not desirable for PET imaging, it provided a relatively easy way to do proof-of-principle production. The following step in this research was the production of ^{13}N. It was created by using high-energy protons on ^{16}O which allowed water to be used as a target.

8.2 Present Sources of Radioisotopes

Most of the isotopes used today for nuclear medicine come either from nuclear reactors, cyclotrons, or linacs. Nuclear reactors are able to create some desirable isotopes as by-products of the fission reaction. One example is ^{99}Mo which then decays into ^{99m}Tc. Generators are made using ^{99}Mo to provide ^{99m}Tc far away from the reactor [1]. Reactors are also able to create isotopes from neutron activation. The large neutron flux in a reactor allows it to create a large amount of isotopes in a short time period.

Cyclotrons and linacs are used to accelerate charged particles into targets for isotope production. Most commonly hydrogen and deuterium are accelerated from 10 to 20 MeV at which point the cross-sections for (p,x) or (d,x) reactions tend to be high enough to produce quantities in the 50 to 100 mCi range [1]. Cyclotrons in particular are used often sometimes strictly for the purpose of producing medical isotopes. They have been good for PET production because cyclotron technology is very mature.

The first isotope used in this work was ^{94m}Tc, made from the ^{94}Mo(p,n)^{94m}Tc reaction. ^{94}Mo is a stable, naturally-occurring isotope that makes up about 10% of natural molybdenum. The cross-section plot for ^{94m}Tc production is shown in Figure 8-3. The cross-section has a threshold around 6 MeV, and is fairly large over the range from 6 to 15 MeV. The 14.7 MeV D-^{3}He protons have a large area under the cross-section plot to work with.

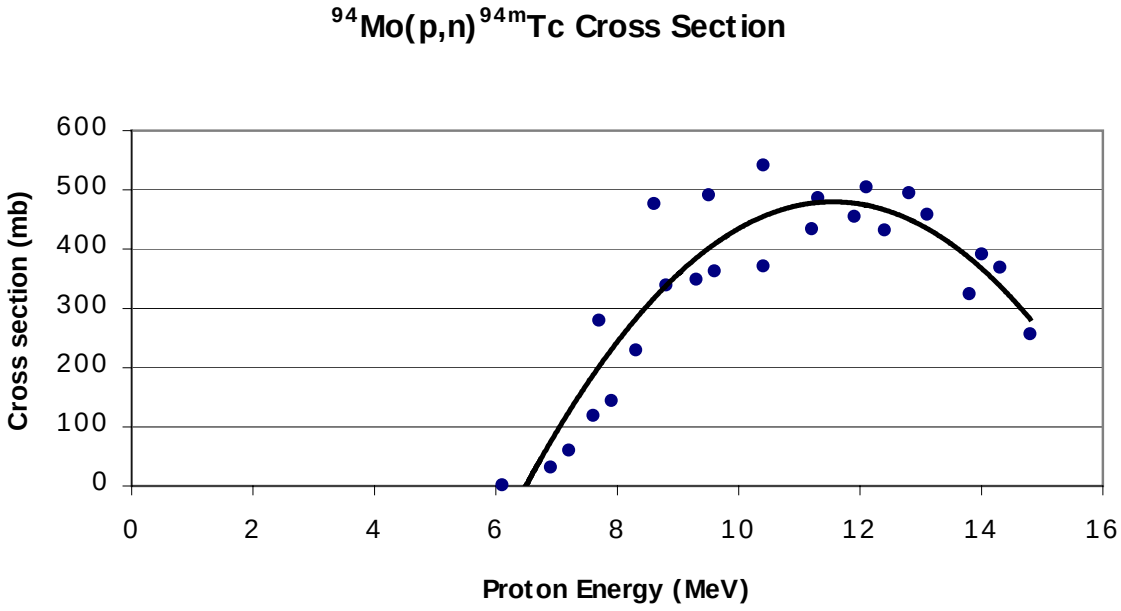

Figure 8-3: Cross-section for ^{94m}Tc Production [8]

The isotope ^{13}N was also created in this research from the ^{16}O(p,α)^{13}N reaction. Figure 8-4 shows the cross-section for this reaction. Although the cross-section is not as high as for the ^{94m}Tc production, the D-^{3}He protons do still have a significant probability to react down to about 6 MeV. The advantage of the reaction is that a proton beam can simply bombard a water target to transform the oxygen in the water. A small amount of alcohol added to the water will induce the formation of $^{13}NH_3^+$ ions in the water [9]. These ammonia ions are easily separated out from the rest of the water using an ion exchange resin. The typical ^{13}N dose needed for a PET scan is about 20 mCi, but often about 100 mCi must be produced since about ¾ will decay away by the time it reaches the patient [10].

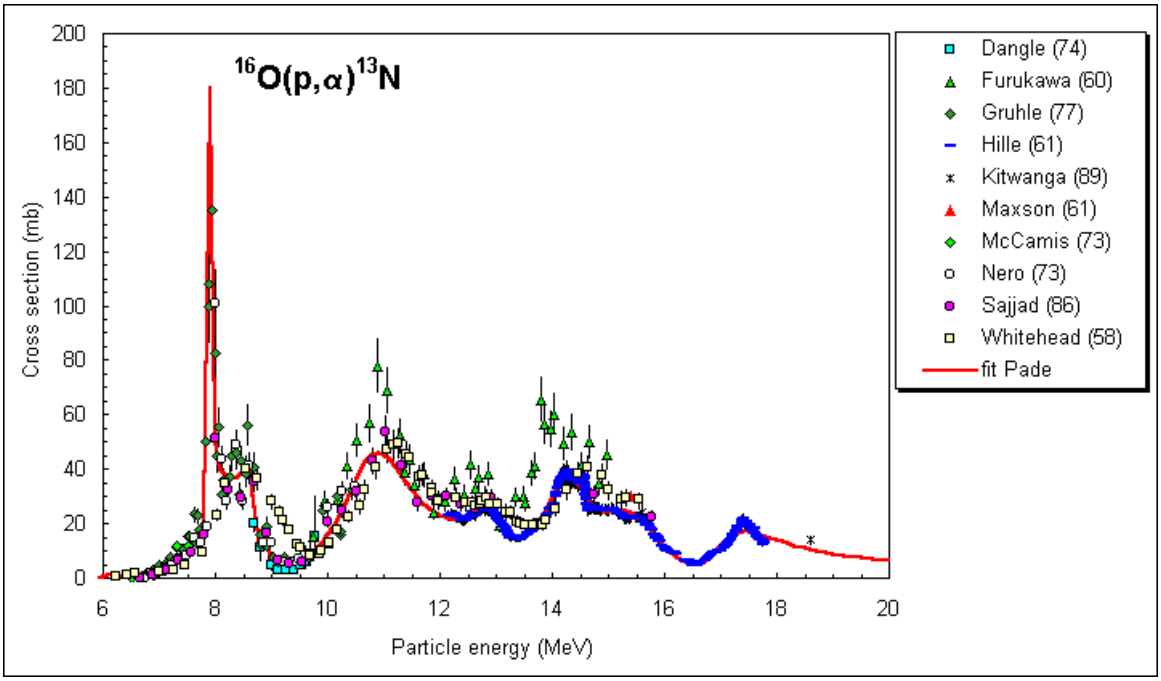

Figure 8-4: Cross-section for ^{13}N Production [11]

8.3 Theory of Thick Target Yield

In the isotope production experiments using the IEC device, the 14.7 MeV D-^{3}He protons bombard a thick target. In other words the target is thick enough to slow down and completely stop the high-energy protons. The thick target case is complicated by the fact that the proton energy decreases with the depth the proton has traveled in the material. The cross-section for isotope production then is a function of depth.

The equation for calculating the yield of a beam on a thick target is [1]:

$$A = (1 - e^{-\lambda t}) n_{par} \int_0^{R_p} \sigma_i(x)\phi(x)dx \qquad \text{Eq. 8-1}$$

where A is the total activity produced (decays/s), λ is the decay constant of the produced isotope (s^{-1}), and t is the time of the run (s). The variable n_{par} is the number density of the

parent atom (cm^{-3}). The cross-section, σ_i (cm^2) is a function of x (cm), because the proton energy is a function of x. Finally, ϕ is the total number of protons hitting the target in s^{-1}. The integral is evaluated from 0 at the target surface to R_p, the penetration depth of the proton.

For rather small cross-sections, which tend to be the case for (p,x) reactions, the flux of incoming protons does not change to a significant amount during the bombardment. Therefore, ϕ is a constant that can be removed from the integral. The integral can further be changed into the variable energy. The stopping powers of materials are well-known data sets and given as [1]

$$S(E) = \left|\frac{dE}{dx}\right| \qquad \text{Eq. 8-2}$$

Stopping powers are simply the change in energy per unit distance traveled, and this varies with the energy. Equation 8-2 can then be substituted into Equation 8-1 to give [1]

$$A = (1 - e^{-\lambda t}) n_{par} \phi \int_0^{E_p} \frac{\sigma_i(E)}{S(E)} dE \qquad \text{Eq. 8-3}$$

Given a constant proton flux and the run time, the cross section and stopping power tables can be used to solve for the theoretical activity produced.

An alternative to the integrated approach is to solve for the activity using a spreadsheet in a numerical method. For the numerical method, a distance step is used over which the production is solved for given the number density, flux, and proton energy. Then, the stopping powers are used to recalculate the proton energy for the next step. Both methods result in the same results if the distance step used is small enough.

The complication with the current IEC device was that often it was not possible to maintain a constant D-^{3}He reaction rate during the run. This may have been due to variation in the voltage (±2 kV) and variation in the current (±1 mA) during runs. For these cases, it was important to record the proton production rate (the flux) as a function of time. The flux was then approximated as a series of constant flux levels for short time, and Equation 8-3 was used to solve for each flux level. Then, taking into account the decay until the end of the experiment, the numbers were added to find the final activity.

It is typical in the radioisotope production community to measure the production in the units mCi/μA. This unit refers to the maximum activity produced assuming an infinite radiation time at 1 μA of proton current. This normalized unit is found by converting ϕ to I in Equation 8-3 and by removing the $(1-e^{-\lambda t})$ term:

$$A = 1.689 \times 10^5 n_{par} I \int_0^{E_p} \frac{\sigma_i(E)}{S(E)} dE \qquad \text{Eq. 8-4}$$

In this equation, I is given in μA, and all other constants retain the same units.

Equation 8-4 can be further modified for the IEC case. The current given in Equation 8-4 refers to the proton current, and this is directly related to the D-^{3}He reaction rate. The D-^{3}He reaction rate is found from cross-section data as a function of the ion energies (or voltages). For beam-target reactions, the integral in Equation 8-4 is constant for a particular target material. The number density, n_{par}, is approximated as constant which allows the production yield to be given as a function of voltage. This will be described in more detail in Chapter 11.

8.4 References

[1] J.A. Sorenson & M.E. Phelps (1987). *Physics in Nuclear Medicine, Second Edition* New York: W.B. Saunders Company.

[2] E. Adams & K. Flynn, "A Systematic Review Update of FDG-PET as a Diagnostic Test in Cancer and Alzheimer's Disease," Health Services Research and Development Services Technology Assessment Report, MTA 98-032 (September, 1998), see also www1.va.gov/resdev/prt/petreport.htm.

[3] R.B. Firestone (1996). *Table of Isotopes: 8th Edition,* New York: John Wiley.

[4] Cyclotron Research Group, University of Wisconsin-Madison, www.medsch.wisc.edu/cycl/default.html (2004).

[5] G.L. Kulcinski, "Near Term Commercial Opportunities from Long Range Fusion Research," *Fusion Technology,* **30**, 411 (1996).

[6] Biomedical Research Foundation of Northwest Louisiana, www.biomed.org/pet.html (2004).

[7] B.T. Christian, R.J. Nickles, C.K. Stone, T.L. Mulnix & J. Clark, "Improving the Radionuclidic Purity of ^{94m}Tc for PET Imaging," *Applied Radiation & Isotopes,* **46(2)**, 69 (1995).

[8] National Nuclear Data Center (EXFOR[CSISRS]), www.nndc.bnl.gov/nndc/exfor (2003).

[9] J.W. Weidner, "The Production of ^{13}N from Inertial Electrostatic Confinement Fusion," Master's Thesis, University of Wisconsin-Madison (2003).

[10] N. Tamaki et al., “Dynamic Positron Computer Tomography of the Heart with a High Sensitivity Positron Camera and Nitrogen-13 Ammonia,” *Journal of Nuclear Medicine*, **26**, 567 (1985).

[11] Nuclear Data Services, International Atomic Energy Agency, www-nds.iaea.or.at/medical/O6p13N0.html (2003).

Chapter 9 Medical Isotope Production Experimentation

Three different experiments were setup to produce isotopes from embedded D-^{3}He reactions. In all three cases, the IEC grid was replaced with a solid cathode that forced only embedded reactions to occur. The high voltage was applied directly to the target to pull the fusion ions into it.

9.1 Solid Molybdenum Target

The first idea was designed to produce ^{94m}Tc using a molybdenum cathode. A solid sphere of molybdenum was fabricated with a protrusion at the top to connect to the high-voltage stalk. Figure 9-1 is a schematic of the general idea. With a negative potential applied to the molybdenum target, both the deuterium and helium-3 ions were pulled into the outer layer. At the voltage range used in this experiment, the ions were

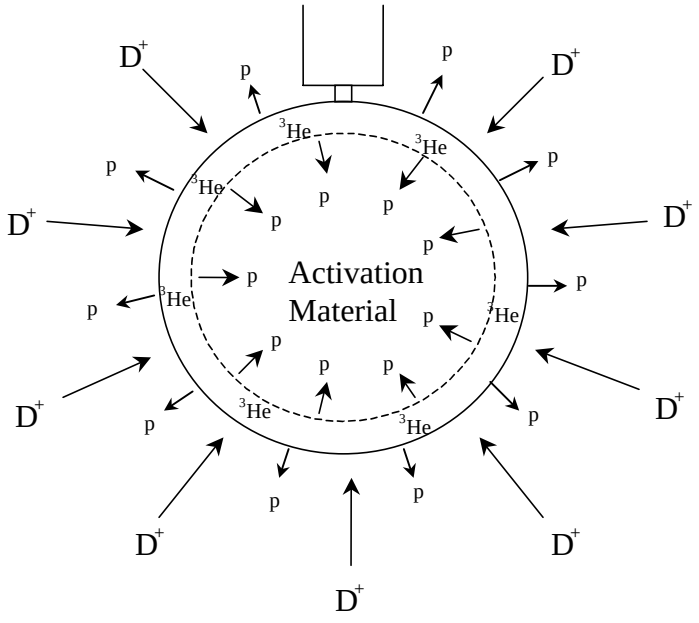

Figure 9-1: Method for Beam-Target Isotope Production

implanted within about a micron of the surface of the target. Further bombardment initiated D-^{3}He fusion reactions in the outer layers of the target. The 14.7 MeV protons generated from the reaction are created isotropically, so roughly half traveled deeper into the target.

Natural molybdenum is composed of about 10% ^{94}Mo which can be used to produce ^{94m}Tc from a (p,n) reaction. The ^{94m}Tc isotope decays by positron emission 82% of the time, and decays with a 52-minute half-life. The production cross-section for this isotope and short half-life overshadows the production of any other isotope that can be created from natural molybdenum.

The purpose of this first isotope experiment was to produce isotopes as easily as possible using the target concept. Molybdenum has a high melting point, so there was no need to actively cool the target from the high ion current hitting it. The target was installed in the chamber as shown in Figure 9-2A. Figure 9-2B shows the target during operation at 70 kV, 30 mA. The large power input caused the target temperature to reach ~1200 °C.

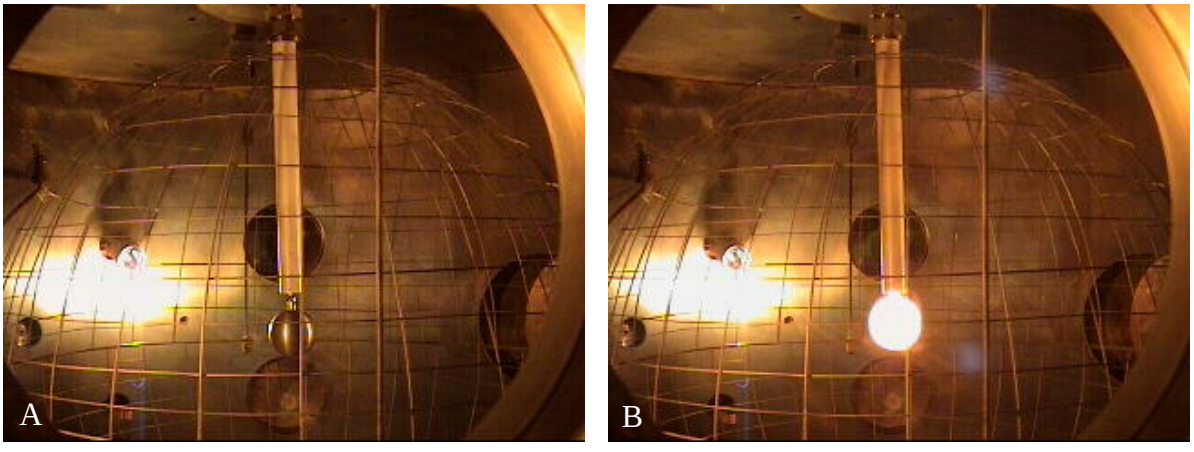

Figure 9-2: Molybdenum Target in IEC Chamber, (A) No Power, (B) 2.1 kW

After a production run, the molybdenum sample was removed from the chamber to be counted on a NaI scintillation detector. The detector had a flat, circular geometry, 7.6 cm in diameter. The molybdenum target was placed on the detector in the center for counting. As a positron emitter, the presence of ^{94m}Tc is indicated by a 511 keV gamma peak. In addition, each decay also releases an 871 keV gamma. The presence of an 871 keV peak along with a 511 keV peak with twice as many counts shows evidence for the production.

9.2 Al_2O_3 Target with Tungsten Coating

The next step in the production plan was to produce ^{13}N using the $^{16}O(p,\alpha)^{13}N$ reaction with a similar target setup. A solid aluminum oxide target was fabricated in the same configuration as the molybdenum target. The large fraction of oxygen in the target gave plenty of targets to create ^{13}N. A tungsten layer was then sprayed over the target to maintain the electrical contact and to hold the implanted ions. Both the target fabrication and layering process were sent out to private industries. The tungsten layer was put on with a thermal plasma spray process that sprayed small chucks of tungsten from a powder at elevated temperatures. A 25-50 μm layer was deposited. The final target is shown in Figure 9-3.

The idea of this design was to embed the fusion ions into the outer metal layer (100 keV D^+ only travels about 0.4 μm in tungsten [1]). Then the reactions occur at this point. The D-^{3}He protons then can travel into the target to activate the oxygen. In 50 μm of tungsten, the 14.7 MeV protons lose about 1.5 MeV of their energy [1], so they still

have plenty of energy upon reaching the oxygen. The newly created ^{13}N stays trapped within the target. After producing the isotopes, it is important to remove the target quickly for counting (due to the short half-life). Because ^{13}N is a positron emitter, the 511 keV gamma-ray is detected.

Figure 9-3: Al_2O_3 Target with Tungsten Coating

Tungsten was chosen as the layering material based on the results of the solid target embedding experiments. Tungsten performed the best with D-^{3}He rates compared to molybdenum and titanium, so it seemed like the better choice for trapping the fusion ions. Unfortunately tungsten is difficult to work with, and there was some concern as to how well the tungsten would adhere to the oxide target.

9.3 Cooled Water Target

The difficulty with the two previous ideas was that the vacuum chamber had to be vented to take the target out after activation. Although this was not a problem for measuring the activity, it is unpractical for an actual isotope production system. The ideal system for the production of medical isotopes should have the following characteristics:

1. The target should be robust enough to handle many runs.
2. The activated isotope should be able to be removed from the device quickly.
3. The target must be able to withstand the high power input.
4. The target must hold a large amount of D or ^{3}He or both.

These project goals are just a first step if this idea ever has commercial possibilities. A commercial system would need a target and stalk design with a long lifetime. There would need to be some way to flow the material for activation into and out of the device. The target and system must be able to withstand the heat or be actively cooled. Lastly, a large deuterium or helium-3 inventory in the target will maximize the reaction rates.

The final design for the production of PET isotopes comes out of an effort to satisfy the four goals. The design consists of bombarding a water target that flows in and out the chamber easily. The water is cooled in a heat exchanger outside of the system. A steel tube is used to keep the water contained within the vacuum environment as well as to be able to hold a large amount of fusion ions.

The overall design is shown in Figure 9-4. The IEC cathode is replaced with a thin-walled stainless steel tube. The wall is 125 μm thick—this amount of steel is thick enough to stop the deuterium and helium ions, but thin enough to allow the 14.7 MeV

protons to pass through without losing much energy. The protons loose 2.3 MeV before they reach the water in the tube. The tube contains water in a closed loop, and the water acts as both the material to be activated the coolant for the tube. The ^{13}N production occurs from the (p,α) reaction on the oxygen in the water. A small pump circulates the primary loop. The primary loop passes through a tube-in-tube heat exchanger where heat is transferred to a chilled water line.

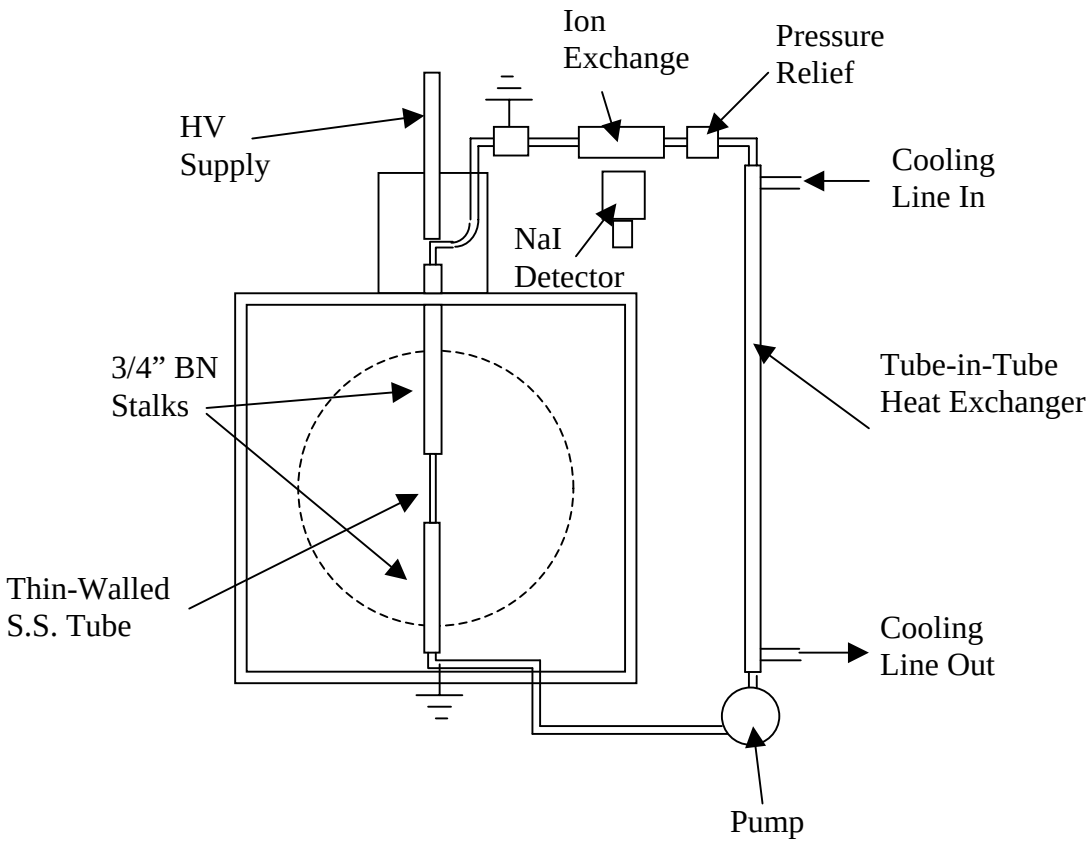

Figure 9-4: Cooled Water Target Design

Because high voltage is applied to the tube, the water used in the primary loop needs to be ultra pure and de-ionized to keep the resistivity high. The ion population

needs to be kept down to keep the water from drawing power. The creation of ^{13}N in the water from the oxygen creates NH_3^+, NH_2^-, or other ions with oxygen, and these must be removed. An ion exchange resin is used to accomplish both tasks. The resin is a mixed-bed resin designed for use with ultra-pure water; it removes both positive and negative ions. This resin keeps the water to a high resistivity, and collects all of the ^{13}N produced during the runs. A NaI detector is placed facing the resin to count the production rate.

Flowing water through a high voltage system poses an interesting challenge, but one that has been solved with other systems. It was important to design the entire primary loop out of materials other than brass or copper as they deposit ions into the water through corrosion. Stainless steel tubing and fittings were used for most of the loop. All tubing was 6.4 mm standard stainless steel tubing from the top of the oil-filled feedthrough clockwise around to the bottom of the lower stalk inside the chamber.

The lower stalk contains a ceramic tube. The ceramic tube connects to the thin-walled stainless steel tube (that makes up the cathode). This thin-walled tube travels the entire length of the upper stalk. At the top of the stalk (in the oil-filled feedthrough), a connection is made to plastic tubing that travels out of the oil. The plastic tubing on top and ceramic tubing on the bottom are used as insulators.

Figure 9-5 shows a picture of the inside of the IEC chamber with the initial design installed. Figure 9-5A shows the double stalk and steel tube design inside of the outer grid. Figure 9-5B shows the outside of the chamber. Figure 9-6 shows a close-up of the top of the IEC chamber. The oil-filled feedthrough is more clearly shown along with the resin exchange column. Below the column is the tube-in-tube heat exchanger.

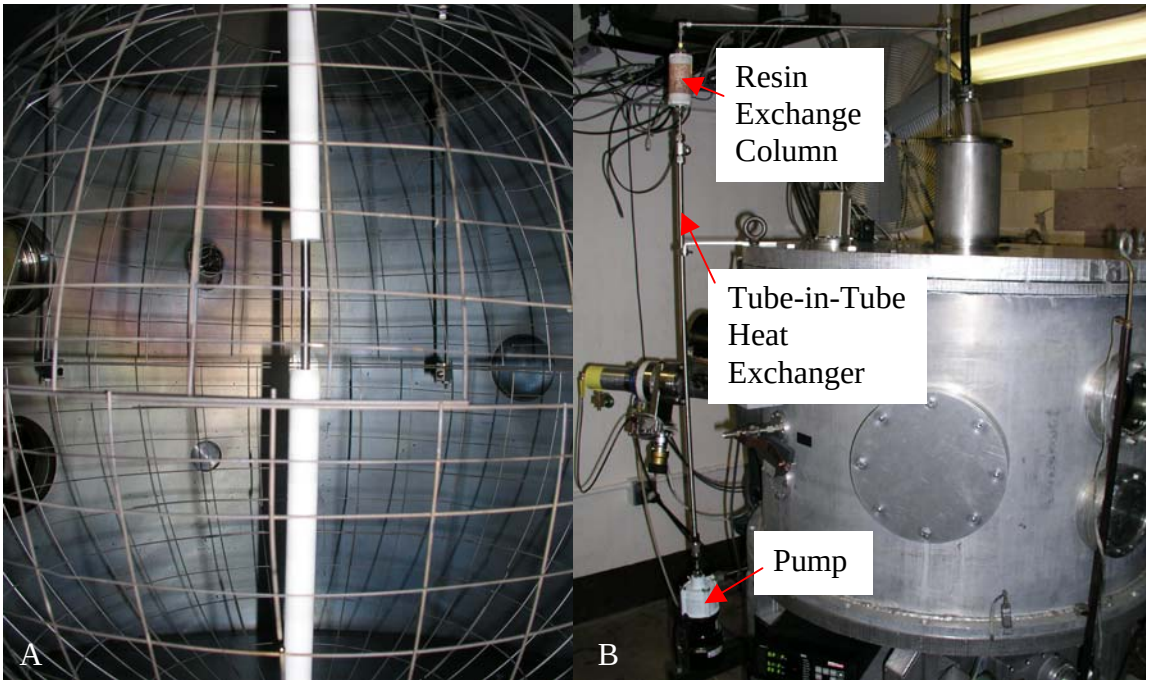

Figure 9-5: ^{13}N Production System, (A) Inside the Chamber, (B) Outside the Chamber

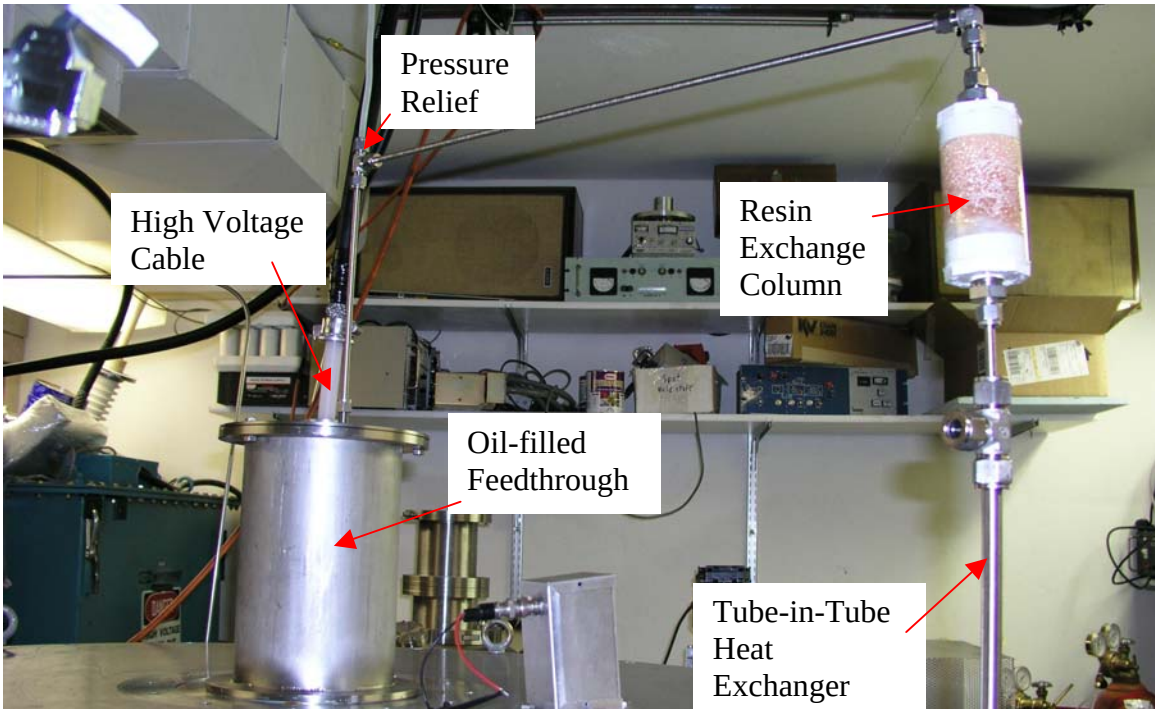

Figure 9-6: ^{13}N Production System, Top of IEC Chamber

Thermodynamic calculations were used to design the tube-in-tube heat exchanger and determine how much power could be removed. The pump moves water around the system at 0.25 L/min. With the chilled water line running at full capacity through the heat exchanger, this design easily allows for 1 kW power removal to keep the maximum primary loop water temperature below 75 °C.

The weakness in the design is in the lower stalk. The design described was the final version that gave the best results, but it went through many revisions. It was difficult to get a good connection from the thin-walled steel tube to the ceramic tube that would not leak in the vacuum environment, would not cause electrical breakdown, and would survive the plasma environment. During experimentation, this area was a constant source of problems.

9.4 References

[1] J.F. Ziegler & J.P. Biersack, “The Stopping and Range of Ions in Matter,” SRIM Code Version 2003.20 (2003).

Chapter 10 Medical Isotope Production Results

10.1 Molybdenum Target

10.1.1 Molybdenum Target Operation

When the molybdenum target was first installed in the chamber, it was attached to the high-voltage stalk as shown in Figure 10-1. A tungsten-rhenium wire loop was used to hang the target from the molybdenum rod in the stalk. This connection led to problems during runs.

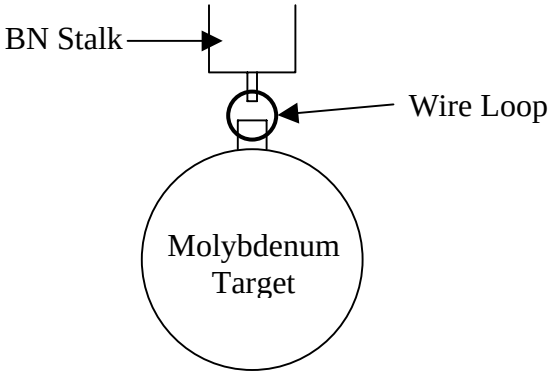

Figure 10-1: Initial Molybdenum Cathode Connection with Wire Loop

The high-voltage power supply shut down many times due to breakdown. The filaments in the chamber blew their fuses on numerous occasions. The arcing was not seen visually, but the current on the meter indicated problems. The arcing also caused noise problems in the proton detector. Adjusting the parameters such as pressure, filament bias, and current did not appear to help. In general the target was not able to operate over 70 kV.

It was suspected that the wire loop with its sharp points was the culprit for the breakdown problems. The connection was modified to that shown in Figure 10-2. A

hole was drilled into the top of the target for the high voltage line to slip into. Then a pin was used to keep the target attached. This design eliminated the sharp points.

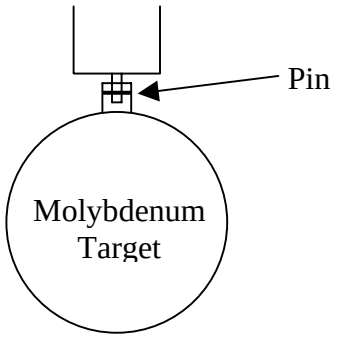

Figure 10-2: Molybdenum Cathode Pin Connection

The pin connection made a huge difference. The first run after up-to-air reached 100 kV, and the device was much more stable. The first activation run using D-^{3}He was run at 110 kV, 30 mA, and that condition was sustained for about 15 minutes without interruption. A follow up run to verify results about 6 months later used the same connection. For that run, the device sustained 120 kV, 30 mA for about 20 minutes.

10.1.2 ^{94m}Tc Production

The first activation experiment using the molybdenum target was run 684. During the run, it took 10 minutes to ramp up from 40 to 110 kV, and then 110 kV was held for 15 minutes. The current was kept at 30 mA for the entire run. After the run ended, it took 30 minutes to shut down the device, vent the chamber, and take out the target to be counted. A one-hour count was then started on the NaI detector. Figure 10-3 shows the spectrum with background counts subtracted out.

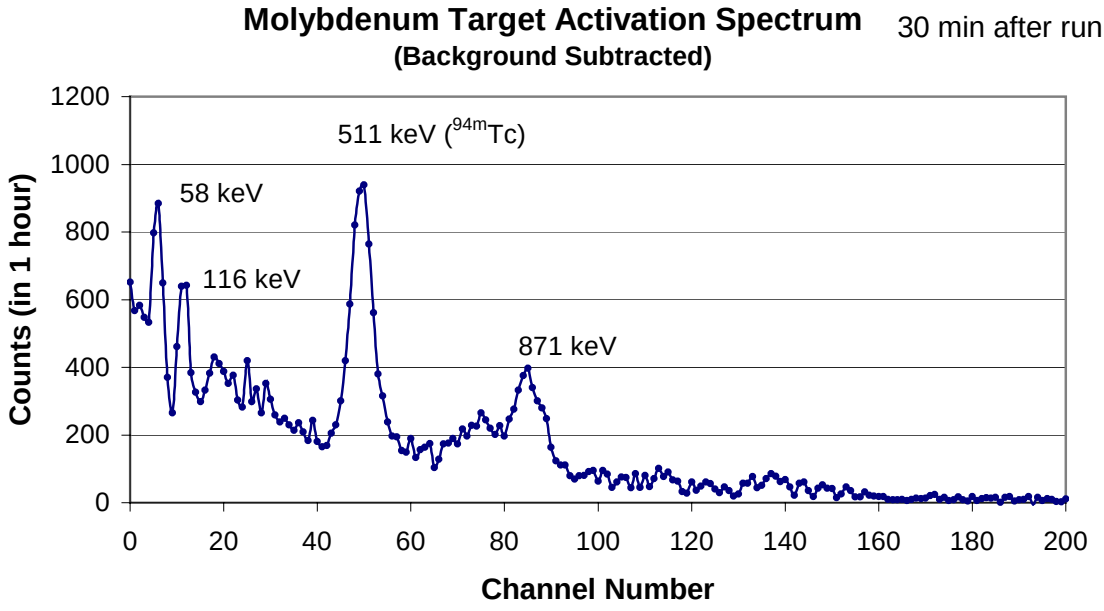

Figure 10-3: Sample Spectrum from ^{94m}Tc Production

The lower energy peaks on the left are due to characteristic x-rays from the detection setup. The peaks of interest are at 511 and 871 keV. The 511 keV peak is due to the positron annihilation, so this is a direct indication of ^{94m}Tc production. The 871 keV peak is from the gamma ray that is released in conjunction with the positron during decay of ^{94m}Tc. Since there is one 871 keV gamma and two 511 keV gammas given off with each decay, it makes sense that the 871 keV peak is about half the height of the 511 keV peak. This particular spectrum indicates a ^{94m}Tc activation of about 1 nCi at the time of the count.

Experiment 805 was run to reproduce the previous results but also to push the rates and determine the experimental half-life. During the run, D-^{3}He proton rates were measured every two minutes. The graph of the proton rate vs. run time is shown in Figure 10-4. The rates were plotted using the embedded fusion calibration factor described in Part I, Chapter 7. This assumption should be correct since the proton

detector was far away, and because the target was thick enough to block protons coming from the far side. Because only half of the protons generated travel deeper into the target, only half of the proton rate on the plot was available for activation.

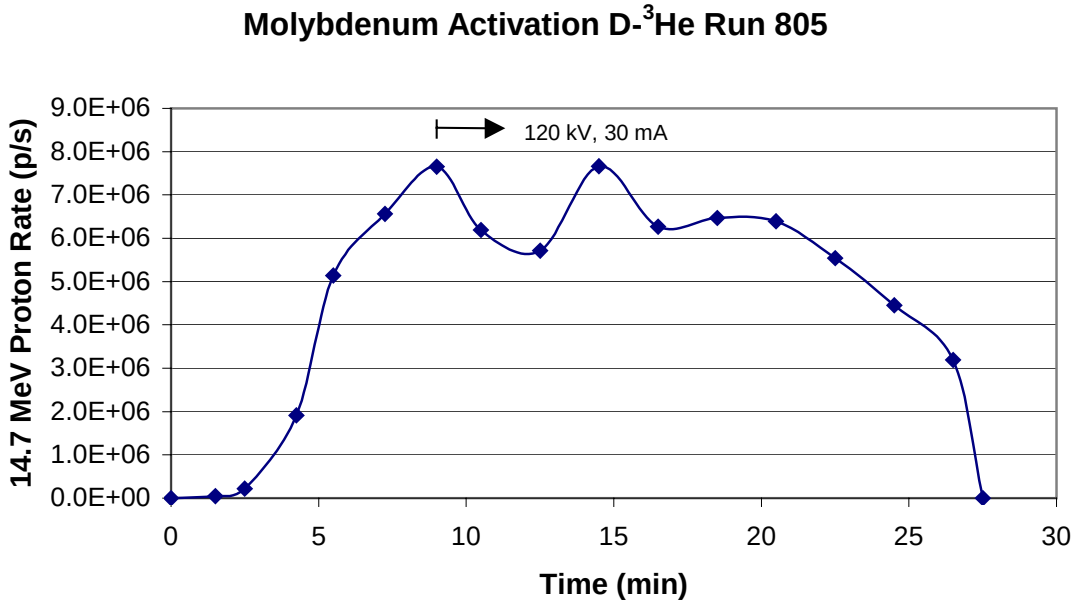

Figure 10-4: ^{94m}Tc Production Run

The initial climb in Figure 10-4 was due to increasing the voltage to 120 kV as shown. The variation at the top was due to an inability to keep the current steady; it varied ±3 mA. The drop off at the end was due to chamber heating that increased impurities in the device. The impurities made less current in the form of deuterium or helium ions. This graph was used to determine the theoretical ^{94m}Tc production yield at machine shutdown.

A set of sample calculations to figure out the yield are shown in Appendix B. An Excel™ spreadsheet was used to solve the problem numerically using distance steps into the target. For the first distance step, the proton energy (E) started out at 14.7 MeV. The cross-section (σ) for ^{94m}Tc production was calculated from tables for this energy. The

^{94}Mo number density, n (cm^{-3}), was found for that occurring in natural molybdenum. The following equation calculated the production rate in each step:

$$R_P = R_r \sigma(E) n x \qquad \text{Eq. 10-1}$$

The reaction rate or proton rate heading into the cathode is R_r (s^{-1}), x is the distance traveled in that step (0.001 cm), and R_p is the production rate of ^{94m}Tc in that distance (s^{-1}). At the end of each step, slowing down equations were used to determine the proton energy left over. With this new proton energy, the next step was calculated. After the proton lost enough energy so that the cross-section became negligible, all the R_P numbers were added up to get a total production rate for a given reaction rate.

Because the reaction rate changed during the run, Figure 10-4 was split up into two-minute segments, and the production rate was determined for each segment. Assuming a constant reaction rate over the two minutes, multiplying by time gave the number of ^{94m}Tc isotopes produced. Then, the isotopes calculated in each time segment were allowed to decay until the time of the shutdown of the machine using the 52-minute half-life. Adding up all the pieces led to a theoretical end-of-bombardment activity of 1.8 nCi (see Appendix B).

Experimentally, the target was removed from the chamber as quick as was possible to shut down safely. A series of five counts were taken of the target, each for 15 minutes, all back-to-back. For each count, the activity was determined from the height of the 511 keV peak. The five activities as a function of time are shown in Figure 10-5. The plotted activities take into account all efficiency factors, so they show the total activity in the molybdenum sample as a function of time.

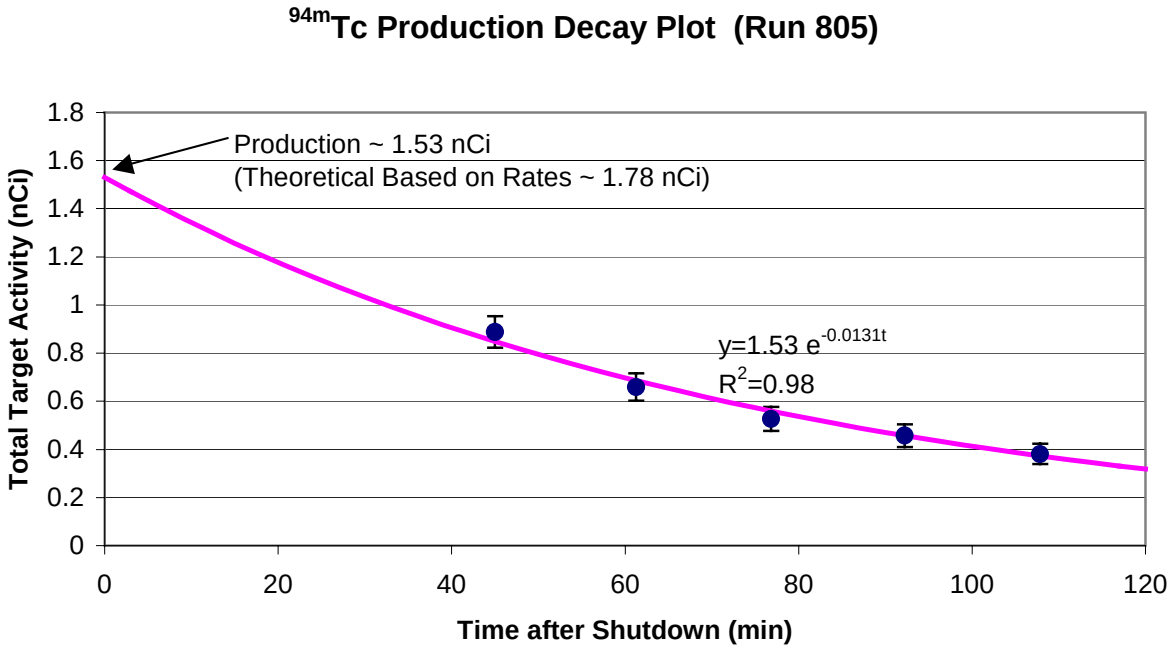

Figure 10-5: ^{94m}Tc Decay Plot

The activities are plotted as a function of time after shut-down to the middle of the count. The error bars shown include counting statistics and uncertainties in the measuring techniques. An exponential decay trendline was added to the data; the half-life was determined to be 53 minutes, a percent error of 1.9% away from the actual 52-minute half-life. It is obvious that the line fits the data very well. The y-intercept of this graph gives the activity at end-of-bombardment, which came out to be 1.5 nCi. The theoretical expectation of the production from the proton rates was 1.8 nCi, a percent difference of 18%.

The calibration used for the detection setup was somewhat complicated, and calculations are included in Appendix B. The activity was first calculated from the raw 511 keV peak with the background subtracted out. However, since two 511 keV gamma rays are released for each decay event, the activity was divided by two. The isotope only

decays by positron emission 82% of the time, so only 82% of the total isotope production was detected. The geometrical efficiency factor for the target on the flat detector was ~27%. The counting efficiency for this type of detector was ~17%. Finally, there was a shadowing factor. The activation only occurs in the outer layer of the target, and gamma rays born on the far side must pass through the target, getting attenuated, to reach the detector. The effect leads to a ~67% attenuation efficiency averaged over the entire 4π surface area. The total efficiency including all factors is 5%.

10.2 Al_2O_3 Target Operation

The layered target had many experimental difficulties associated with it. The ultimate goal of producing ^{13}N was not satisfied because the target was not able to sustain high voltages. The runs did show how a better target could be designed in the future, but this path was not taken since the idea was just a step in the isotope production process. Also, the cooled-target experiment had more success, so the effort was focused on the dynamic water target.

When the target was first installed, there were problems immediately with breakdown, even at 25-30 kV. Sparking was visibly evident at the connection with the high-voltage conductor. At one point, 40 kV, 10 mA was reached, but it did not last for more than a minute. Upon removing the target, it was found that the high-voltage connection was not good. There was either a very high or off-scale resistance from any point on the target surface to the conductor. In addition, the stub at the top of the target cracked off.

To attempt to salvage the idea, a wire loop configuration was used to cradle the target and make the connection. This appeared to work at first as the target reached 70 kV, 30 mA before breakdown. However, at the next run, severe sparking occurred where the wire loops contacted the target surface, and the current could not be pushed past 5 mA. Even changing the connection one last time did not help. The current was hard to control, and the voltage could not get past 40 kV.

By the end of these runs, the surface appeared to lose conductivity in some areas, especially at the bottom of the target. It seemed that the thin tungsten layer had sputtered away in areas. A thicker layer may have made the target last longer. The tungsten layer did not seem to crack or peel after the thermal variations during experimentation, so the actual adhesion to the aluminum oxide was good.

Figure 10-6: Al_2O_3 Target After Runs

Figure 10-6 shows the target after all of the runs. The broken stub at the top can be seen. The dark lines are from where the tungsten wire loops were holding the target. It appears that the dark coating formed where the wire was not actually attached to the

surface, probably due to arcing between the surface and wire. The top of the target is seen in this picture to be slightly darker than the bottom. The bottom is probably lighter due to more tungsten sputtering, revealing the white Al_2O_3 beneath.

Scanning electron micrographs were done of the target both before and after the runs, but unfortunately they did not shed any light on what happened. The before pictures showed a very rough surface on all magnification levels, and the after shots were not much different.

In general, the layered target had too many experimental difficulties associated with it to be useful. Improvements on the design are possible, but it was decided not to be worth the time and money. A solid target makes retrieval of the isotopes too difficult for any potential future use.

10.3 Cooled-Water Target

10.3.1 Operation and Difficulties

The cooled, stainless steel tube cathode initially had many difficulties to get over, but this rocky start was expected as it represented a drastic change from normal operation. Fortunately, most of the system ultimately worked as planned. The water cooling, pump, and heat exchanger were easily able to handle the heat load during runs. The ion exchange resin seemed to keep the water clear of excess ions, and it seemed to remove most or all of the ^{13}N that was produced. The upper stalk also seemed to work well. The swagelock connections around most of the outside of the chamber proved to be an easy way to make connections and changes. Also, the thin-walled stainless steel tube did not leak even after numerous runs. The two main problems were both associated with

the lower stalk. The lower stalk and tube design had problems with leaking the water into the chamber and problems with electrical breakdown.

The lower stalk was different from the upper stalk in that there was not a conductor traveling the length of it. The first design used plastic tubing to connect the thin-walled steel tube to the tubing at the bottom of the chamber at ground potential. This design did not allow for operation past 60 kV, and there was much flashing down the lower stalk. After three runs, a leak developed in the plastic tubing. The arcing appeared to travel down the outside of the plastic tube, causing a leak over time. The gap between the plastic tube and boron nitride stalk was filled with silicon glue for the next revision, but this caused out-gassing and further arcing problems.

It was then realized that the problem with the lower stalk was that it was a smooth path to ground, and the thick boron nitride was useless since there was not a conductor underneath. The lower stalk was then replaced with an aluminum oxide tube to carry the water, with boron nitride discs cemented to the outside (see Figure 10-7). The thought was that the disks break up the smooth path to ground. Eventually this new design seemed to work better to prevent the breakdown, and after a series of condition runs, voltages around 85 kV were sustained.

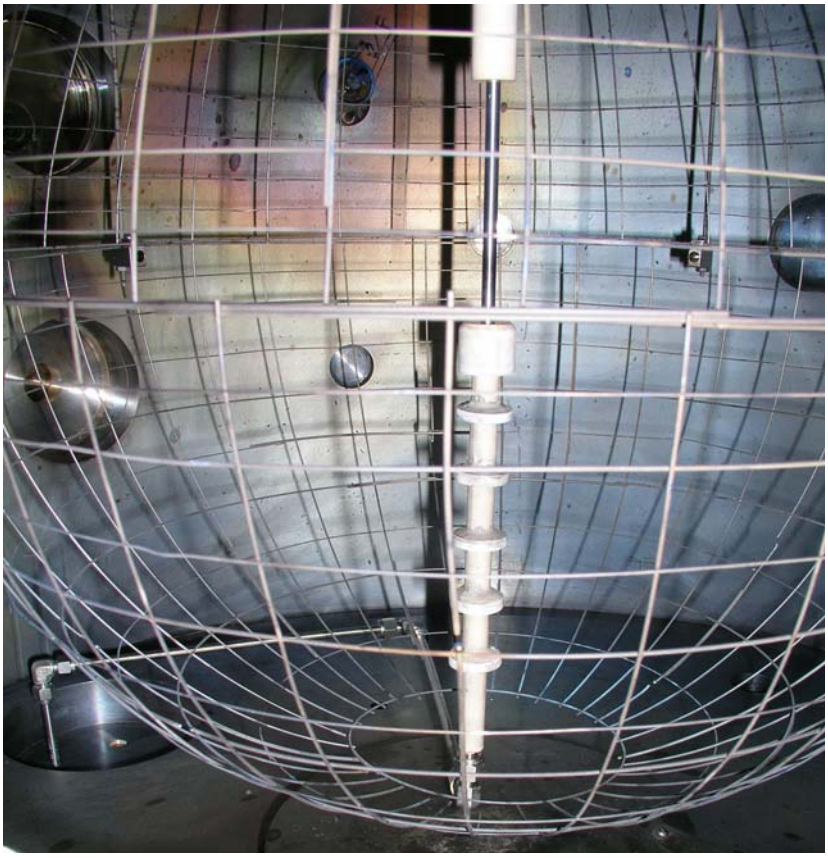

Figure 10-7: Revised Lower Stalk Design for the Water Cooled Target

The problem with the aluminum oxide tube had to do with leaking water into the chamber. The design was very rigid, and this caused the whole tube to crack during one run (see Figure 10-8) from the pressure the connections made. Also, it was difficult to make a good connection to the stainless steel tube. However, the run that reached 85 kV operated long enough to produce ^{13}N.

Figure 10-8: Cracked Al_2O_3 Tube

The chilled water supply kept the primary water loop at about 15.0 °C before high voltage and current were applied to the tube. The maximum power reached during a run was 85 kV, 30 mA at which point the temperature of the water after leaving the cathode was 31.1 °C. This result left a large margin for higher voltage and current operation.

10.3.2 ^{13}N Production

Two different runs were completed to produce ^{13}N for repeatability, but the results will be shown for the best run. In run 863, the water-cooled target achieved 85 kV, 30 mA for a few minutes before shutting down. This run produced enough D-^{3}He

protons for measurable activation. The proton production as a function of time is shown in Figure 10-9. The raw counts on the proton detector were converted to actual proton production using the embedded fusion calibration factor. The rates increased with voltage increase, and the highest point was at 85 kV with $4x10^6$ p/s.

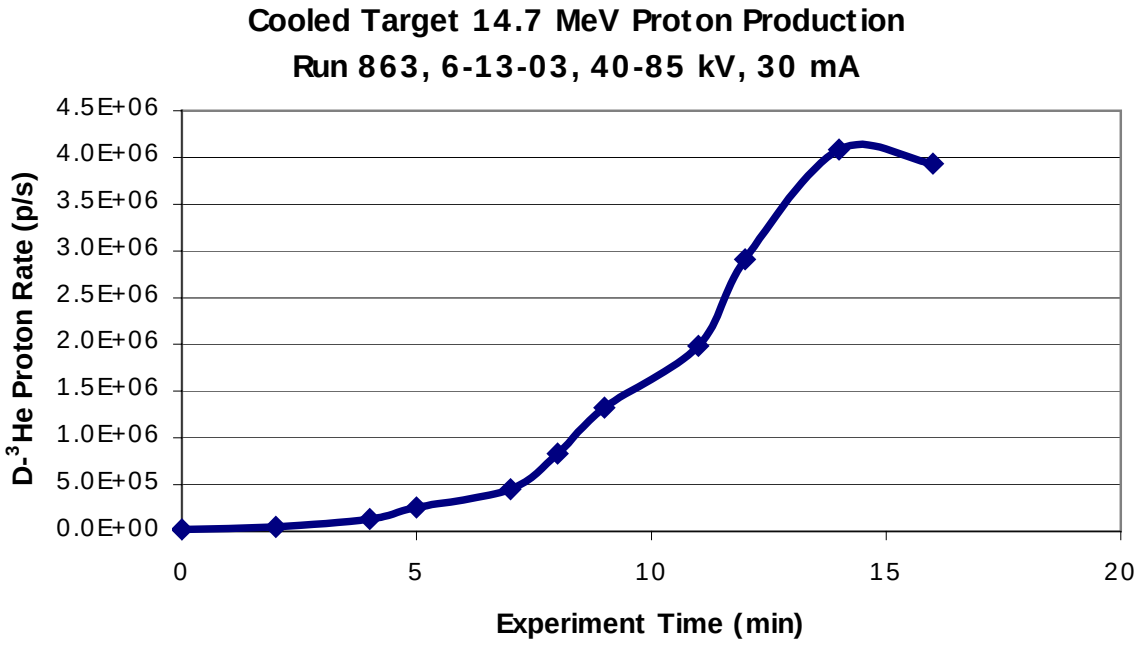

Figure 10-9: ^{13}N Production Run

At the end of the run, a series of five counts were taken on the NaI detector of the ion exchange resin. These counts were taken to verify the 10-minute half-life of ^{13}N and to be able to extrapolate back the activity produced. Figure 10-10 shows the gamma ray spectrum from the first count.

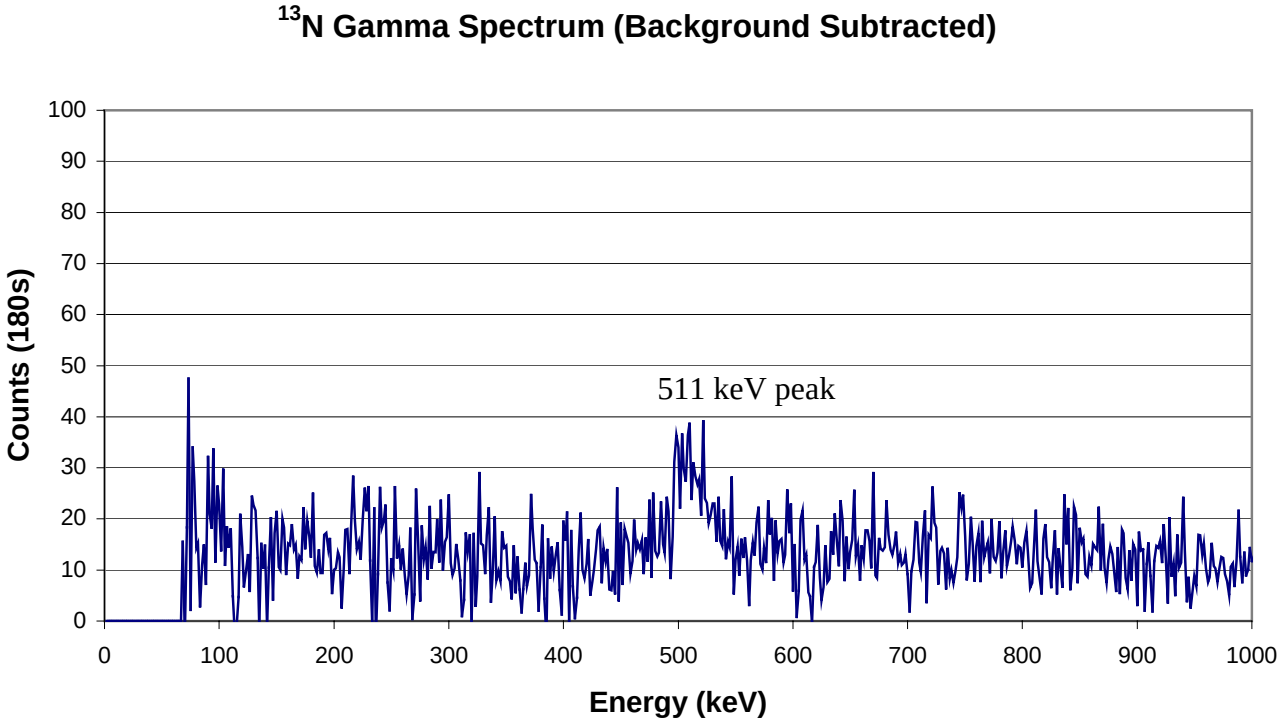

Figure 10-10: Sample Spectrum from ^{13}N Production

The 511 keV gamma peak is seen on this graph, though it is clearly not a large peak. There was much scatter in the data since a 180 s count was taken. Unfortunately, because of the short half-life of ^{13}N, this problem could not be alleviated. This scatter led to large uncertainties in the activities.

Figure 10-11 shows the results of the five counts taken after run 863. The activity of the 511 keV peak was plotted against time after the machine shut down (end of bombardment). The counting rates were transformed into activity (see Appendix C) taking into account the detector efficiency (17%), geometry efficiency (25%), gamma rays released per decay (2), and attenuation effects (75%). An exponential decay trend line was fit to the data to find an experimental half-life of 10.4 minutes. The line fits the

data points well, verifying that ^{13}N was indeed produced. This result is a percent error of 4% from the actual 10-minute half-life. The trend-line was used to determine that about 1.0 nCi of ^{13}N was produced at end of bombardment. The error bars on the graph show the large uncertainty in the measurements.

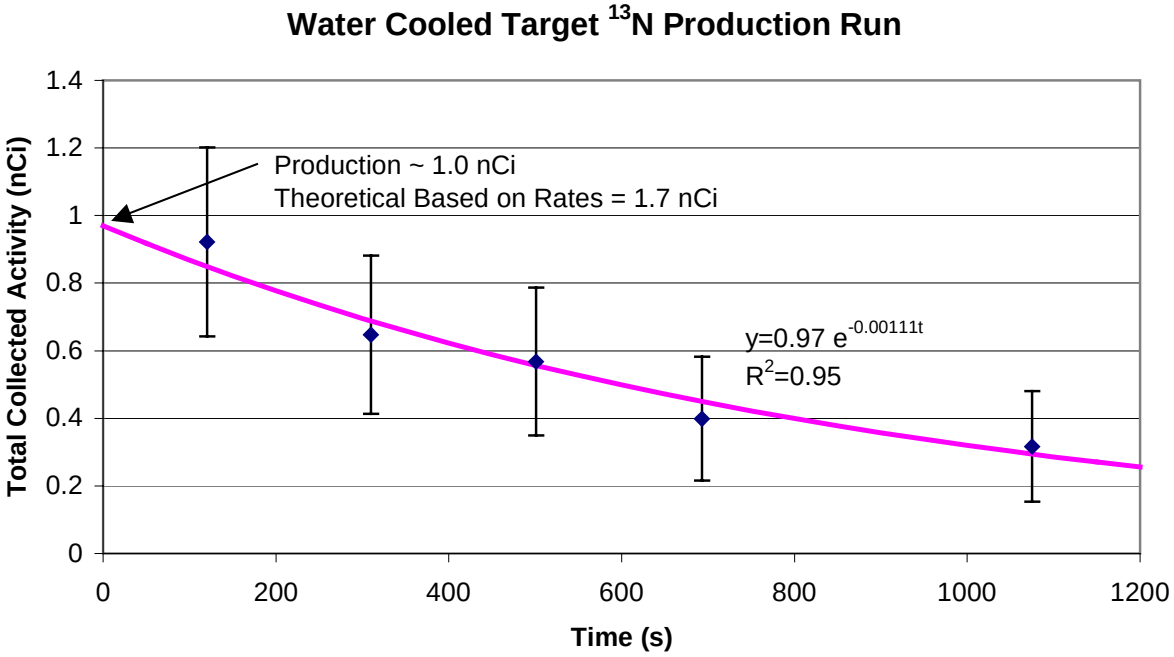

Figure 10-11: ^{13}N Decay Plot

The measured proton rates during the run were used to determine a theoretical value for how much ^{13}N should have been produced. This calculation was done similarly to the ^{94m}Tc production, except the stopping powers and cross-sections were used for water (see Appendix C). This number came out to be about 1.7 nCi. The difference in the theoretical and experimental production could be partially due to the approximations in the efficiency calculations. More likely, the difference is probably due to the collection efficiency of the resin column. The resin may not have been able to remove all of the ^{13}N, or the isotope may have gotten trapped in other areas of the coolant loop.

Chapter 11 Medical Isotope Production Discussion

From the onset of the isotope experimentation, the solid targets did not seem to make for an attractive production system. However, the molybdenum target was valuable for proof-of-principle investigation. The Al_2O_3 target with the tungsten coating had serious experimental difficulties. Ultimately, the water-cooled target seemed to have the best hope for producing ^{13}N using the IEC device.

It may be that the IEC design is not the ideal geometry for this type of experiment. If a simple way were developed to produce a deuterium and helium-3 beam at similar currents and energies that the IEC produces, a beam-target system may be better. Such a system would simply involve a beam hitting a target at ground potential. This could allow the target to be located at the wall of a vacuum vessel. It would be at ground potential, perhaps easier to cool, and perhaps more easily developed to be able to produce other types of short-lived PET isotopes.

The advantage of the IEC project is that the equipment was readily available for this experimentation. Also, a large amount of time was spent on designing the high-voltage feed through for the IEC to be able to sustain high-voltage, steady state operation. The high voltage operation has allowed the project to achieve higher operating voltages than similar plasma experiments.

11.1 Maximizing the Production Yield

The current ^{13}N yield is on the order of nCi's. For medical applications, the yield would have to be on the order of mCi's to even be considered. The next step in the

experimentation then is to push the production yield. The variables that can be changed to do this are ion energy, ion current, run time, and ion density.

The cross-section for the D-^{3}He reaction rises strongly with voltage in the voltage range of the experimentation. In addition, a higher energy ion travels farther into the cathode material. This gives it more time to have a chance to fuse with an embedded ion. The maximum voltage of the supply is 200 kV. For 200 kV deuterium ions traveling into a target, the production yield will be 44 times larger than for the 85 kV condition which was the maximum experimental voltage. This calculation was done with the computer model as outlined in Part III, Chapter 14.

The production yield is directly proportional to the ion current, so doubling the ion current doubles the yield. The present ion current is estimated to be around 1-2 mA due to a high secondary electron emission coefficient (See Part III, Chapter 14). With a large enough power supply, it may be possible to increase this current by one or two orders of magnitude. The power supply of the present system is limited to 75 mA, but that includes the secondary electron emission.

The run time can also be extended to increase production yield up to a certain extent. The highest yield ^{13}N production run unfortunately only reached the highest voltage condition for a few minutes. The run time can only help rates up to a few half-lives of the produced species before a saturation rate is achieved. This saturation rate could increase the yield by another order of magnitude, though.

Finally, the ion density may be able to be increased by a different choice of target materials. Certain materials have a high affinity for adsorption of gases, particularly hydrogen and its isotopes. Some of these materials can hold a 1:1 hydrogen to metal

atom ratio. This ratio is over 2 orders of magnitude above the estimated number density of helium in the stainless steel. Perhaps a material like palladium or titanium could be used as the tube.

Altogether these four adjustments could increase the total production yield by six orders of magnitude. These changes are much easier said than done. It will be difficult to increase the voltage to 200 kV, and the current may not be able to go much higher with the present power supply. The run time could certainly be increased. A change of tube material may help the deuterium retention, but the low-pressure chamber operation may place a limit on the maximum number density.

Chapter 10 discussed how isotope production is typically reported in mCi/μA proton beam current. It seems that for the IEC beam-target case, it is possible to report the maximum production as mCi/mA in which the current refers to the fusion ion current reaching the cathode (not the proton current). From Equation 8-4 we know the activity produced (infinite radiation time) as a function of proton current:

$$A = n_{par} I_p \int_0^{E_p} \frac{\sigma_i(E)}{S_{par}(E)} dE \qquad \text{Eq. 11-1}$$

In this equation, n_{par} is the number density of the parent material to be activated, I_p is the D-^{3}He proton current [p/s], σ_i is the cross-section for isotope production, and S_{par} is the stopping of protons in the parent material. This integral is evaluated from the initial proton energy down to zero.

From Equation 4-3, we know the embedded fusion rate which is also equal to the proton production rate, or the proton current:

$$I_p = I_{fi} n_{fi} \int_o^{E_i} \frac{\sigma_{fus}(E)}{S_D(E)} dE_i \qquad \text{Eq. 11-2}$$

In this equation, n_{fi} is the embedded fusion ion density, I_{fi} is the fusion ion current, σ_{fus} is the cross-section for fusion, and S_D is the stopping of the fusion ions in the cathode material. Since D on ^{3}He fusion dominates, n_{fi} can be set to the helium density in the cathode and I_{fi} and S_D can refer only to the deuterium current into the cathode. This integral is evaluated from the initial fusion ion energy down to zero. The integral was evaluated numerically.

Using the water-cooled cathode case of producing ^{13}N, Equations 11-1 and 11-2 were combined to find the maximum activity that would be produced with the beam-target D-^{3}He method. Assuming a cathode voltage of 200 kV (the maximum in the present experimental setup), all variables are known except for I_{fi} and n_{fi}.

$$A = 6.05 \times 10^{-27} I_{fi} n_{fi} \qquad \text{Eq. 11-3}$$

In this equation, I_{fi} must be in mA, and n_{fi} must be in ions/cm^3. Equation 11-3 takes into account the fact that only half of the protons are available for activation. Assuming the steel tube could hold a 1:1 helium to metal ratio, the activity produced by this setup is equal to:

~ 0.0012 mCi/mA

This final yield implies that a deuterium current of about 800 mA is required to produce 1 mCi of ^{13}N. For a beam-target setup at 200 kV and under the best case scenario of implantation density, beam currents on the order of amps would be needed to produce isotopes for medical doses in this manner. The power requirements for these parameters would make the IEC device into a non-mobile unit and drive up the costs. It will

probably be only through an advanced, converged core mode that the IEC device will be able to generate the D-^{3}He rates needed for isotope production.

11.2 Improving the Experimental Setup

If future work should occur with the cooled-cathode experiment for producing ^{13}N, some changes should be made to the system. As discussed previously, the biggest weakness in the design was in the lower stalk and the connection to the ceramic tube. The upper stalk seemed to have no problems.

A solution to the breakdown and leakage problems would be to make an identical oil-filled feedthrough and insulator on the bottom of the machine. Both the upper and lower stalks would be identical with a single thin-walled steel tube traversing the entire height of the vacuum chamber. It may be difficult to assemble this kind of setup, but it would probably allow for higher voltage operation, and leaks should not be a problem.

This idea was in fact the original design, but it was changed because the turbo pump lies at the bottom center of the chamber. This design would involve moving the pump and buying a few new flanges (and the new feedthrough) to make it work. At the time, it seemed like an unnecessary change; the problems with the lower stalk were not foreseen.

Part III: Ion Implantation

Chapter 12 Ion Implantation Theory

The previous part showed how embedded fusion reactions were successfully used to produce isotopes in the IEC device. Embedded reactions are driven by ion implantation in the cathode, so it was a natural extension of this work to learn more about the implantation process. The embedded reaction rate is dependent on the buildup of ions in the cathode which in turn depend on how the gases behave in metals. The actual ion current into the cathode is also important to know for the analysis. Ion implantation can both affect surface properties and possibly the device performance, so morphology changes should be known. The following sections outline the literature available on the subject as it pertains to this work.

12.1 Gases in Metals

When ions are forced into a metal during implantation, a number of effects can occur depending on the ion type. Hydrogen isotopes tend to be more mobile in metals, whereas helium isotopes tend to get trapped and precipitate in bubbles. Therefore, deuterium and helium will affect the metal in different ways. The mobility of these isotopes determines how much they will build up in the sample and what effects they may have on the surface properties of the metal.

12.1.1 Hydrogen Behavior in Metals

Different metals have varying abilities to store gases within their lattices. Palladium for example was used in “cold fusion” experiments [1] due to its strong ability

to adsorb hydrogen isotopes. Under the right conditions, Pd can hold as much as a 2:1 hydrogen to metal ratio. Titanium also can hold a sizeable quantity of hydrogen isotopes due to its ability to form hydrides at room temperatures. However, the hydrides are not stable at high temperatures (~300°C). Titanium hydride can be created with as high as a 2:1 hydrogen to metal ratio. This metal forms an fcc crystal structure, and the hydrogen lies at the tetrahedral interstices [2]. The addition of the hydrogen, while only interstitially, increases the specific volume of the structure slightly.

The metals that do not form hydrides simply adsorb hydrogen isotopes into the interstitial sites in the lattice. This adsorption is determined by permeability (K), diffusivity (D), and solubility (S), related by the equation [3]:

$$K = DS \qquad \text{Eq. 12-1}$$

In general, materials with a high diffusivity and solubility also have a high permeability. For hydrogen isotopes in metals, the dissolved concentration (C) is related to outside gas pressure (P) by [3]:

$$C = SP^{1/2} \qquad \text{Eq. 12-2}$$

To load up a metal with deuterium, a metal sample is immersed in a high-pressure deuterium environment. Metals with high solubilities are desirable for hydrogen retention.

The grid used in the UW IEC device is made of a 75% tungsten-25% rhenium alloy. Both of these metals are similar in properties. Tungsten forms a cubic crystal structure. It has a lower diffusivity for hydrogen isotopes when compared to titanium or palladium and does not form hydrides [3]. Figure 12-1 shows the hydrogen diffusivities

for various metals as a function of temperature. Tungsten has one of the lowest diffusivities.

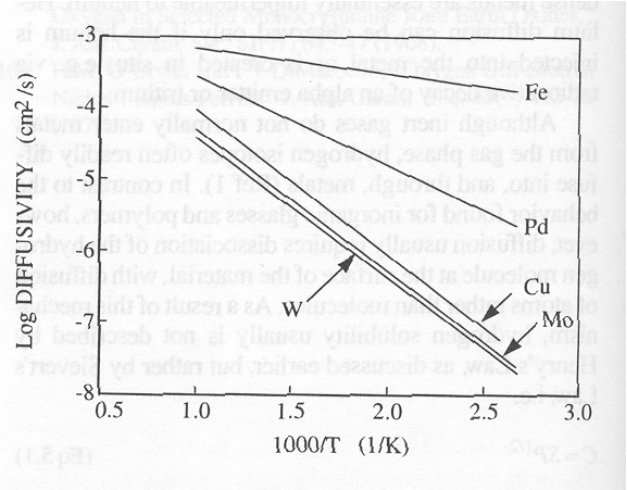

Figure 12-1: Hydrogen Diffusivity for Various Metals [3]

Likewise, tungsten also has a low permeability for hydrogen isotopes. Figure 12-2 shows the permeability as a function of temperature for some metals. Metals such as palladium and iron are very permeable to hydrogen.

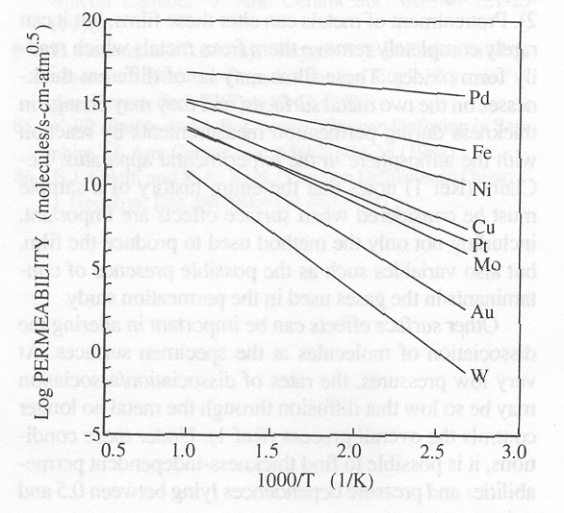

Figure 12-2: Hydrogen Permeability for Various Metals [3]

The behavior of hydrogen isotopes in metals or other materials has been of increased importance in magnetic confinement fusion reactors. Plasma facing materials

in tokamaks are subjected to continual ion implantation by hydrogen and helium. Tungsten has played an important role [4] due to it high melting point and high threshold for sputtering. The difference from the IEC components is that the tokamaks experience ions of at most a few keV where the IEC device deals with 10's to 100's of keV. The retention of gases inside reactor walls can affect fuel inventories, plasma density control, and confinement. The concentration of the gas, C_s, can be found from the following differential equation [4]:

$$\frac{\partial C_s}{\partial t} = D\frac{\partial^2 C_s}{\partial x^2} + \Phi P(x) - \sum_i S_i \qquad \text{Eq. 12-3}$$

The flux of ions is Φ, the depth distribution is P(x), and S_i represents any sources or sinks in the material.

In tokamak research it is important to keep track of the amount of tritium and deuterium in the reactor components. The solubility and diffusivity of hydrogen isotopes in tungsten must be known. An experiment by Frauenfelder [5] in 1969 gives a commonly accepted expression for diffusivity in tungsten over the temperature range of 1200 to 2400 K:

$$D\left[\frac{m^2}{s}\right] = 4.1\times10^{-7}\exp(-0.39eV/kT) \qquad \text{Eq. 12-4}$$

Likewise the solubility over the same range was found to be:

$$S\left[\frac{H}{W}atm^{1/2}\right] = 9\times10^{-3}\exp(-1.04eV/kT) \qquad \text{Eq. 12-5}$$

The solubility is given as a ratio of hydrogen atoms to metal atoms (H/W), and as a function of the square root of pressure. The diffusion at the surface of a cathode can be

determined by setting the gas diffusion equal to the recombination rate as the ions leave the surface [6]:

$$-D\left[\frac{\partial C_s}{\partial x}\right]_{x\to 0} = 2K_r\left[NC_s(x\to 0)\right]^2 \qquad \text{Eq. 12-6}$$

In this equation, C_s represents the concentration, K_r is the recombination rate coefficient, and N is the atomic density.

The processes described by Equations 12-3 through 12-6 are the ideal case in a uniform material structure. Ion implantation is complicated by the presence of traps or grain boundaries where ions can collect [7]. Traps can result in larger implantation densities and differing diffusion rates, so these ideal equations usually cannot be used to predict implantation densities. Irradiation of surfaces increases the trapping sites. The subject of trapping is a very detailed subject and outside the scope of this work.

12.1.2 Helium Behavior in Metals

Helium and other inert gases are impermeable to metals under normal conditions. That is to say that metals will not adsorb helium and have very low solubilities. Therefore, when helium ions are implanted into a metal, they do not stay uniformly distributed throughout the metal lattice. The helium collects to form bubbles, and when the bubbles form just below the surface, it is known as blistering. Bubble formation can also lead to a trapping site for deuterium. This well known phenomena is an issue in many fusion devices [5].

The ^{3}He used in the IEC device has the potential for bubble formation within the grid wires. If embedded ^{3}He is responsible for some of the fusion reactions taking place,

the number density of bubbles and ^{3}He within the bubbles will be important to quantify. There is a critical total fluence of helium ions before blistering can occur. For molybdenum, this fluence is 4-5x10^{17} ions/cm^2 [8]. For rhenium, a close element to tungsten, it is about 3x10^{17} ions/cm^2 [9]. A typical D-^{3}He experiment on the UW IEC implants about 1 mA of ^{3}He for 30 minutes, a fluence of 1.5x10^{17} ions/cm^2 over the grid wires (total area ~ 74 cm^2). Therefore, bubble formation is expected in the IEC.

Blister formation commonly occurs in metals under helium implantation up to elevated temperatures. However, at high temperatures the helium bubbles are able to move through the sample more. An experiment by Thomas and Bauer in 1974 [10] showed the results of helium implantation on Vanadium at high temperature. See Figure 12-3. At these conditions, the surface structure developed a porous morphology. The authors felt that the helium bubbles migrated to the surface to form the pores rather than

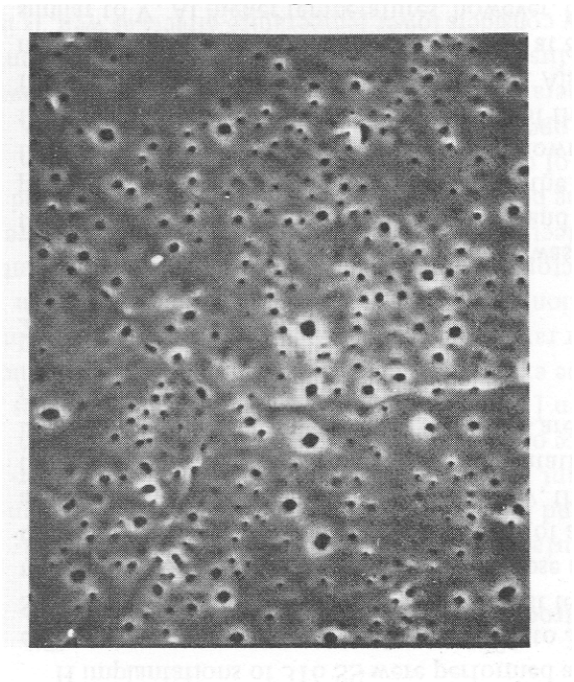

Figure 12-3: 300 keV Helium implantation on 1200 °C Vanadium at 2x10^{18} ions/cm^2 [10]

breaking the surface like in the case of low temperature implantation. It was the conclusion of the authors that this structure results in 100% helium re-emission during subsequent implantation. These conditions were close to the temperatures and fluences seen on the IEC cathodes.

12.2 Secondary Electron Emission

Ion bombardment of metal surfaces induces the emission of electrons, and this electron emission plays an important role in the IEC device. The electron emission must be known to get an accurate idea of the ion current hitting the cathode. The high voltage power supply measures the current, but it includes both the ion and electron components. The actual ion current must be known for determining the embedded fusion contribution. In addition, the re-circulation ion current through the grid is believed to be proportional to the ion current hitting the grid.

The secondary electron emission is reported in this work with the symbol γ, which stands for the number of electrons emitted per incident ion. Numerous experimental data is available for this phenomena, but unfortunately it varies widely depending on the ion type, metal, surface finish, angle of incidence, temperature, and other variables. The experimental setup is also important in regarding any data.

Specifically for helium ions on tungsten, the secondary electron emission values range from 2-3 [11] to 4-5 [12] around the 20-50 keV energy range. These experiments are done with an ion beam impinging a clean, smooth tungsten surface normal to the surface. Experiments with helium ions on molybdenum report γ as 1-2 on a degassed

surface and from 10-14 on a surface that had not been degassed over the 20-50 keV range [13]. The oxidation of a surface can also drastically increase the electron emission. Svensson and Holmen [14] reported that electron emission starts off very high in the beginning of experiments until the beam erodes away the oxidized surface. Finally, increasing angle of incidence can also increase the electron yield. Experiments with 250 keV deuterium ions on zirconium report γ as 5 at 0° (perpendicular) incidence, and up to 12 a 60° incidence [13].

Plasma source ion implantation is a plasma-aided manufacturing device that works similarly to the IEC device. This device pulses ions into a production part. The secondary electron emission has been measured between 5 and 20 [15] over energies similar to the IEC device, but the ion type and target material, are different from the IEC case. The only conclusion to draw from the literature review is that the secondary electron emission is particular to each experiment, and external data should be closely examined.

12.3 Modeling the Embedded Fusion Rate

In Chapter 4, Equation 4-3 showed how to calculate the embedded fusion rate. The equation is repeated here:

$$\frac{dN(x)}{dt} = I \cdot n(x) \cdot \sigma\left[E(x)\right]dx \qquad \text{Eq. 12-8}$$

Numerically, this equation can be solved by splitting the ion path up into distance steps in the cathode. The constants are a uniform ion current I that does not change through the sample, and a known implantation ion density profile n(x). For the first distance step into

the sample, the ions have the cathode voltage energy. The cross-section is calculated for that energy. Then the fusion rate for that delta x is solved using:

$$\dot{N}_i = I \cdot n(x) \cdot \sigma \cdot \Delta x \qquad \text{Eq. 12-9}$$

Then stopping power tables are used to determine the energy loss of the ions over the distance of the step. With a new energy, the process is repeated in the next distance interval. When the ion energy goes to zero, all of the reaction rates from each step are added up to find the total embedded reaction rate.

The two difficult variables to measure in Equation 12-9 are the implanted ion density, n(x), and the actual ion current into the grid wires, I. The ion density depends on the flux history of ions bombarding the grid, the grid temperature, and the behavior of gases in metals. It would be good to have an independent way to measure the density.

12.4 References

[1] D. Das & M.K.S. Ray, "Fusion in Condensed Matter-A Likely Scenario," *Fusion Technology,* **24**, 115 (1993).

[2] D. J. Malbrough, "Deuteron Stopping Cross Sections in Transition Metal Hydrides," *Nuclear Instruments and Methods in Physics Research,* **B28**, 459 (1987).

[3] J. E. Shelby, *Handbook of Gas Diffusion in Solids and Melts,* ASM International, Ohio (1996).

[4] N. Yoshida, "Review of Recent Works in Development and Evaluation of High-Z Plasma Facing Materials," *Journal of Nuclear Materials,* **266-269**, 197 (1999).

[5] R.A. Causey, “Hydrogen Isotope Retention and Recycling in Fusion Reactor Plasma-Facing Components,” *Journal of Nuclear Materials,* **300**, 91 (2002).

[6] T.A. Thorson et al., “Fusion Reactivity Characterization of a Spherically Convergent Ion Focus,” *Nuclear Fusion,* **38**, 495 (1998).

[7] M. Kaminsky, *Radiation Effects on Solid Surfaces,* American Chemical Society, Washington, D.C. (1976).

[8] C.R. Fahlstrom & M.K. Sinha, “Surface Blistering of Molybdenum Irradiated with 75-350 keV Helium Ions,” *Journal of Vacuum Science Technology,* **15(2)**, 675 (1978).

[9] J. Van Guysse et al., “Blistering of Rhenium Irradiated with 21 keV Helium Ions,” *Applied Physics,* **17**, 89 (1978).

[10] G.L. Thomas & W. Bauer, “Helium and Hydrogen Re-emission During Implantation of Molybdenum, Vanadium and Stainless steel,” *Journal of Nuclear Materials,* **53**, 134 (1974).

[11] D. Hasselkamp et al., “Ion Induced Electron Emission from Metal Surfaces,” *Nuclear Instruments and Methods,* **180**, 349 (1981).

[12] B. Dev, “Statistics of Secondary Electrons from W Induced by He Ions and Atoms at 0°-90° Incidence,” *Applied Surface Science*, **40**, 319 (1990).

[13] M. Kaminsky, *Atomic and Ionic Impact Phenomena on Metal Surfaces,* Springer-Verlag: Berlin, Germany (1965).

[14] B. Svensson & G. Holmen, “Electron Emission from Ion-Bombarded Aluminum,” *Journal of Applied Physics,* **52**(11), 6928 (November, 1981).

[15] D.J. Rej et al., “Magnetic Insulation of Secondary Electrons in Plasma Source Ion Implantation,” *Journal of Vacuum Science Technology*, **12**(2), 861 (March/April, 1994).

Chapter 13 Ion Implantation Experimentation

13.1 IEC Implantation

The grids and the solid targets run in the IEC device were subjected to large fluences (>10^{18} ions/cm^2) over many runs. These runs alternated between deuterium, helium-3, or runs with both gases. Although the exact fluence and ion energy were not known, the surface morphology of some of these cathodes was determined.

More controlled experiments were carried out using pure tungsten samples. This research was completed as part of the HAPL (High Average Power Laser) design study [1]. The HAPL study is devoted to developing a reactor design for an inertial fusion energy power plant that relies on lasers with a high repetition rate. The chamber wall must be designed to withstand the large ion, particle, and x-ray flux that hits it in repetitive, high-power bursts. Tungsten is one of the key materials being studied, so the effects of deuterium and helium implantation on tungsten are important to understand. This work then parallels the work on the IEC cathodes since they are made out of tungsten-rhenium.

The tungsten samples were provided by Dr. Lance Snead at Oak Ridge National Laboratory. The samples were made by powder metallurgy into flat squares or discs that had been polished to a mirror finish on one side (see Figure 13-1). The square samples were 1 cm on an edge, and the round samples were 1 cm in diameter.

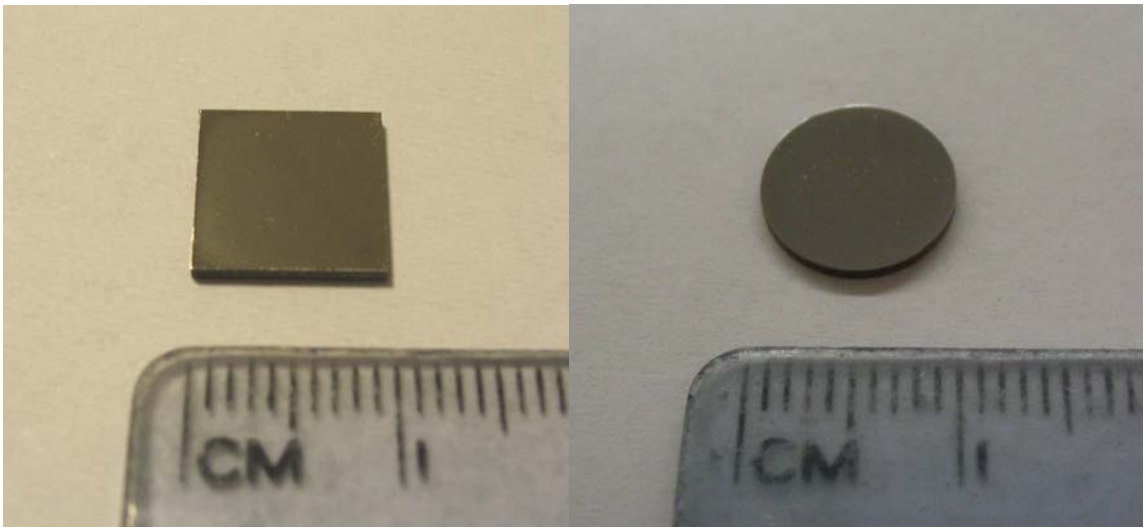

Figure 13-1: HAPL Tungsten Powder Metallurgy Samples

These samples were installed in the IEC chamber as shown in Figure 13-2. A tungsten-rhenium wire loop held the samples in either by a spring force or by spot-weldings, and this wire connected to the high-voltage feedthrough. The fusion ions were accelerated into the samples that replaced the gridded cathode. Figure 13-3 shows the samples during run conditions in which the samples glow a bright red or orange, representative of high temperatures.

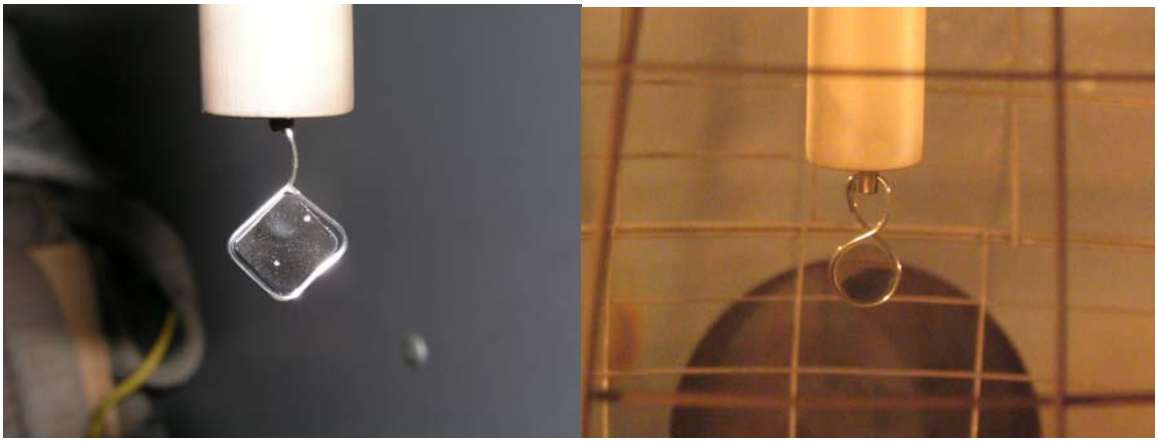

Figure 13-2: HAPL Tungsten Sample Installation

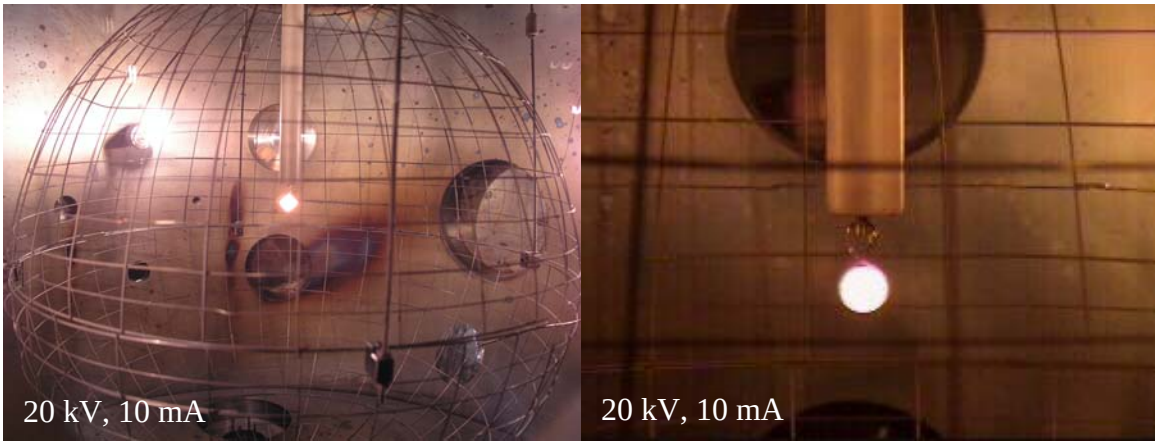

Figure 13-3: HAPL Tungsten Samples during Implantation Runs

A total of 20 experiments were done with the HAPL samples. One sample was run with deuterium ions, but all the rest were run with helium-4 ions. A fluence scan, voltage scan, and temperature scan were all completed using helium-4.

In the fluence scan, all parameters but the run time were kept constant. The voltage was set at 30 kV, the meter current was set to 6 mA, the pressure was held at 0.5 mtorr, and the temperature varied between 800 and 940 °C. Changing the run time changed the total fluence hitting the sample at a constant temperature. Four different samples were analyzed from $1x10^{16}$ to $6x10^{17}$ $^{4}He/cm^{2}$.

For the voltage scan, the fluence was kept at $3x10^{17}$ $^{4}He/cm^{2}$, and the current varied slightly to keep the temperature constant around 900 °C. The pressure was again held at 0.5 mtorr, and the voltage scan covered the range from 20 to 60 kV.

Finally for the temperature scan, the fluence was again kept constant at $3x10^{17}$ $^{4}He/cm^{2}$, the voltage was kept at 40 kV, and the current was adjusted to change the sample temperature. The pressure for all of these experiments was also kept at 0.5 mtorr. This pressure was lower than that used in normal IEC operation, but the reason was to

make the ions hitting the target all have as close to the cathode voltage as possible. Figure 13-4 summarizes the experiments carried out.

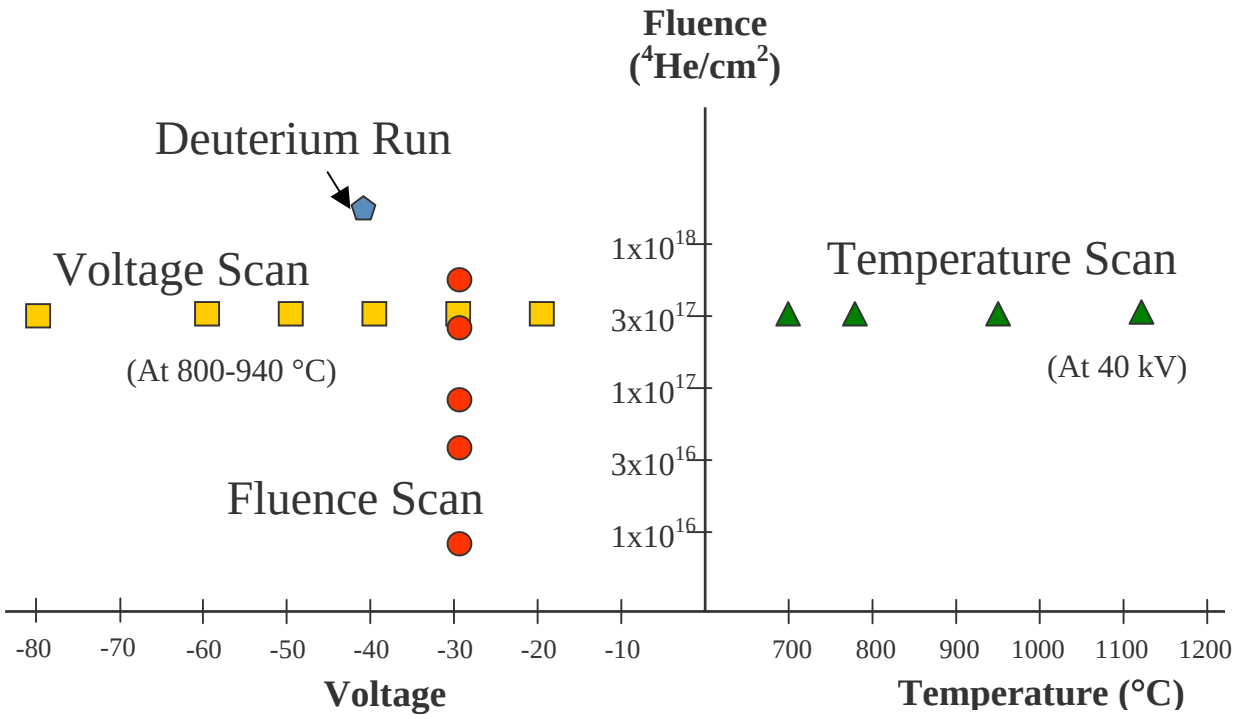

Figure 13-4: HAPL Implantation Experiments

For all of the implantation experiments, a pyrometer was used to measure the temperature of the sample surface. Temperature readings were taken normal to the sample surface throughout the run. After all of the samples were run, they were viewed under a scanning electron microscope to determine the effect of the ion implantation on surface morphology.

13.2 Scanning Electron Microscopy

For all of the implantation experiments and for some grid wires and solid targets, a scanning electron microscope was used to determine the surface morphology. In all cases, a picture was taken of the as-received samples to compare to the samples after irradiation.

The microscope used was a LEO 1530 Field Emission Scanning Electron Microscope. It has a resolution of between 1 and 40 nm depending on the voltage. This allowed for very clear pictures of surface features on the order of 0.1 μm. All of the samples were either cleaned or untouched by human hands before scanning. A few standard magnifications were taken of each sample for easy comparison.

13.3 Cathode Ion Current Determination

The pyrometer has proven to be a very useful tool for determining the actual ion current reaching the cathode in the IEC device. In the low-pressure environment in the chamber, the ion power into the cathode can only be rejected through radiative emission. With accurate temperature measurements the following equation can be used to determine the ion current:

$$\frac{VI_{meter}}{1+\gamma_{SE}} = \varepsilon A \sigma T^4 \qquad \text{Eq. 13-1}$$

This equation balances the input power (left) to output power (right), so it can only be used in a steady state case. The power supply voltage is V, I_{meter} is the meter current, and γ_{SE} is the secondary electron emission coefficient. The radiative power can be determined by knowing the emissivity of the sample (ε), the total surface area of the

cathode (A), the Stefan-Boltzmann constant (σ=5.67x10^{-8} W/m^{2}K^4), and the absolute temperature (T) in Kelvin.

Equation 13-1 actually is used to solve for the secondary electron emission, but this value can be applied to the meter current to determine the actual ion current. The emissivity of the cathode material is difficult to determine. Tables can be used, but the emissivity changes quite a bit depending on the surface conditions. For the HAPL experiments, two samples were sent to NASA Glenn Research Center to do accurate emissivity measurements. These experiments showed a total emissivity of 0.2 for the polished tungsten surfaces at temperatures around 1000 °C. Another assumption of the equation is that all of the ion current comes in at the full cathode potential. This assumption may not be the case at the pressures of operation because of charge exchange reactions.

The pyrometer is useful for measuring temperature as long as the temperature is constant over the cathode. For the solid cathodes, that was usually the case, but for the grids, different parts of the grid were hotter than others during runs. In that case, an average temperature was approximated. The pyrometer collects data in the chamber through a thick piece of vacuum glass. It uses a two-color mode that allows it to determine the temperature through glass and from a thin wire. The pyrometer was calibrated by heating up a W-Re grid wire resistively and using a thermocouple to determine the accurate temperature.

13.4 References

[1] J.D. Sethian et al., “Fusion Energy with Lasers, Direct Drive Targets, and Dry Wall Chambers,” *Nuclear Fusion*, **43**, 1693 (December, 2003).

Chapter 14 Ion Implantation Results

14.1 Surface Morphology

14.1.1 W-Re Grid Implantation

Scanning electron micrographs were taken of a few of the many grids run in the IEC device. Although the grids were run many times and with highly varying conditions, a particular surface structure did develop.

In an effort to clean one of the grids after a run, grid W-1 was sandblasted, cleaned, and then re-installed in the chamber. It did not run well, and had many problems with arcing and sparking off the wires. It was soon removed and a new grid was made. Most likely, the sand-blasting caused a very rough surface which created sharp electric field gradients at the surface. Figure 14-1 shows a comparison between the W-Re wire as received and the sandblasted surface.

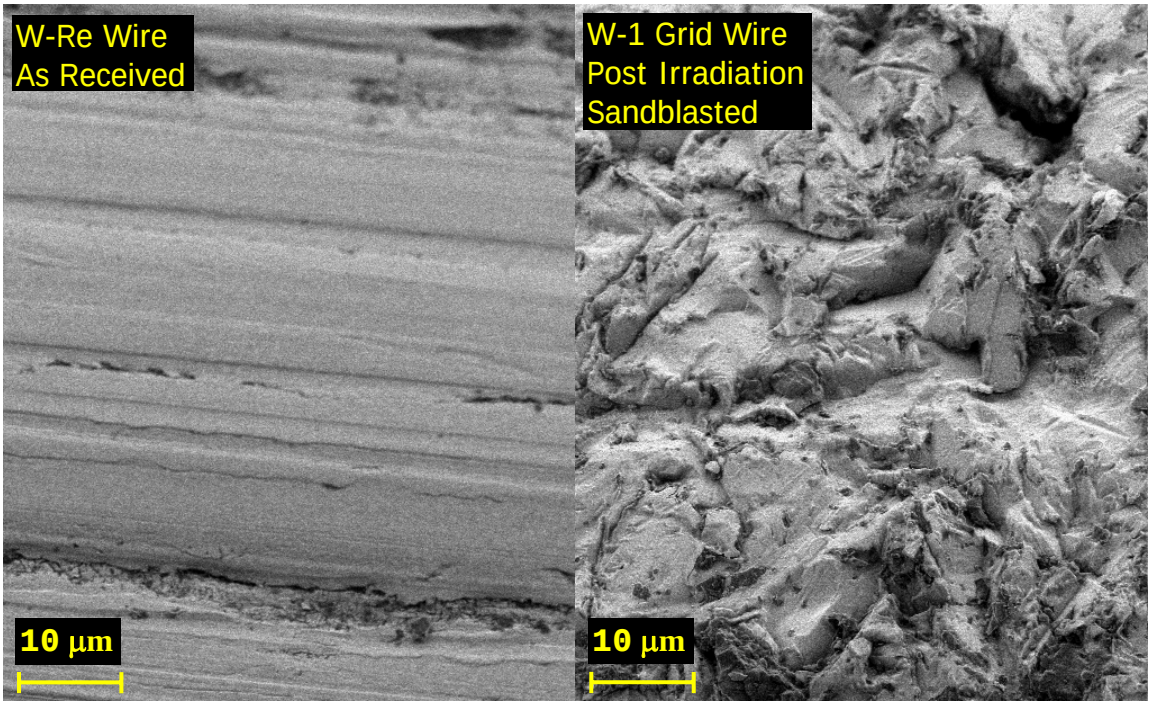

Figure 14-1: Comparison of New W-Re Grid Wire to Sandblasted Wire

Figure 14-2 shows a comparison of a new W-Re wire to a wire from grid W-3. This grid had been used in multiple D-D and D-^{3}He runs with voltages up to about 150 kV and temperatures up to 1300 °C. The ion bombardment created a porous surface structure. The pores appear to be less than 0.1 μm in diameter. It is not clear at this point if this structure affects device performance. What is known from experimentation is that grids can be run extensively with D-D without any degradation in performance. However, extensive running with D-^{3}He can cause problems maintaining the high voltages eventually. Running with only helium has caused enough problems to warrant replacing the grid with a new one. These ion implantation effects motivated the study on surface morphology.

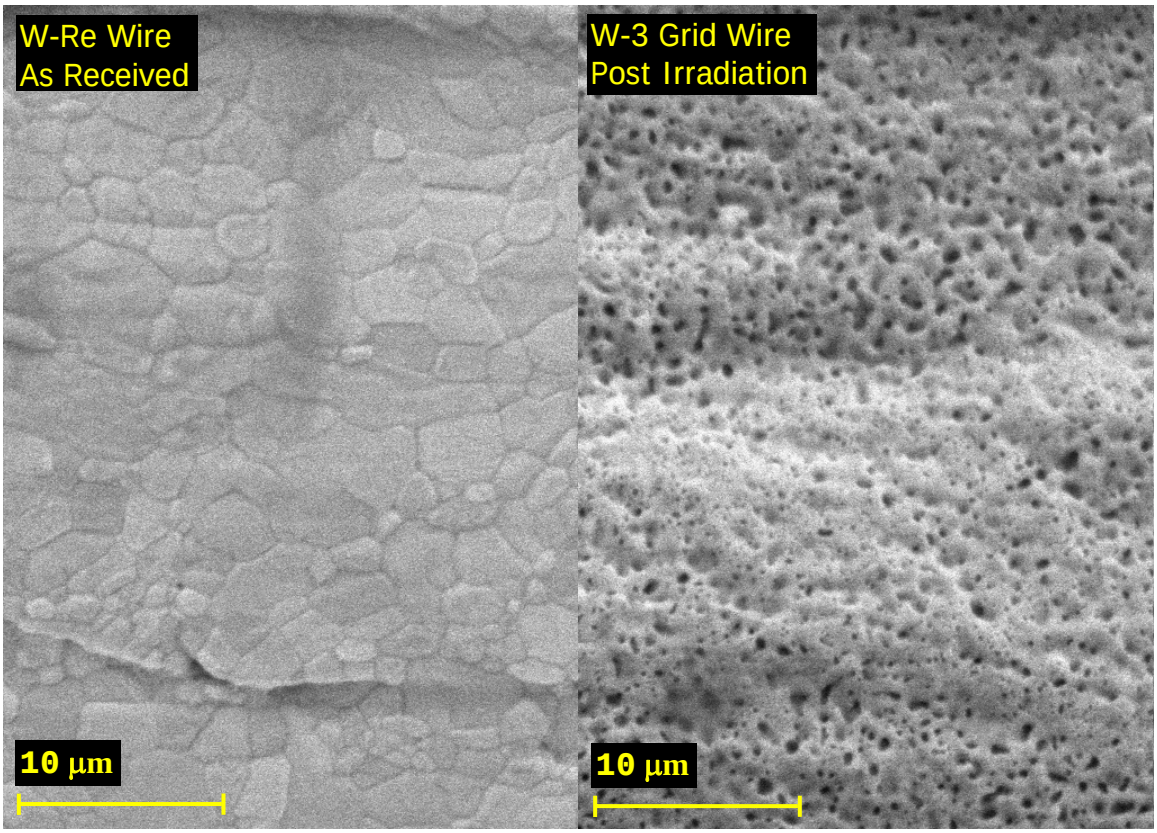

Figure 14-2: W-Re Grid Wire Comparison after Many D-D and D-^{3}He Runs

14.1.2 Solid Target Implantation

Similar results were seen with the solid titanium target. Again, the experiment was not controlled for ion implantation, but the surface was examined after the series of D-D and D-^{3}He runs. Figure 14-3 compares the top part of the target (which was protected from the ion flow by the stalk) to the bottom part (which received the highest ion flux). In essence, the picture on the left shows only the surface after heating (no temperature data was available), and the picture on the right shows the effects of the implantation. The pores that formed in titanium are much bigger on average than the pores from the W-Re grid wires.

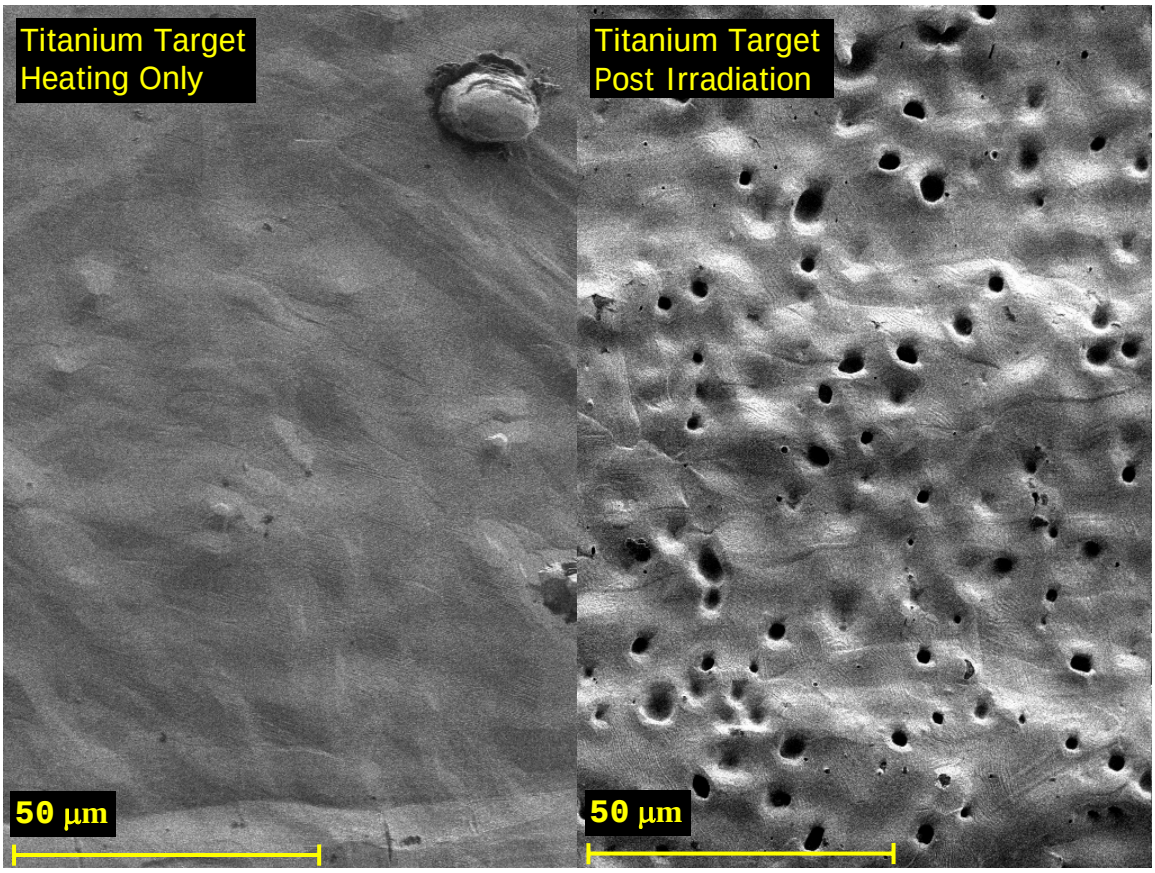

Figure 14-3: Titanium Target D-^{3}He Implantation Comparison

The porous structure was also seen with the molybdenum target as shown in Figure 14-4. Unfortunately, no picture was taken before to compare it to, but the pore formation is still visible. There appears to be more variation in the elevation of the surface, but this is probably because the surface was not polished before implantation. It also may indicate sputtering or erosion of the surface.

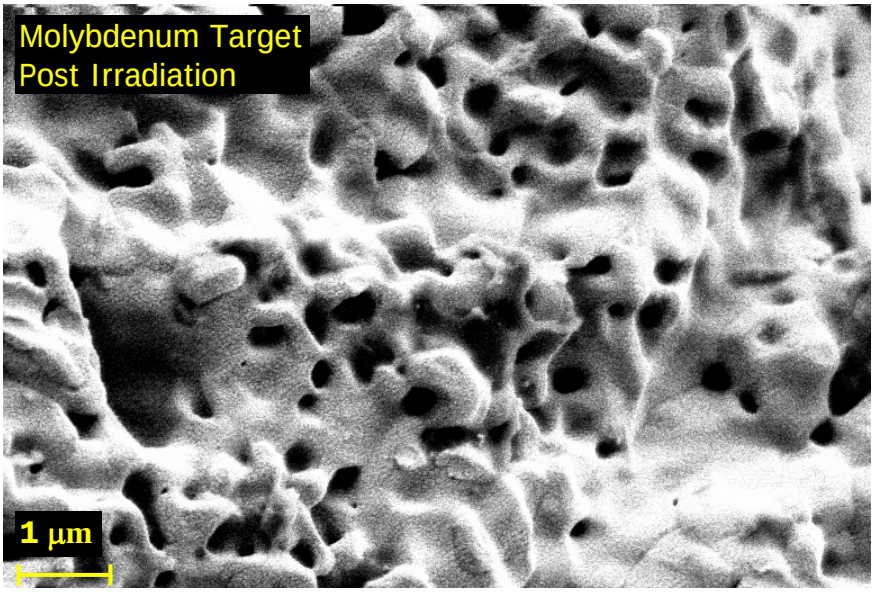

Figure 14-4: Pore Formation in the Molybdenum Target after D-^{3}He Runs

14.1.3 Tungsten Powder Metallurgy Sample Implantation

The implantation experiments on the pure tungsten HAPL samples were much more controlled. The first run using a square sample was with only deuterium. The sample was run with a chamber pressure of 2 mtorr and received a total deuterium fluence of 2×10^{18} D^{+}/cm^{2}. The voltage was varied between 20 and 40 kV over a total run time of about 32 minutes. The deuterium implantation did not cause any observable defects (> 0.1 μm) to occur in the surface such as a blister or pore formation. Figure 14-5

shows a comparison of the sample as received to the sample after the irradiation. The difference is that the irradiated sample experienced significant grain growth. This was most likely just due to the high temperatures reached (~1200 °C for about 20 minutes).

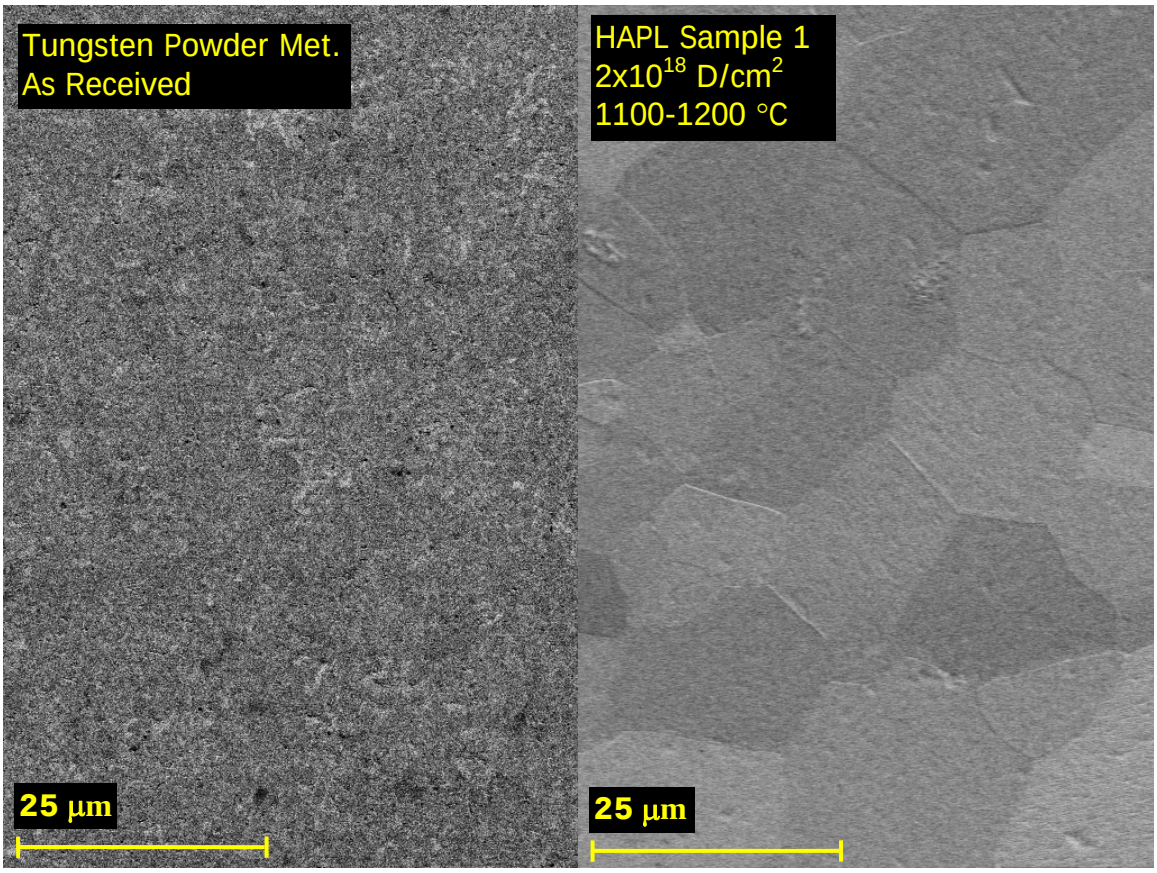

Figure 14-5: Deuterium Implantation on Tungsten Showing Grain Growth

The results from the helium implantation were quite a bit different. The helium fluence scan was completed at a constant 30 kV, 6 mA, 0.5 mtorr helium pressure. The temperature was difficult to control, but the average was held between 800 and 960 °C. Figure 14-6 shows six micrographs which outline the formation of pores in tungsten at high temperatures.

The upper left tile of Figure 14-6 shows the surface of the as-received sample. Sample 2 was implanted with $1x10^{16}$ $^4He/cm^2$ at 800 °C. Sample 3 shows the beginning of pore formation at $4x10^{16}$ $^4He/cm^2$ at 800 °C. Therefore, the threshold for pore formation is somewhere below the $4x10^{16}$ $^4He/cm^2$ level. The pores are localized at the grain boundaries. Sample 4 shows bombardment to $1x10^{17}$ $^4He/cm^2$ at 900 °C. The pores have increased, and the grain boundaries are no longer discernable. Finally, Samples 5 and 6 show implantation at $3x10^{17}$ $^4He/cm^2$ at 920 °C and $6x10^{17}$ $^4He/cm^2$ at 960 °C respectively. It appears that at some point between these two fluences, the pore diameter stabilizes, and the surface structure stabilizes as well.

For each of these micrographs, the average pore diameter and pore density were determined. This was accomplished using the Image Processing Toolbox in MatLab™. The program is able to distinguish the dark areas as pores, and through some manipulation of the picture, it can determine the pore size distribution. A sample of the code is shown in Appendix D. The average pore diameter and density is plotted in Figure 14-7. It appears from this plot that the average pore diameter stabilizes around 0.14 μm, and the density stabilizes around 7-8 pores/μm^2.

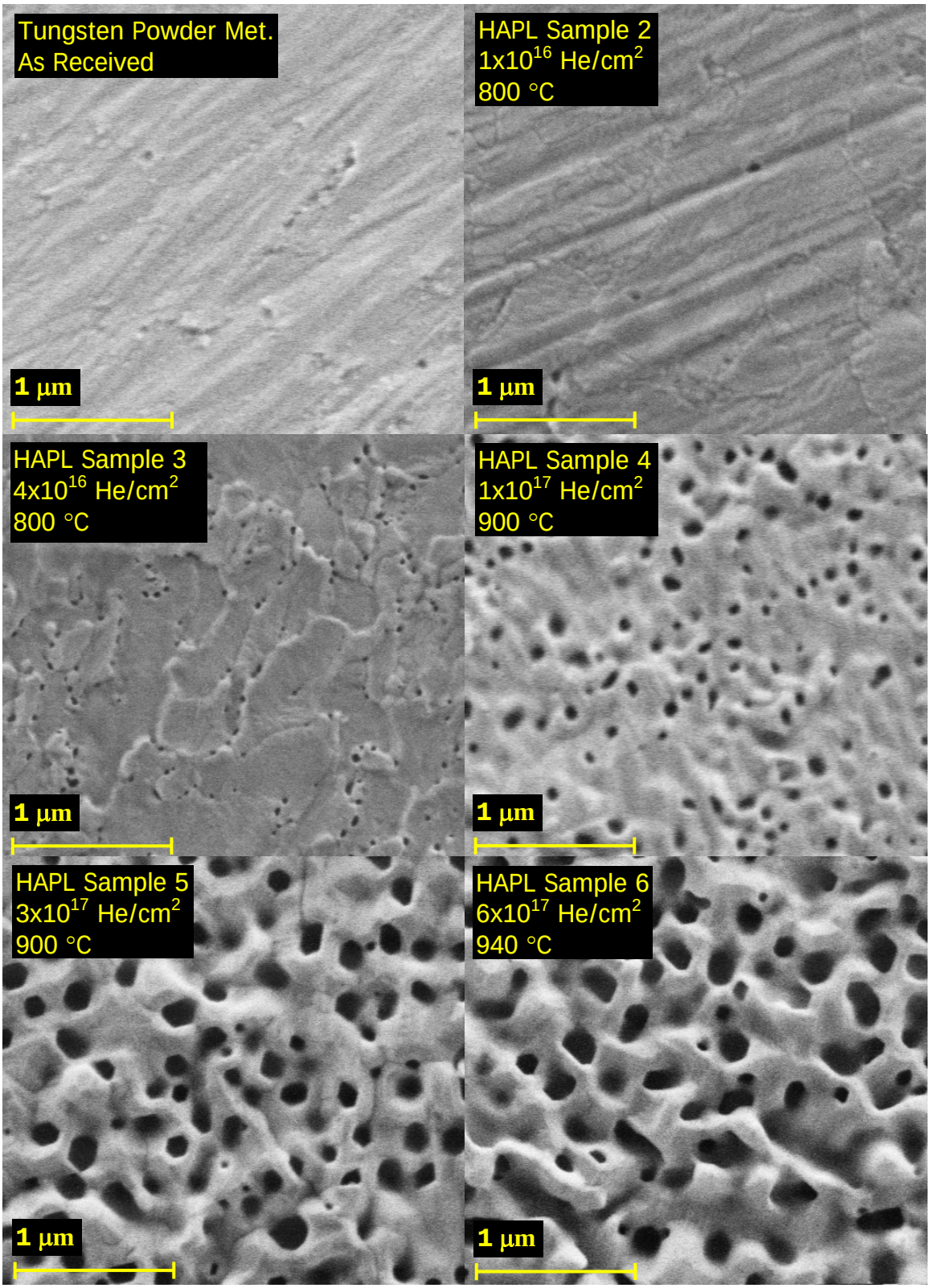

Figure 14-6: Fluence Scan, $^{4}He^{+}$ on Tungsten HAPL Samples

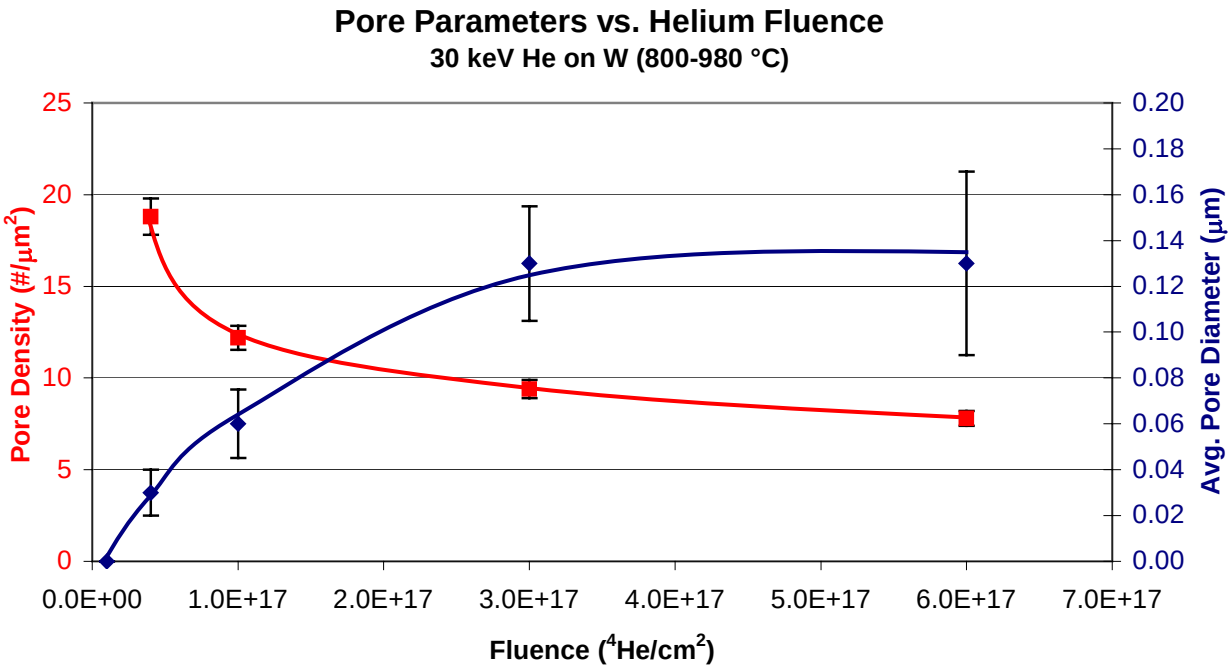

Figure 14-7: Increase of Pore Diameter and Decrease of Pore Density with Helium Fluence on Tungsten

The next results are for the temperature scan. The voltage was kept constant at 40 kV, and the fluence was kept constant at $3x10^{17}$ He/cm^2. Since variation of the current was the only way to control temperature, the flux and time were different for each experiment to still allow for a constant total fluence.

Figure 14-8 shows the results. Sample 7 shows implantation at 700 °C. The pores are the smallest in this picture. Sample 8 shows slightly larger pores at 770 °C. Sample 9 shows implantation at 950 °C, and Sample 10 has the largest pores at 1120 °C implantation.

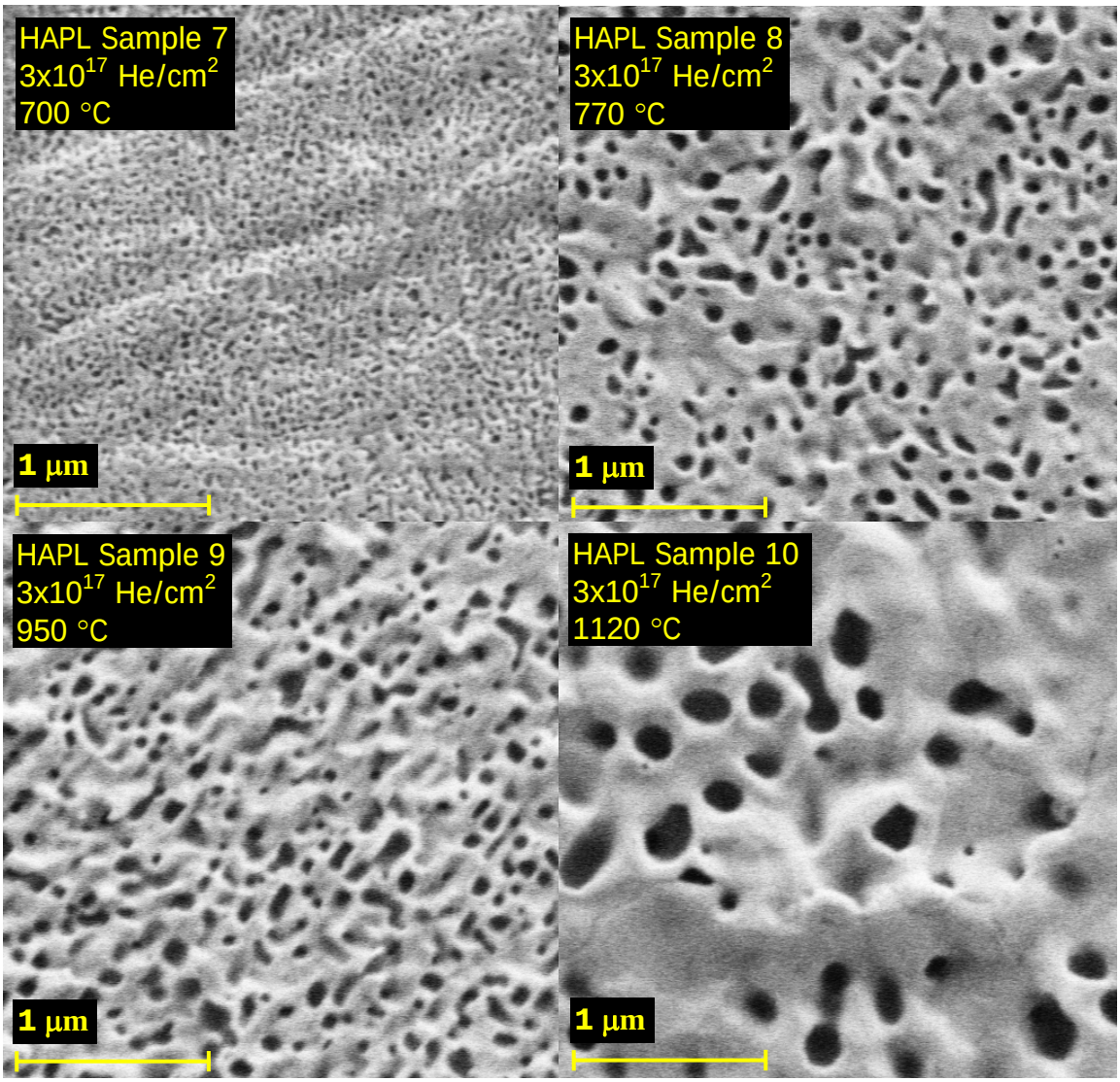

Figure 14-8: Temperature Scan, $^{4}He^{+}$ on Tungsten HAPL Samples

The pore diameter and density were plotted for this scan as well (see Figure 14-9). This figure does not show a specific type of trend, but over the temperature range from 700 to 1120 °C, the average pore diameter increased by a factor of 6, and the pore density decreased by a factor of 35. If the temperature difference only affects how the helium precipitates, and the total amount is still the same, it makes sense that the 2-D pore density would decrease by about the square of the increase in diameter.

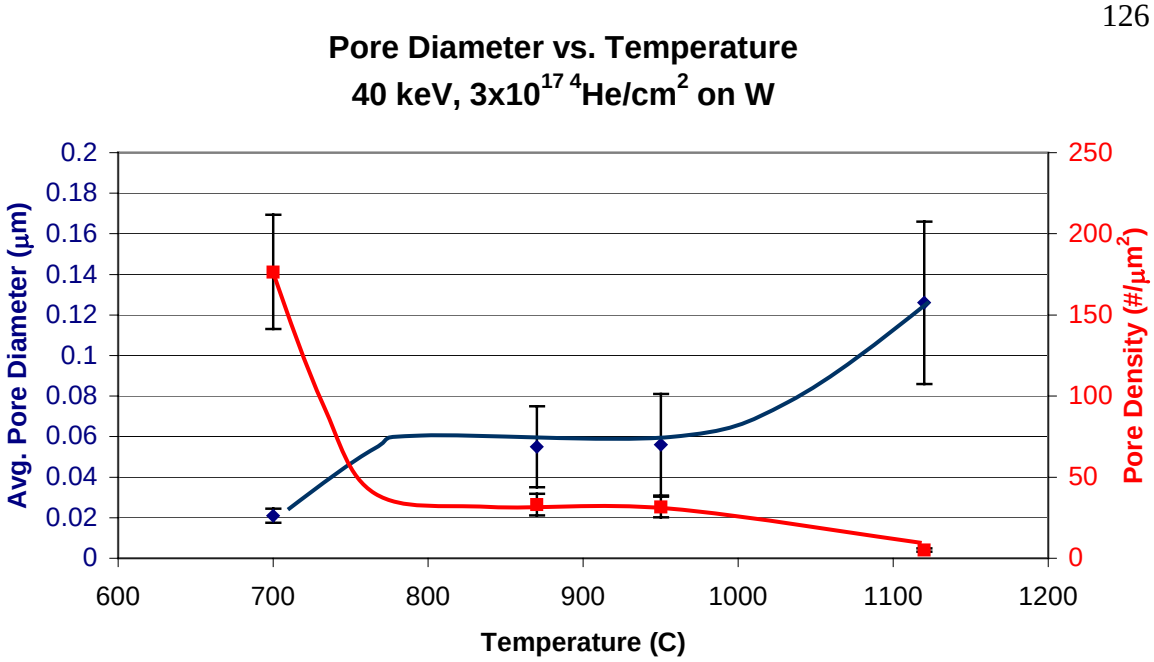

Figure 14-9: Increase of Pore Diameter and Decrease of Pore Density with Temperature in Tungsten under Helium Implantation

The effects of voltage did not show a clear trend. In the voltage scan, fluence was kept constant at $3x10^{17}$ He/cm^2, and temperature was kept constant (870-940 °C) by adjusting the current with the voltage. Figure 14-10 shows the results from six samples. It was difficult to control the higher voltages as there were problems with breakdown during the experiments. This led to a variation in the energies. Sample 15 that received 80-90 kV implantation shows larger pores, and Sample 9 at 40 keV shows slightly smaller pores, but all of the others are about the same. Unfortunately, both the 40 kV and 80-90 kV samples were square while the others were round. Sample 15 especially was very difficult to control, so it went through a different fluence and energy sequence. Only the samples at 20, 30, 50, and 60 kV were the same and controlled the best, and they show no clear trend.

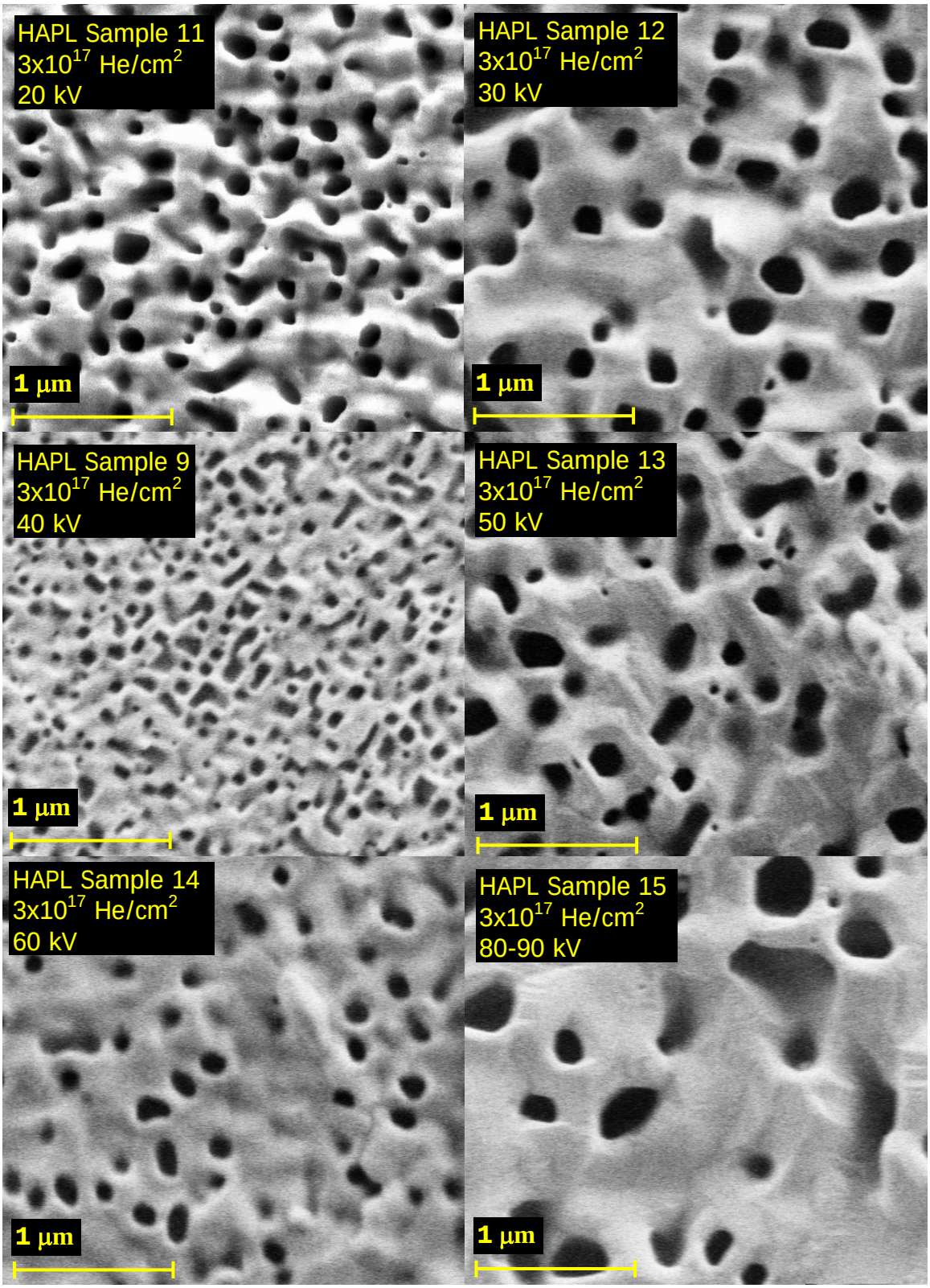

Figure 14-10: Voltage Scan, $^{4}He^{+}$ on Tungsten HAPL Samples

It should also be pointed out that the flux reaching these samples was not uniform. This was most likely due to the geometry of the chamber. It appears that the tops of the sample received less implantation than the bottoms since the top was slightly protected by the stalk. In most of the samples, the difference was not that noticeable, but it became more noticeable with a smaller total fluence. Figure 14-11 shows the variation. These three pictures are from the same sample at different locations. The smallest number of pores occurred at the top of the sample, and the highest occurred towards the bottom.

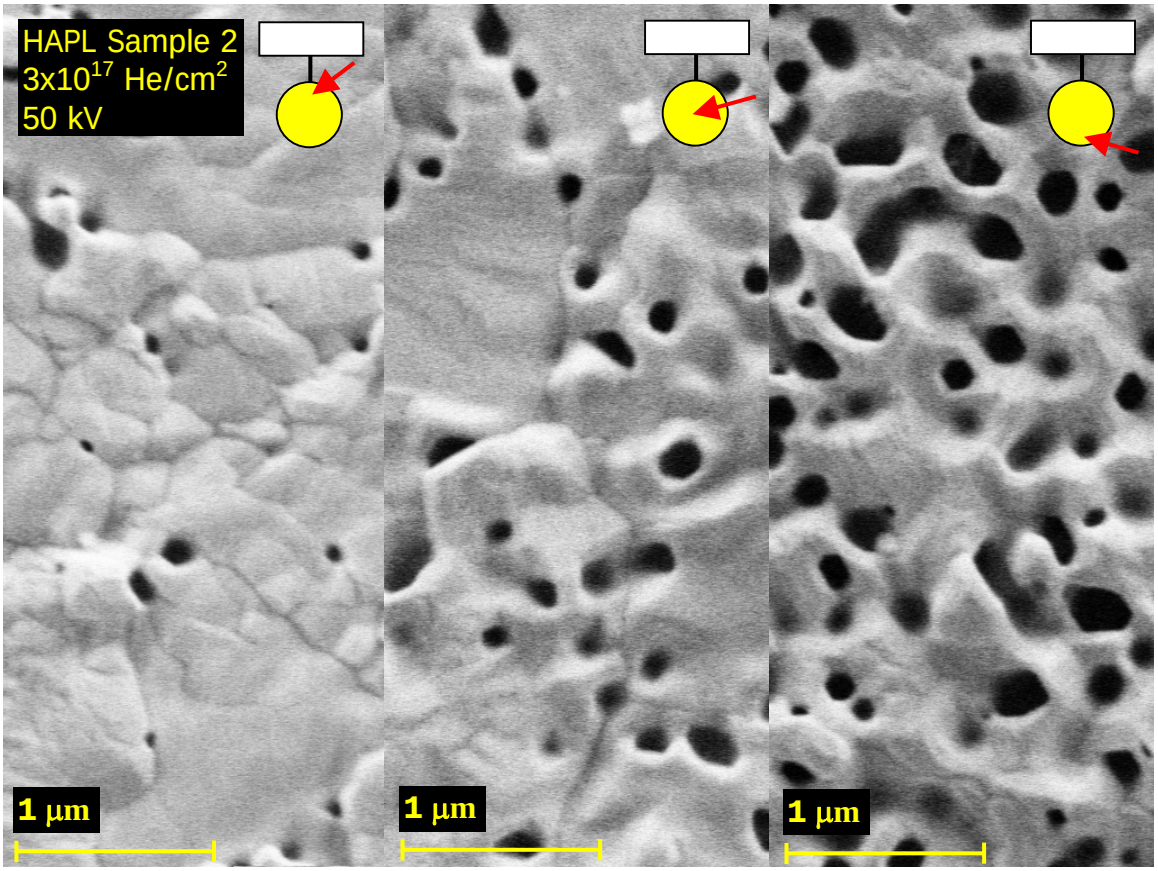

Figure 14-11: Flux Variation over the Sample Surface

14.2 Secondary Electron Emission

For all of the various cathodes that were installed in the chamber, the secondary electron emission was determined in order to know the true ion current reaching the cathode. Equation 13-1 was used to find the secondary electron emission coefficient.

14.2.1 Solid Cathodes

Temperature data was available for the molybdenum and titanium targets. Figure 14-12 shows the secondary electron emission as a function of voltage for both materials. Each curve represents a different run, and they were all D-D experiments. In general, the secondary electron emission is higher than expected, meaning the actual ion current is much lower than the meter current.

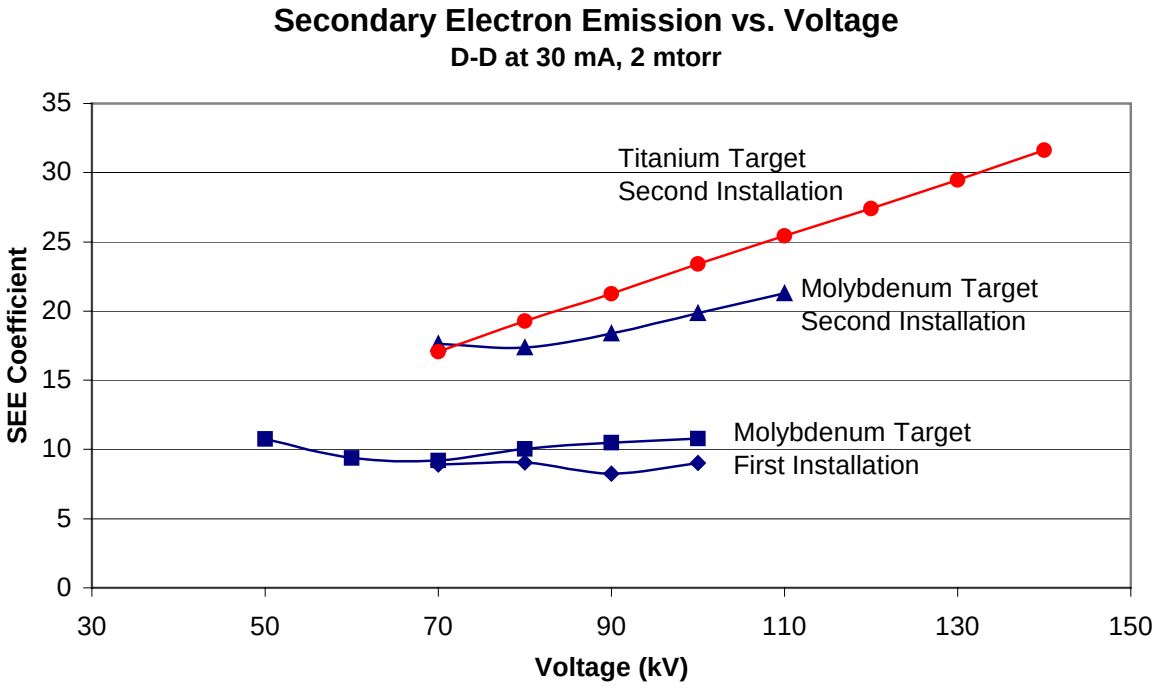

Figure 14-12: Solid Target Secondary Electron Emission Increase with Voltage

When the molybdenum target was first installed, the secondary electron emission coefficient varied around 10-12. The second installation resulted in about double the coefficient at the same conditions. When the target was removed the first time, it was taken out while still hot (~200 °C). The surface visibly changed colors when exposed to air, so it probably formed an oxide on the surface. The oxide may have been responsible for the increased secondary electron emission on the second installation. The titanium target also had high coefficients on the second installation. (Temperature readings were not taken for the first installation).

14.2.2 HAPL Samples

The experimentation with the HAPL samples was designed solely to determine the effect of the implantation on surface morphology. Many of the samples were not run long enough for the steady-state temperature to be reached. In others, the voltage or current varied. These characteristics of the runs did not lead to very clear trends in the secondary electron emission. In general, though, the coefficients varied between 10 and 20 over the runs when steady state was reached. The coefficients were calculated for each run to determine the accurate total fluence into the samples (which is what was reported in the previous scanning electron micrographs).

14.2.3 W-Re Grids

The effect of secondary electron emission is very important to normal operation of the IEC device with the W-Re grids installed. Temperature data was taken for many voltage scans. Figure 14-13 shows the calculated secondary electron emission

coefficients as a function of voltage for various voltage scans. Both D-D runs and D-^{3}He runs at around 2 mtorr pressure are shown.

The main feature to note is that there is quite a bit of scatter in the data, but the scatter is the same for D-D and D-^{3}He. This scatter is from variations in temperature readings at different locations on the grid. During runs it is visibly obvious that different areas of the grid are glowing brighter than others at times. This asymmetric heating must be due to non-uniform ion flow in certain angles. The location on the grid that the pyrometer measures from can result in varying secondary electron emission.

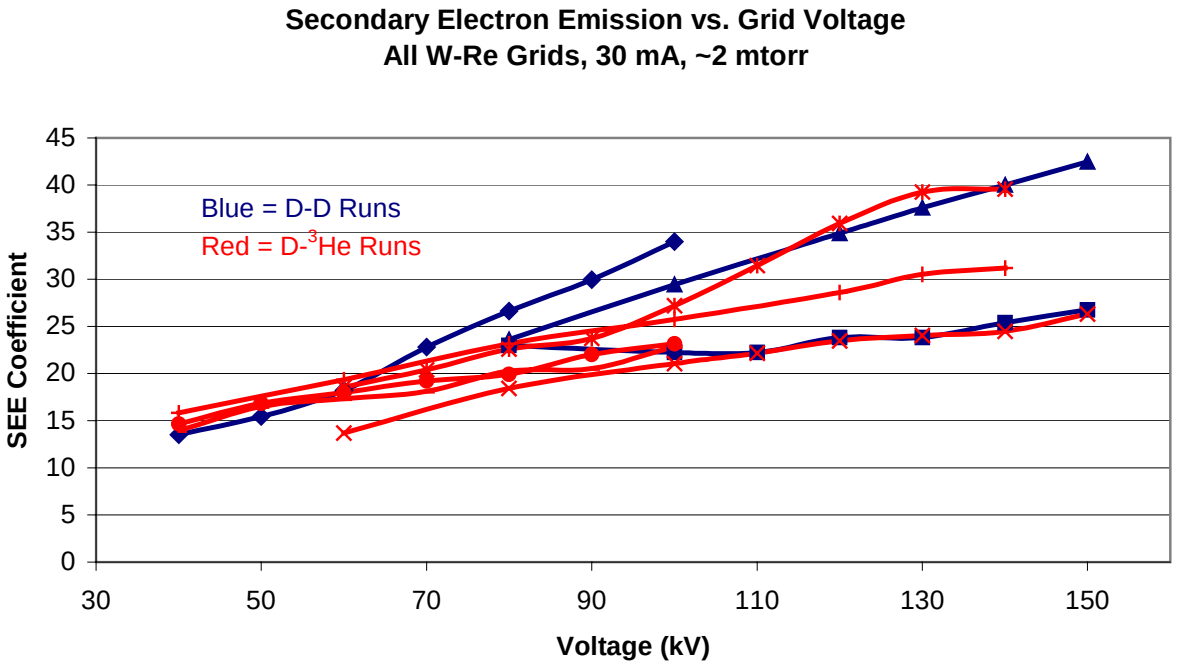

Figure 14-13: Calculated Secondary Electron Emission from W-Re Grids

To determine an average secondary electron emission coefficient for each voltage, the temperatures from all the scans were plotted and fitted with an appropriate trend-line. The average temperature at each voltage was then used to determine the coefficient. Figure 14-14 shows the average plot.

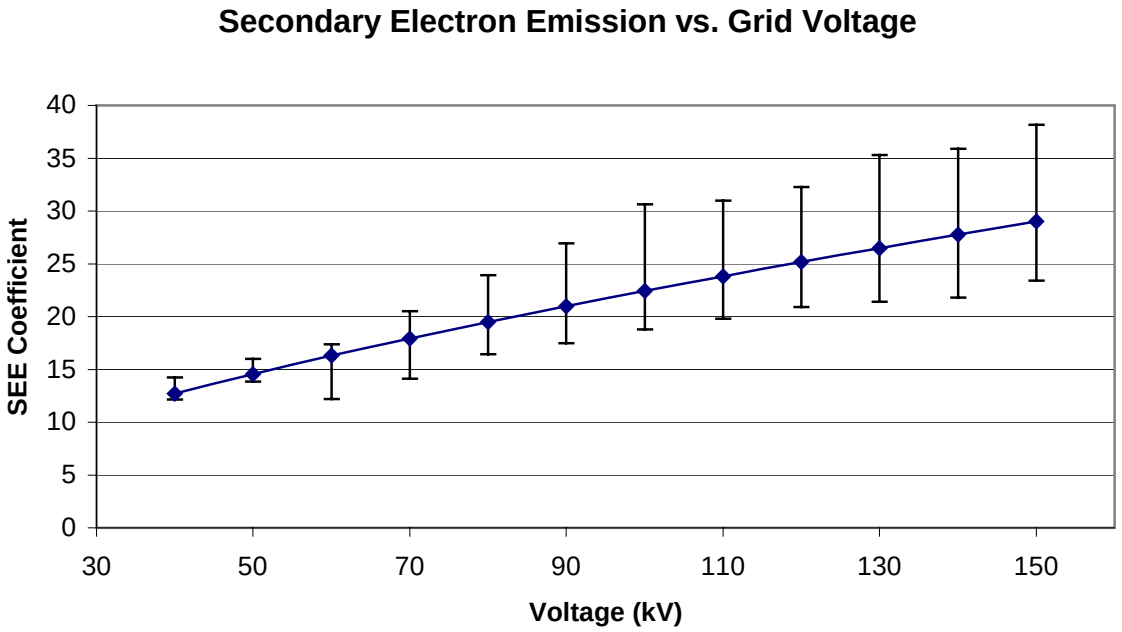

Figure 14-14: Average W-Re Grid Wire Secondary Electron Emission Increase with Voltage

The coefficient rises from about 13 at 40 kV to 29 at 150 kV. This means that at a meter current of 30 mA, the actual ion current into the cathode is 2 mA at 40 kV and 1 mA at 150 kV. It will be important to compare these values to numerical modeling work that is occurring both at Wisconsin and at other IEC projects in the future.

14.2.4 Water-Cooled Cathode

The water-cooled cathode used for ^{13}N production allowed for an alternative method of determining the secondary electron emission. The temperature drop was measured across the input and output of the water through the cathode using thermocouples. The water mass flow rate was measured at 0.016 kg/s. These data points over a run were used to plot the amount of heat removed from the system. Figure 14-15 shows this plot as a function of voltage at a constant current.

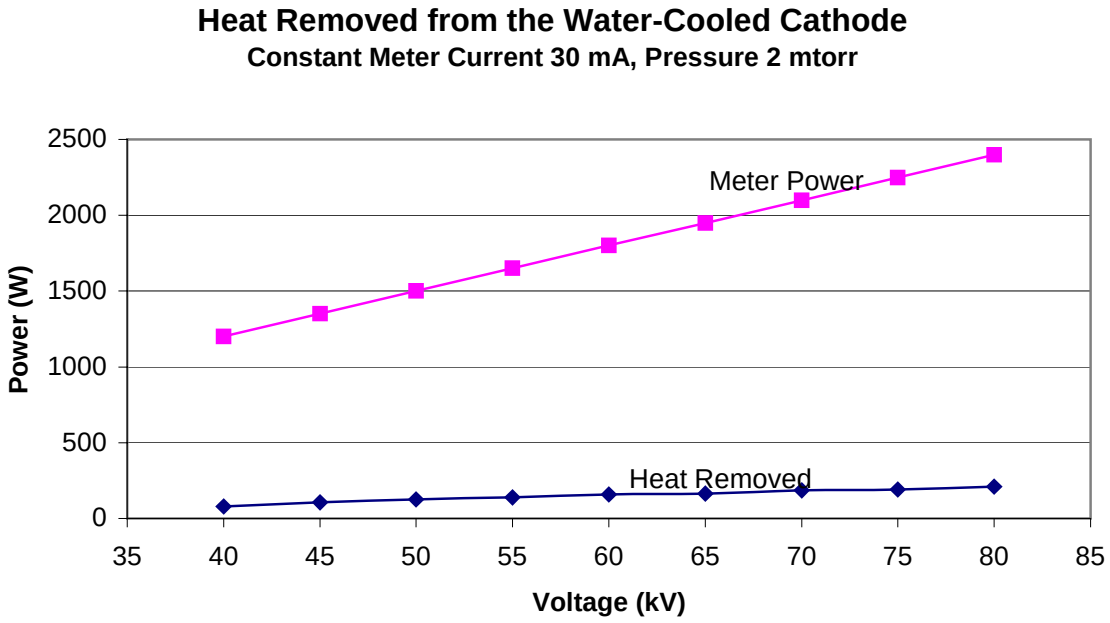

Figure 14-15: Heat Removed from Water-Cooled Stainless Steel Tube

There was a drastic difference in the meter power and the heat removed from the cathode. The meter power varied from a factor of 11 to 15 times greater than the heat removed, so the secondary electron emission coefficient varied from about 11 to 15. The heat should not have been removed in any other way like conduction or convection.

14.3 Computing the Embedded Number Density

14.3.1 Deuterium Density

With the measured values of reaction rate at a specific meter voltage and current, a small computer code using Mathematica™ was used to determine the embedded number density in the W-Re grid wires. The results of the source regime experiments were used to determine the total embedded reaction rate. The ion energy used was that of the meter voltage. The ion current was found using the meter current and the secondary

electron emission data. The only unknown then (from Equation 12-8) is the embedded number density. The program was designed to solve for an average, uniform density through the entire ion path into the metal.

Experiment 1063 was used as a representative D-D experiment that gave high D-D reaction rates. The neutron and proton raw counts were used to find the total neutron and proton production using the new calibration factors found from Part I. Then the embedded contribution of those rates was found again from the results of Part I. The computer program was used to solve for the embedded number density (see Appendix E). The average embedded density as a function of voltage is shown plotted in Figure 14-16.

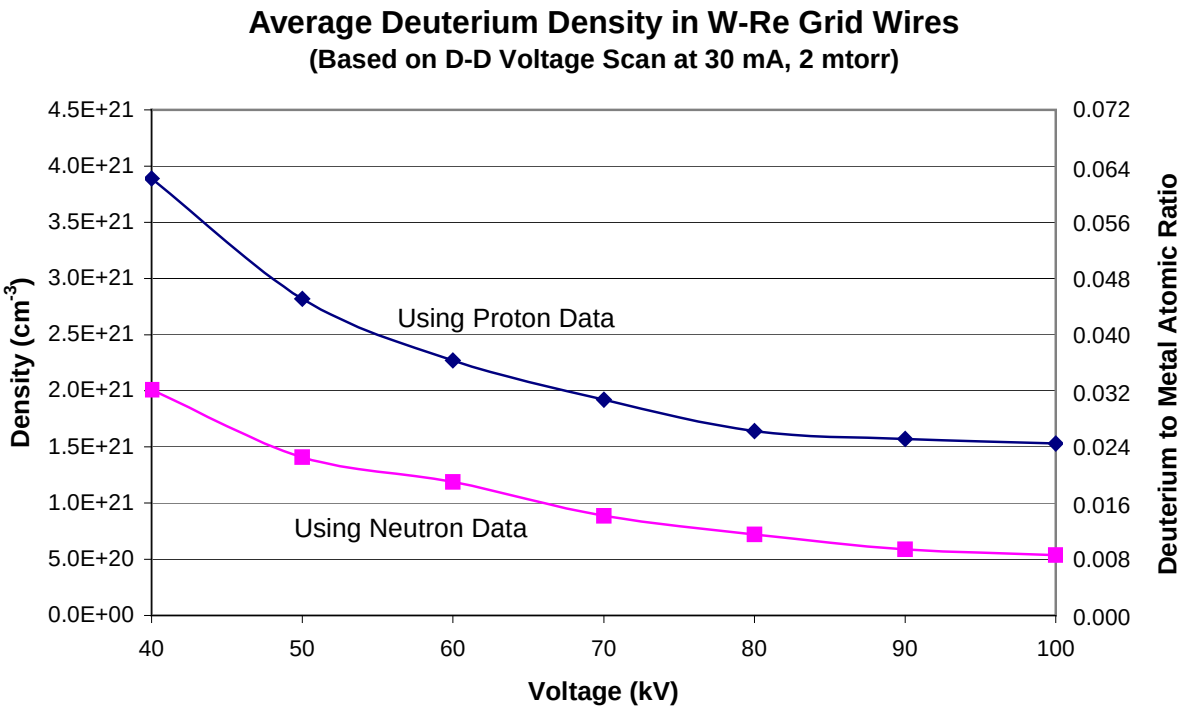

Figure 14-16: Deuterium Density in W-Re Grid Wires

The top curve in Figure 14-16 is the density solved using the neutron data, and the bottom line is that solved using the proton data. The difference shows the continued discrepancy between the numbers. If the difference were true, the total deuterium density would be the addition of the two curves. Each curve only shows half of the rate. It is interesting to note that the average density appears to drop with voltage. This result is probably due to a non-uniform density profile in the wires. At the higher voltages, the deuterium is able to penetrate deeper into the wire. A lower density at deeper depths then can decrease the embedded rates. The density varied from 0.008 to 0.064 deuterium to metal atomic ratio over the range of the graph.

The gas concentration solved using Equation 12-3 and the diffusion coefficient given by Equation 12-4 is on the order of 10^{14} deuterium ions/cm^3 for the grid conditions. This is much lower than the values from Figure 14-16. Most likely the deuterium diffusion coefficient is much different than the experimental values. Assuming a deuterium density of 10^{21} cm^{-3} at 1 μm in the wire and a linear fall-off in concentration to the surface, the diffusion coefficient must equal about 10^{-11} cm^2/s during steady state. These differences can also be due to trapping locations in the cathode.

14.3.2 Helium Density

The helium-3 embedded density could be determined from two different types of experiments. A D-^{3}He run could be used; however, the D-^{3}He proton production rate from embedded reactions is a combination of D on ^{3}He and ^{3}He on D reactions. The difficulty is that the fraction of deuterium ions to helium ions is not known when running both gases. It was better to use a D-D run that was done immediately after a number of

D-^{3}He runs when the grid built up its maximum helium density. Then with only deuterium ions making up the current, it was more accurate to determine the average helium density.

These experiments were further complicated by the fact that the D-^{3}He rate while only running deuterium drops off fairly quickly with run time. This means that helium is being measurably lost from the grid wires during runs. Experiment 835 was a D-^{3}He run that reached maximum rates over the 40-100 kV range. Approximately two hours later, run 836 was run with only deuterium at a constant 100 kV, 30 mA, 1.9 mtorr to measure the D-^{3}He proton production rate. The data from run 836 was used to determine the average embedded density of helium as a function of run time. Appendix E contains another sample computer code for determining the helium density. Figure 14-17 shows the result.

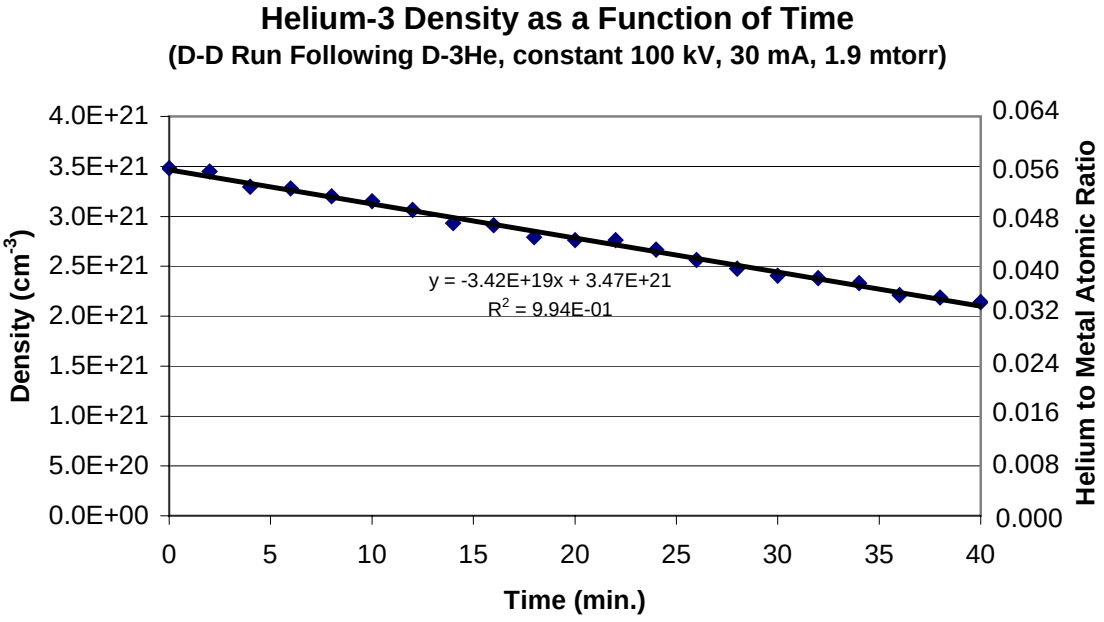

Figure 14-17: Helium-3 Density Drop-off with Run Time in W-Re Grid Wires

The left-most point on the graph shows the helium density at or near its maximum value in the IEC grids. Over this experiment, there was a linear, steady drop-off in the density with run time. The drop-off can either be due to helium diffusing out of the grid wires due to grid heating, or due to helium getting knocked out or pushed deeper into the wires due to deuterium ion bombardment. The helium to metal ratio at the zero time is about 0.056. The deuterium to metal ratio at 100 kV from Figure 14-16 is somewhere between 0.008 and 0.025. This comparison confirms previous evidence showing that helium builds up to higher densities than deuterium in tungsten at the elevated temperatures.

Chapter 15 Ion Implantation Discussion

15.1 Use of Tungsten in Fusion Systems

Tungsten has been an attractive potential first wall material for fusion systems due to its small sputtering yield but sputtering has not been studied in this work. The formation of blisters can complicate sputtering because it can result in exfoliation of the surface. The pore formation seen on tungsten due to helium implantation at high temperatures is probably a much better development than blistering. The pores do not seem to lead to exfoliation. Perhaps running the first wall of a fusion system at elevated temperatures (>700 °C) would be better for the wall life.

The helium implantation fluences from this work were very small compared to the fluences reached in an actual D-T fusion reactor. The highest helium fluence of $6x10^{17}$ He/cm^2 from this line of experimentation would be reached on the reference HAPL chamber wall after only about 8 hours of full-power operation [1]. This means that the pore formation will occur almost immediately in a fusion power plant scenario.

In the future, more work should be done to determine the rate of helium re-emission from the porous surface. Much higher helium fluences should be reached at the high temperatures, and the erosion rate should be measured. Finally, it would be better to look at the full range of helium ion energies that will be experienced in a fusion system.

15.2 Maximizing the Embedded Fusion Rate

The computer model that was used to solve for the embedded fusion rate can be used to determine how to maximize that rate. Although this would not be useful for a

fusion energy system since beam-target systems have limitations, it can be used to determine how high the rates for isotope production can be increased.

The maximum embedded helium-3 density that might be reached is about a 1:1 helium to metal ratio. The power supply used at Wisconsin can accelerate 200 keV deuterium ions into the grid at a maximum meter voltage of about 70 mA. The actual ion current, assuming a secondary electron emission coefficient of 20, would be about 3.3 mA. This operating regime would produce an embedded reaction rate of 5.3×10^9 D-^{3}He reactions/s.

It is probably safe to say then that D-^{3}He embedded fusion is limited in a reasonably small IEC device to producing about 10^{10} p/s. Even this rate will be difficult to achieve in the current setup. Any further increase would need a power supply capable of higher current. If it were possible to suppress the secondary electron emission, the current could also be increased. Beyond that, it remains important to achieve the converged-core operating regime to further increase the D-^{3}He rates.

15.3 References

[1] J.D. Sethian et al., "Fusion Energy with Lasers, Direct Drive Targets, and Dry Wall Chambers," *Nuclear Fusion*, **43**, 1693 (December, 2003).

Chapter 16 Conclusions & Recommendations

16.1 Source Regimes

The D-D reaction in the UW IEC device at 2 mtorr has been found to have the following source regime breakdown:

- 70% volume regime
- 22% converged core regime
- 8% embedded regime

These percentages are for the total reaction rate in the chamber, and they apply over the 40-100 kV range at 30 mA meter current. The large volume regime suggests that a larger chamber would have a higher reaction rate, but it is probably not desirable to move towards a larger device for near term applications where a portable device is desired. It will probably be better in the long run to move towards a low pressure, converged-core only regime that drives up the density in the core of the device.

The D-^{3}He reaction in the UW IEC device at 2 mtorr has been found to have the following source regime breakdown:

- Negligible volume regime
- 5% converged core regime
- 95% embedded regime

Again, these results are valid over the 40-100 kV range at 30 mA meter current. It may be possible to increase the embedded reaction rate, but beam-target fusion has its limitation. It would probably be better in the long run to move towards the low-pressure regime to try to increase the reaction rate.

In the future, it would be beneficial to do a complete source regime analysis at different background pressures. Since the results of this work suggest that there is not much difference with voltage over the 40-100 kV range, it would be good to repeat the source regime experiments in a pressure scan at constant voltage. The lower pressures should produce a larger percentage of converged core reactions. However, if a lower pressure regime does not improve the reaction rates, it may not be worth pursuing.

16.2 Isotope Production

Beam-target D-^{3}He fusion has successfully been used to produce medical isotopes in a proof-of-principle experiment.

- 1.5 nCi of ^{94m}Tc were produced with a solid molybdenum target
- 1.0 nCi of ^{13}N was produced with a water-cooled steel tube

The water-cooled system proved to be a good way to produce the isotopes and remove them from the system without venting the vacuum chamber. The operational difficulties could probably be eliminated with improved manufacturing techniques.

The extrapolation of the current beam-target isotope production system to produce the activities needed for medical diagnostics may lead to a system that is not commercially practical. At maximum parameters, the IEC beam-target setup has been calculated to produce approximately 0.0012 mCi ^{13}N/mA deuterium current. Amps of deuterium current then would be needed to produce a medical dose around the 10's of mCi level. The power requirements of such a system would be large (100's of kW). Also, the secondary electron emission occurring at the cathode increases the power

requirements by a factor of 20-30. It may be better to design such a system with an actual beam of fusion ions bombarding a flat plate target. The secondary electrons coming off the plate would not draw from the power supply going into the beam.

16.3 Ion Implantation

The large embedded fusion regime was found to be due to the buildup of fusion ions in the cathode. At the 100 kV, 30 mA, 2 mtorr condition the average ion densities in the tungsten-rhenium grid wires over the ion penetration depth were:

- 0.008 to 0.024 D:W (deutrium:metal) atomic ratio
- 0.056 He:W (helium-3:metal) atomic ratio

The helium builds up to higher densities than the deuterium at the high temperatures experienced by the grid wires.

Deuterium implantation up to $2x10^{18}$ D^+/cm^2 on tungsten samples at high temperatures (1100-1200 °C) did not cause any surface deformations to occur. On the other hand, helium implantation at the elevated temperatures created a porous surface structure where the bubbles interacted with the surface. The threshold for pore formation was found to be:

- Below $4x10^{16}$ He^+/cm^2 on tungsten at 800 °C

The pore size increased with increasing fluence and increasing temperature. The pore density decreased with increasing fluence and increasing temperature.

The porous structure is most likely the cause for the degraded grid performance after many D-^{3}He runs. The sharp edges associated with some of the pores may cause

significant local electric field gradients near the wires. It will be interesting to determine how the pore formation will affect the use of tungsten as a first wall material in fusion reactor designs. Future work should examine the sputtering and exfoliation rates of the tungsten under continued bombardment. Allowing the first wall to stay at the elevated temperatures needed for pore formation may help to increase the wall life. Since the high temperatures prevent the formation of blisters, which can then break and exfoliate, the pore formation may be a good feature. A set of helium implantation experiments comparing the high temperature erosion rate to low temperature erosion rate at the same fluence conditions would be extremely valuable.

The final implantation result worth noting is the high secondary electron emission seen on the various cathodes in the IEC device. The secondary electron emission coefficient on average varied linearly from:

- 13 at 40 kV to 29 at 150 kV

This huge electron emission means that a great deal of power is lost in the IEC device due to ion impact on the cathode. It also means that the re-circulation ion current through the grid will be lower than what was believed before the experimentation was done.

Appendix

Appendix A Proton Detector Calibration Factors

On-Axis Proton Detector

The volume source calibration factor for the on-axis proton detector has been calculated using MCNP (Monte Carlo) methods and is given by:

$$R_{vol} = R_{\det}\left[\frac{4\pi r^2}{A}\left(\frac{1}{\eta_a \eta_d}\right)\times 21\right]$$

This factor is used to convert the counting rate from the proton detector (R_{det}) to the total reaction rate in the chamber (R_{vol}). In this factor, r is the distance from the center of the chamber to the detector, A is the detector surface area, η_a is the anode transparency, and η_d is the detector efficiency. The factor 21 was found by Dr. Mohamed Sawan at the University of Wisconsin using MCNP methods and includes the extrapolation from the solid angle of the detector to the entire chamber volume. For the current setup, r=81.25 cm, A=12 cm^2, η_a=0.927, and η_d=0.95; leading to a calibration factor of **164,850**. This factor was the original calibration factor used based on the assumption that the chamber operated in an entirely volume source mode.

The converged core source looks like a point source to the detector, so it can be modeled similar to Equation A-1, but without the factor of 21 and with another transparency for the inner grid η_c (0.95):

$$R_{core} = R_{\det}\left[\frac{4\pi r^2}{A}\left(\frac{1}{\eta_c \eta_a \eta_d}\right)\right]$$

This calibration is equal to **8,260**. With only a point source present in the chamber, this factor would be used to convert the counting rate from the proton detector (R_{det}) to the total core reaction rate (R_{cor}).

The embedded source also acts like a point source with an additional shadowing factor of 2 because protons born on the far side of a grid wire get stopped by the 0.84 mm thick tungsten-rhenium wire. It is also missing the cathode grid transparency:

$$R_{emb} = R_{\det}\left[\frac{4\pi r^2}{A}\left(\frac{1}{\eta_a \eta_d}\right)\times 2\right]$$

The embedded calibration factor is equal to **15,700**. With only an embedded source present in the chamber, this factor would be used to convert the counting rate from the proton detector (R_{det}) to the total embedded reaction rate in the grid wires (R_{emb}).

Off-Axis Proton Detector

The off-axis proton detector calibration factor was calculated using a piece-wise method. Only the volume source contributes to the off-axis counts since neither the core or grid are seen by the detector. The assumption made in this calibration factor is that the volumetric reaction rate is uniform throughout the chamber. Figure A-1 shows the solid angle seen by the off-axis detector. This volume was divided into 5 sections as shown. The SolidWorks™ modeling program was used to determine the volume of each section.

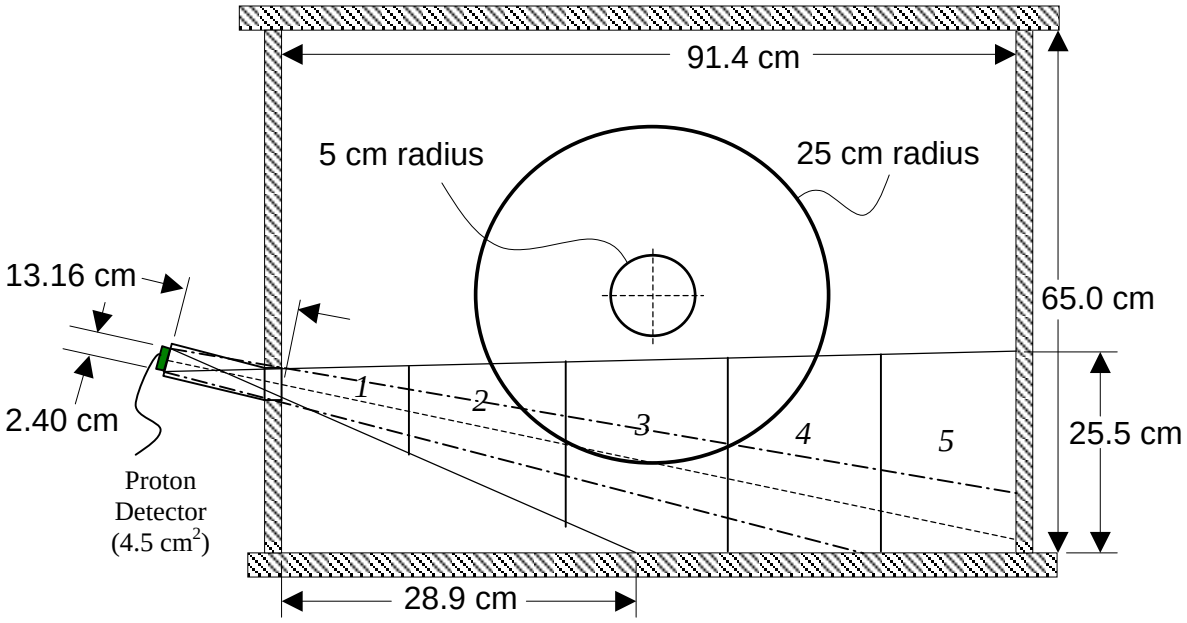

Figure A-1: Off-Axis Proton Detector Solid Angle

The volumes and radii to the centroid (from the detector face) of each section are:

Section 1	1237 cm^3 volume	17.65 cm radius
Section 2	4785 cm^3 volume	36.49 cm radius
Section 3	9846 cm^3 volume	55.32 cm radius
Section 4	13282 cm^3 volume	74.16 cm radius
Section 5	14397 cm^3 volume	93.00 cm radius

The counting rate (R_c in p/s) is related to the volumetric reaction rate (R_v in p/s/cm^3) by the expression:

$$R_c = R_v \sum_i V_i \frac{4.5}{4\pi r_i^2}$$

In this equation, r_i is the radius to each section, and V_i is the volume of each section. The detector surface area is 4.5 cm^2. Using this expression and the numbers above, R_c=5.32R_v. This expression can be used to solve for the volumetric reaction rate in the

chamber. Multiplying R_v by the total chamber volume (426477 cm^3) gives the total reaction rate caused by the volume regime.

There is one more factor that must be taken into account due to geometry. The volume enclosed by the two dash-dot lines in Figure A-1 is the only volume that "sees" the entire detector face. The rest of the solid angle only sees a part of the detector face. The solid angle cone was split up into five cones (see Figure A-2) to figure out this effect. The volume was found for each (using SolidWorks™), and an assumption was made as to how much of the detector face each cone saw:

Cone 1	2604 cm^3 volume	sees 100% detector face
Cone 2	6368 cm^3 volume	sees 80% detector face
Cone 3	9354 cm^3 volume	sees 60% detector face
Cone 4	11777 cm^3 volume	sees 40% detector face
Cone 5	13444 cm^3 volume	sees 20% detector face

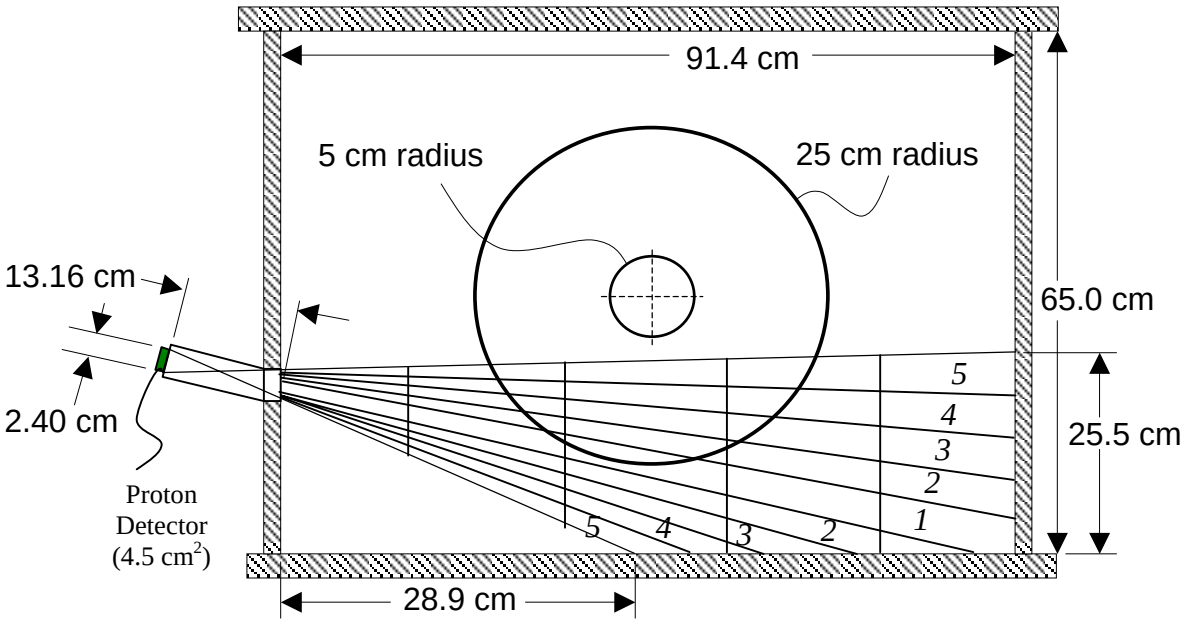

Figure A-2: Off-Axis Proton Detector Solid Angle Cone Segments

Averaging over all the section volumes, the reaction products in those volumes can access an average of only about 47% of the detector face. Finally, there is about a 90% transparency factor due to the presence of the outer grid, and the detector efficiency is 95%. The overall off-axis calibration factor then is equal to:

$$R_{vol} = R_{\det}\left[\frac{426477}{R_c / R_v} \times \frac{1}{0.47} \times \frac{1}{0.95} \times \frac{1}{0.90}\right]$$

This calibration factor is equal to **200,000**.

Appendix B Molybdenum Target Counting

Theoretical ^{94m}Tc Production Calculations

The ^{94m}Tc production in the molybdenum target was calculated using a shreadsheet such as given in Table B-1. The calculation assumes a constant proton production rate over a set time period and calculates the total activity produced. If the rate changes with time, the rate can be split up into segments. The results also need to be adjusted for decay if the run time is on the order of the half-life of the isotope produced.

The first column is the distance step into the molybdenum cathode. Each step was 0.001 cm. The cross-section was figured from empirical data for the initial proton energy. Equation 10-1 was then used to determine the ^{94m}Tc production/s in that distance step using the constant proton current. The stopping powers were used to calculate the energy loss in that distance step (given in the last column). Then, the new energy was placed in step 2, and all the calculations were repeated.

The process was repeated until the proton was left with about 6.6 MeV of energy where the cross-section drops off to negligible values. Then all of the production/s numbers were added up to find the total target production/s. This number was multiplied by the run time to determine the total number of ^{94m}Tc isotopes produced. Finally, the decay constant was used to determine the activity. Table B-1 shows a production of about 1 nCi of ^{94m}Tc produced after 20 minutes of run time at a proton current of 2.25×10^6 p/s.

Step	Energy (MeV)	Δx (cm)	Sigma (cm^2) (see Fig. 8-3)	Production/s	S_{low}	S_{high}	ΔE (MeV)
1	14.700	0.001	2.942E-25	2.130	543.89	2.84	0.181
2	14.519	0.002	3.150E-25	2.281	540.86	2.87	0.183
3	14.336	0.003	3.347E-25	2.423	537.78	2.90	0.185
4	14.151	0.004	3.533E-25	2.558	534.65	2.93	0.187
5	13.964	0.005	3.709E-25	2.685	531.46	2.96	0.189
6	13.776	0.006	3.872E-25	2.804	528.22	2.99	0.191
7	13.585	0.007	4.024E-25	2.913	524.92	3.02	0.193
8	13.392	0.008	4.164E-25	3.015	521.56	3.06	0.195
9	13.198	0.009	4.291E-25	3.107	518.13	3.09	0.197
10	13.001	0.010	4.405E-25	3.189	514.64	3.13	0.199
11	12.802	0.011	4.506E-25	3.262	511.08	3.17	0.202
12	12.600	0.012	4.592E-25	3.325	507.44	3.20	0.204
13	12.396	0.013	4.665E-25	3.377	503.73	3.24	0.207
14	12.189	0.014	4.722E-25	3.419	499.93	3.29	0.209
15	11.980	0.015	4.764E-25	3.449	496.05	3.33	0.212
16	11.768	0.016	4.789E-25	3.467	492.09	3.38	0.215
17	11.554	0.017	4.798E-25	3.474	488.02	3.42	0.218
18	11.336	0.018	4.789E-25	3.467	483.86	3.47	0.221
19	11.115	0.019	4.762E-25	3.447	479.59	3.53	0.224
20	10.891	0.020	4.716E-25	3.414	475.21	3.58	0.228
21	10.663	0.021	4.649E-25	3.366	470.72	3.64	0.231
22	10.431	0.022	4.562E-25	3.303	466.09	3.70	0.235
23	10.196	0.023	4.453E-25	3.224	461.33	3.76	0.239
24	9.957	0.024	4.321E-25	3.128	456.43	3.83	0.244
25	9.714	0.025	4.164E-25	3.015	451.37	3.90	0.248
26	9.465	0.026	3.981E-25	2.883	446.15	3.98	0.253
27	9.213	0.027	3.772E-25	2.731	440.75	4.06	0.258
28	8.955	0.028	3.533E-25	2.558	435.15	4.15	0.263
29	8.691	0.029	3.264E-25	2.363	429.34	4.24	0.269
30	8.422	0.030	2.961E-25	2.144	423.31	4.35	0.276
31	8.146	0.031	2.624E-25	1.900	417.02	4.45	0.282
32	7.864	0.032	2.249E-25	1.628	410.45	4.57	0.290
33	7.574	0.033	1.832E-25	1.327	403.57	4.70	0.298
34	7.276	0.034	1.372E-25	0.993	396.35	4.84	0.307
35	6.970	0.035	8.632E-26	0.625	388.75	5.00	0.316
36	6.654	0.036	3.015E-26	0.218	380.71	5.17	0.327

Total Isotopes Produced /s = 96.610
Total Prod. After 20 min = 115932
Total Activity (Ci) = 1.003E-09

Table B-1: ^{94m}Tc ($t_{1/2}$=52 min.) Production Calculations

In ^{94m}Tc production run 805, where the proton production varied with time, the proton production was split up into time intervals of constant proton production. The spreadsheet format shown in Table B-1 was used to calculate the ^{94m}Tc production from each segment. Then the time from each segment to the end of bombardment (EOB) was used to determine the number of isotopes left at EOB using the half-life. Table B-2 shows the theoretical ^{94m}Tc production from run 805 using this method. The last column is added up to determine the total activity from all the segments.

Time (min)	Raw Proton Count (60s)	Total Proton Rate (p/s)	Avg. Proton Rate Hitting Target (p/s)	^{94m}Tc Produced (in time interval)	^{94m}Tc Isotopes Left at EOB
0.00	0	0.00E+00	0.00E+00	0	0
1.50	185	4.84E+04	2.42E+04	372	263
2.50	854	2.23E+05	1.12E+05	574	411
4.25	7287	1.91E+06	9.53E+05	8571	6287
5.50	19642	5.14E+06	2.57E+06	16503	12308
7.25	25080	6.56E+06	3.28E+06	29500	22521
9.00	29229	7.65E+06	3.82E+06	34380	26866
10.50	23649	6.19E+06	3.09E+06	23843	19008
12.50	21851	5.72E+06	2.86E+06	29373	24050
14.50	29289	7.66E+06	3.83E+06	39372	33108
16.50	23938	6.26E+06	3.13E+06	32179	27790
18.50	24729	6.47E+06	3.24E+06	33242	29484
20.50	24412	6.39E+06	3.19E+06	32816	29893
22.50	21166	5.54E+06	2.77E+06	28453	26618
24.50	17028	4.46E+06	2.23E+06	22890	21993
26.50	12197	3.19E+06	1.60E+06	16396	16179
27.50	0	0.00E+00	0.00E+00	0	0
				Total ^{94m}Tc:	**296780**
				Total Activity (decays/s):	**65.89**
				Total Activity (nCi):	**1.78**

Table B-2: Run 805 ^{94m}Tc ($t_{1/2}$=52 min.) Production Calculations

Molybdenum Target Counting Efficiencies

A total of four efficiencies were determined to calculate the total activity present in the molybdenum target:

$$A = \frac{C}{\eta_e \eta_a \eta_g \eta_c}$$

C represents the number of 511 keV gamma rays counted by the detector in counts/s, and A is the total target activity in decays/s. The emission efficiency (η_e) takes into account how many gamma rays are released per decay, and the percentage of decays releasing a gamma ray. The attenuation efficiency (η_a) determines how the mass of the target will block or attenuate the gamma ray flux. The geometric efficiency (η_g) simply figures out what percentage of the total gamma rays from the distributed source reach the detector. Finally, the counting efficiency (η_c) determines the number of gamma rays detected in the detector for each one that hits the detector face.

A good way to visualize how the efficiencies multiply together is to place the spherical target inside a large spherical detector (see Figure B-1).

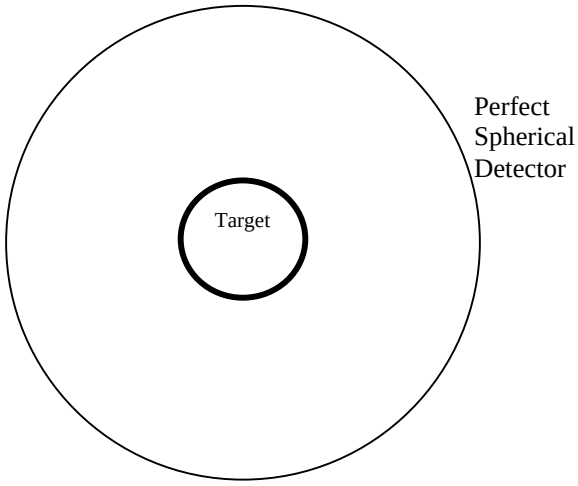

Figure B-1: Molybdenum Sphere Inside of a Perfect Spherical Detector

Emission Efficiency:

With the presence of a positron emitter, each decay event releases two 511 keV gamma rays per emission. The ^{94m}Tc isotope only decays by positron emission 82% of the time. Therefore the emission efficiency is 2*.82=**1.64.** This means that the counting rate seen by the spherical detector (in Figure B-1) from a point source positron emitter must be divided by 1.64 to get the actual activity.

Attenuation Efficiency:

The molybdenum target contains all of its ^{94m}Tc activity within 0.5 mm of the surface, so it can be thought of as a surface source on a sphere. The presence of the metal sphere, though, will absorb some of the gamma rays emitted. All of the activity in the target is localized at the outer surface. The attenuation efficiency determines at the fraction of gamma rays reaching the spherical detector compared to the total number of gamma rays produced.

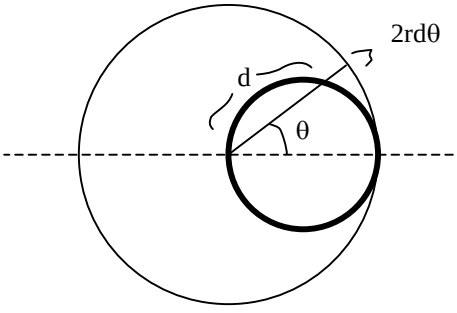

Figure B-2: Molybdenum Cathode Attenuation Efficiency Reference

In Figure B-2, the fraction of gamma rays coming from a point source on the left of the sphere (dark circle) that escape the system is determined. The distance the gamma ray travels through the molybdenum is given by d:

$$d^2 = r^2 + r^2 - 2rr\cos(\pi - 2\theta)$$
$$d = r\sqrt{2}\sqrt{1+\cos 2\theta}$$

The attenuation of 511 keV gamma rays through molybdenum in that distance is $e^{-.875d}$. This equation gives the fraction of 511 keV gamma rays remaining after passing through that distance. The attenuation factor is weighted by the area of the ring around the outer sphere that sees the distance d. The area of the ring is given by:

$$A_{ring} = 2\pi(2r)\sin\theta \times (2r)d\theta$$

For the right half of the large sphere, the average attenuation by the target is given by:

$$Attenuation = \frac{\int_0^{2\pi} d\phi \int_0^{\pi/2} 2\pi(2r)\sin\theta(2r)d\theta e^{-.875d}}{\int_0^{2\pi} d\phi \int_0^{\pi/2} 2\pi(2r)\sin\theta(2r)d\theta} = 0.339$$

For gamma rays traveling out towards the left half of the circle, the attenuation is 1.00 since there is no target material in the way. Averaging over the whole sphere, the total attenuation efficiency is **0.67** or 67%. This means that 33% of all the gamma rays emitted on the spherical surface are absorbed by the sphere, and the rest escape. Referring back to Figure B-1, only 67% of all the gamma rays produced will reach the perfect spherical detector due to the attenuation of the molybdenum.

Geometric Efficiency:

The geometric efficiency takes into account that the actual detector is a flat plate, 3.81 cm in diameter, that the target sits upon. The geometry efficiency is found by assuming an isotropic surface source around the sphere, but the material of the sphere is

ignored since the attenuation effect has already been accounted for. Figure B-3 shows target and detector geometry:

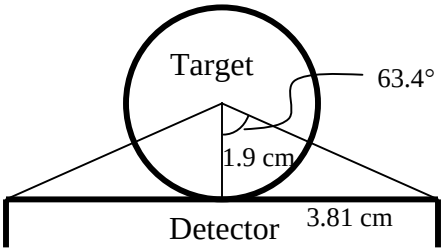

Figure B-3: 3.81 cm Diameter Molybdenum Target on 7.62 cm Diameter NaI Detector

Each point on the sphere has a different fraction of gamma rays that hit the detector face divided by the total 4π solid angle. All of these fractions were added up in an integral over the entire surface of the sphere. Figure B-4 shows the variables used in the integration:

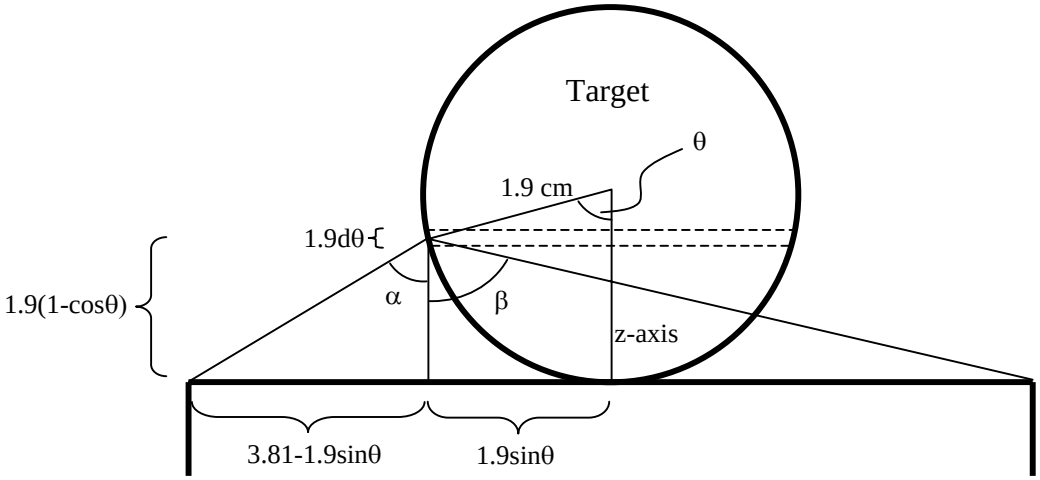

Figure B-4: Geometric Efficiency Integration Variables

Because there is azimuthal symmetry, the solid angle ratio at each point within the strip (shown as the dotted lines) is the same. It should be a fairly good approximation to

say that the detector captures all the gamma rays in the solid angle made by α+β. From this diagram it is seen that:

$$\alpha = \tan^{-1}\frac{3.81-1.9\sin\theta}{1.9(1-\cos\theta)} \qquad \beta = \tan^{-1}\frac{3.81+1.9\sin\theta}{1.9(1-\cos\theta)}$$

Then the solid angle fraction made by α+β is equal to:

$$\frac{\int_0^{2\pi} d\phi \int_0^{\frac{\alpha+\beta}{2}} \sin\varpi d\varpi}{4\pi} = \frac{1}{2}\left(1-\cos\frac{\alpha+\beta}{2}\right)$$

The variable ϕ is the rotation around the z-axis, so the integration is done from 0 to 2π. The variable ω is just an integration variable that integrates over the cone formed by the angles α+β. For each angle of θ, this equation is the fraction of the solid angle covered by the detector face. However, each angle has a different area of the total surface of the sphere covered, so that area will be used to weight the fraction. The area of each strip is equal to:

$$2\pi(1.9\sin\theta)(1.9d\theta)$$

Then the overall collection efficiency is:

$$\frac{\int_0^{\pi}\frac{1}{2}\left(1-\cos\frac{\alpha+\beta}{2}\right)2\pi(1.9\sin\theta)(1.9d\theta)}{4\pi 1.9^2} = \underline{\mathbf{0.27}}$$

The integral is divided by $4\pi 1.9^2$ to normalize the weighting to the total surface area. This means that 27% of the gamma rays emitted from the spherical surface source will reach the detector face. Referring again to Figure B-1, the actual NaI detector intercepts 27% of the gamma rays that hit the perfect spherical detector (ignoring attenuation).

Counting Efficiency:

The counting efficiency was calculated to be **0.17** for 511 keV gamma rays using a known source on the NaI detector. This means that 17% of the gamma rays that hit the detector face are actually counted.

Total Efficiency:

The total counting efficiency taking all four factors into account is equal to:

$$1.64 \times 0.67 \times 0.27 \times 0.17 = \mathbf{0.05}$$

The 511 keV gamma ray counting rate from the detector is divided by this number to get the total ^{94m}Tc activity in decays/s.

Appendix C Water Target Counting

Theoretical ^{13}N Production Calculations

For the theoretical ^{13}N production calculation, the production run was split up into 2-minute segments of constant D-^{3}He proton production. For each segment, the number of ^{13}N isotopes produced was calculated using the method shown in Appendix B but with the parameters for water. Then this activity was decayed to the end of the experiment to get the actual activity left from each segment at end of bombardment. Table C-1 shows the calculations. All the activities of the last column were added up to find that 1.68 nCi of ^{13}N should have been produced in run 863.

Time (min)	Raw D-^{3}He Proton Count	Total Proton Rate (p/s)	Protons (p/s) Hitting Water	N-13 Isotopes Produced	N-13 Isotopes Left at EOB
0	77	20148	10074	53	16
2	193	50502	25251	264	93
4	509	133188	66594	697	283
5	975	255125	127563	667	290
7	1727	451898	225949	2364	1182
8	3187	833932	416966	2181	1169
9	5056	1322987	661493	3460	1987
11	7587	1985265	992633	10385	6852
12	11128	2911827	1455913	7616	5385
14	15607	4083832	2041916	21363	17352
16	15036	3934420	1967210	20582	19203
				Total:	**53814**
				Activity:	**1.68E-09**

Table C-1: ^{13}N Production Calculation Example

Water-Resin Column Counting Efficiencies

The total resin column counting efficiency was calculated similar to the molybdenum target case. Four different efficiencies were determined and multiplied together.

Geometric Efficiency:

The resin column measures 5 cm long and 4.4 cm in diameter. Because the cylinder on a circular flat plate detector was a complex geometry, and because the ^{13}N concentration distribution was not known exactly, it was approximated as a point source in line with the center of the detector, 2.2 cm above the surface (See Figure C-1):

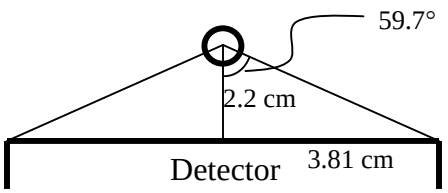

Figure C-1: Water Resin Column Geometry Approximation

The fraction of gamma rays reaching the detector (neglecting attenuation) is given as:

$$S.A. = \frac{\int_0^{2\pi} d\phi \int_0^{59.7} \sin\theta d\theta}{4\pi} = \underline{\mathbf{0.25}}$$

Counting Efficiency:

The counting efficiency was calculated to be **<u>0.17</u>** for 511 keV gamma rays using a known source on the detector.

Attenuation Efficiency:

Assuming the resin material is similar to carbon in mass, the gamma rays are slightly attenuated upon reaching the detector. The mass attenuation of 0.5 MeV gamma rays through carbon is equal to 0.087 cm^2/g. The density of the resin is slightly more than water, so probably around 1.5 g/cm^3. Then the fraction of gamma rays left after passing through 2.2 cm of the resin is:

$$e^{-0.087\times1.5\times2.2} = \underline{\mathbf{0.75}}$$

Emission Efficiency:

The ^{13}N isotope decays by positron emission 99.8 % of the time, and two gammas are given off for each positron emission, so the emission efficiency = **2**

Total Efficiency:

The total counting efficiency taking all four factors into account is equal to:

$$0.25\times0.17\times0.75\times2 = \underline{\mathbf{0.064}}$$

Appendix D Helium Implantation Pore Analysis

The analysis of the pore size and pore density caused by helium implantation was completed with the help of MatLab™. The following program was used to take a scanning electron micrograph and distinguish the pores from the rest of the surface:

```
clear, close all
I=imread('xxx.tif');
```

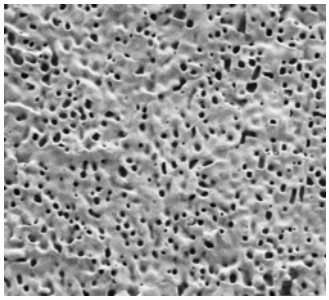

(imports an image file)

```
level=graythresh(I);
bw=im2bw(I, level);
```

(creates a black and white image with the pores in black)

```
se=strel('disk', 6);
bwc=imclose(bw, se);
bwco=imopen(bwc, se);
bwcoin=~bwco;
```

(closes up any partial holes)
(eliminates any speckles)
(inverts the image)

```
[labeled,numObjects]=bwlabel(bwcoin, 4);
numObjects
```

(counts the number of pores)

```
 numObjects =
          488
```

```
graindata=regionprops(labeled, 'basic')
allgrains=[graindata.Area]
```

(determines the area of each pore)

```
hist(allgrains, 100)
```

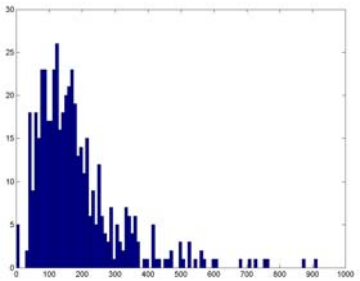

(plots out a histogram of pore areas)

Appendix E Embedded Fusion Numerical Model

Sample Mathematica™ Code for the D-D Reaction

```
(*EMBEDDED FUSION RATE CALCULATION*)
(*cross section functions - from Bosch & Hale, Nuclear Fusion, vol. 32, no. 4, (1992)*)
m = {{34.3827, 68.7508, 31.3970, 31.3970}, {69270, 5750100, 55576, 53701}, {7.454*^8, 2522.6,
      210.54, 330.27}, {2.05*^6, 45.566, -.03238, -.12706}, {52002, 0, 1.4987*^-6, 2.9327*^-5},
      {0, 0, 1.8181*^-10, -2.5151*^-9}, {63.8, -3.1995*^-3, 0, 0}, {-.995, -8.553*^-6, 0, 0},
      {6.981*^-5, 5.9014*^-8, 0, 0}, {1.728*^-4, 0, 0, 0}};

(*Input reaction : T(d, n)4He = 1,
                   3He(d, p)4He = 2,
                   D(d, p)T = 3,
                   D(d, n)3He = 4 *)
rea = 4;

(* sigma calculates the cross section in mb *)
sigma[en_, rea_] = (m[[2, rea]] + en*(m[[3, rea]] + en*(m[[4, rea]] + en*(m[[5, rea]] + en*m[[6,
      rea]])))/(1 + en*(m[[7, rea]] + en*(m[[8, rea]] + en*(m[[9, rea]] + en*m[[10, rea]])))/(en*
      E^(m[[1, rea]]/en^(0.5)));

(* Input initial ion energy in keV, ion density in cm^-3, and current *)
en0 = 100;
ionden = 1.0*^21;
current = 0.00128/1.6*^-19;  (*Assume current is constant throughout travel *)

data = Import["I:/embedding/W_p_stopping.dat"];
stopping = Drop[data, 5, -2];
stoppingfun = Interpolation[stopping];

(* ena = actual energy of ion in beam
   en = half of actual energy to use in cross section calculation
   envar = extra variable to help with for loop  *)

ena = en0;
rate = 0;
For[i = 1, i < 1000,
   If[ena >= 0,
     en = 1/2*ena;
     increate = 1*^-7*current*ionden*(sigma[en, rea]*1*^-27);
     rate = rate + increate;
     envar = ena;
     ena = envar - 1*^-7*1000*stoppingfun[envar/2000]*19.29;
     , Break[];
     ];
   i++];
rate
```

rate = 2.94674×10^{6}

Sample Mathematica™ Code for the D-^{3}He Reaction

```
(*EMBEDDED FUSION RATE CALCULATION*)
(*cross section functions - from Bosch & Hale, Nuclear Fusion, vol. 32, no. 4, (1992)*)
m = {{34.3827, 68.7508, 31.3970, 31.3970}, {69270, 5750100, 55576, 53701}, {7.454*^8, 2522.6,
      210.54, 330.27}, {2.05*^6, 45.566, -.03238, -.12706}, {52002, 0, 1.4987*^-6, 2.9327*^-5},
      {0, 0, 1.8181*^-10, -2.5151*^-9}, {63.8, -3.1995*^-3, 0, 0}, {-.995, -8.553*^-6, 0, 0},
      {6.981*^-5, 5.9014*^-8, 0, 0}, {1.728*^-4, 0, 0, 0}};

(*Input reaction : T(d, n)4He = 1,
                   3He(d, p)4He = 2,
                   D(d, p)T = 3,
                   D(d, n)3He = 4 *)
rea = 2;

(* sigma calculates the cross section in mb *)
sigma[en_, rea_] = (m[[2, rea]] + en*(m[[3, rea]] + en*(m[[4, rea]] + en*(m[[5, rea]] + en*m[[6,
      rea]])))/(1 + en*(m[[7, rea]] + en*(m[[8, rea]] + en*(m[[9, rea]] + en*m[[10, rea]])))/(en*
      E^(m[[1, rea]]/en^(0.5)));

(* Input initial ion energy in keV, ion density in cm^-3, and current *)
en0 = 100;
ionden = 1.0*^21;
current = 0.00128/1.6*^-19;  (*Assume current is constant throughout travel *)

data = Import["I:/embedding/W_p_stopping.dat"];
stopping = Drop[data, 5, -2];
stoppingfun = Interpolation[stopping];

(* ena = actual energy of ion in beam
   en = half of actual energy to use in cross section calculation
   envar = extra variable to help with for loop  *)

ena = en0;
rate = 0;
For[i = 1, i < 1000,
  If[ena >= 0,
    en = 3/5*ena;
    increate = 1*^-7*current*ionden*(sigma[en, rea]*1*^-27);
    rate = rate + increate;
    envar = ena;
    ena = envar - 1*^-7*1000*stoppingfun[envar/2000]*19.29;
    , Break[];
    ];
  i++];
rate
```

rate = 1.64317x10^6